



NUMERICAL MODELING OF MAGMA OCEAN SOLIDIFICATION AND CONCURRENT ATMOSPHERE FORMATION

vorgelegt von

M. Sc.

Athanasia Nikolaou

ORCID: 0000-0001-5526-1628

von der Fakultät II - Mathematik und Naturwissenschaften
der Technischen Universität Berlin
zur Erlangung des akademischen Grades

Doktor der Naturwissenschaften
-Dr.-rer.-nat.-

genehmigte Dissertation

Promotionsausschuss:

Vorsitzender: Prof. Dr. Mario Dähne

Gutachter : Prof. Dr. Dieter Breitschwerdt

Gutachterin : Prof. Dr. Doris Breuer

Gutachter : Dr. Nicola Tosi

Tag der wissenschaftlichen Aussprache: 25.11.2019

Berlin 2020

Science is a way of *thinking*
much more than it is a body of knowledge.

— Carl Sagan

ABSTRACT

Magma ocean is a crucial stage in the build-up of terrestrial planets. Its solidification and the accompanying outgassing of volatiles set the conditions for important processes that occur later or even simultaneously, such as solid state mantle convection and atmospheric escape.

In order to constrain the duration of a global scale magma ocean on Earth I have built and applied a 1D interior model coupled alternatively with either a grey $\text{H}_2\text{O}/\text{CO}_2$ atmosphere or with a pure H_2O atmosphere treated with a line-by-line radiative transfer approach.

This study examines the effects of several factors affecting the magma ocean lifetime, such as the initial abundance of H_2O and CO_2 , the convection regime, the viscosity, the mantle's melting temperature, and the longwave radiation absorption from the atmosphere. In this specifically multi-variable system I assess the impact of each factor with respect to a reference setting commonly assumed in the literature. This setting is intended to be a benchmark and it is deliberately kept low in complexity. Such approach helps emphasize the potential role of each additional modeled process in the solidification time.

It is found that the magma ocean stage can last from a few thousand to several million years for a rocky planet of terrestrial size and composition. By coupling the interior model with the line-by-line radiative transfer treatment in the atmosphere, I identify the conditions that determine whether the planet experiences a transient magma ocean or it ceases to cool and maintains a magma ocean, conditional on the assumption that atmospheric mass is conserved. I find a dependence of this distinction simultaneously on the mass of outgassed H_2O atmosphere and on the magma ocean surface melting temperature. The present work discusses their combined impact on the magma ocean lifetime in addition to the known dependence on albedo, orbital distance and stellar luminosity and notes observational degeneracies that arise thereby for target exoplanets. A potential magma ocean case for Venus and Mars is shortly discussed and is put in perspective with the study findings.

ZUSAMMENFASSUNG

Der Magma-Ozean ist eine entscheidende Phase beim Aufbau von terrestrischen Planeten. Seine Verfestigung und die damit einhergehende Ausgasung flüchtiger Stoffe schaffen die Voraussetzungen für wichtige Prozesse, die später oder sogar gleichzeitig ablaufen, wie die Konvektion des Festkörpermantels und das Entweichen der Atmosphäre. Um die Dauer eines Magma-Ozeans im globalen Maßstab auf der Erde einzuschränken, habe ich ein 1D-Modell des Inneren erstellt und angewendet, das wahlweise mit einer grauen $\text{H}_2\text{O}/\text{CO}_2$ -Atmosphäre oder mit einer reinen H_2O -Atmosphäre gekoppelt ist, die mit einem Spektralrechnungs-Ansatz behandelt wurde.

Diese Studie untersucht die Auswirkungen verschiedener Faktoren, die die Lebensdauer des Magma-Ozeans beeinflussen, wie etwa die anfängliche Häufigkeit von H_2O und CO_2 , das Konvektionsregime, die Viskosität, die Schmelztemperatur des Mantels und die Absorption langwelliger Strahlung aus der Atmosphäre. In diesem spezifischen multivariablen System bewerte ich die Auswirkung jedes Faktors im Hinblick auf eine in der Literatur allgemein angenommene Referenzkonfiguration. Diese Konfiguration soll als Richtwert dienen und ist bewusst wenig komplex gehalten. Ein solcher Ansatz hilft dabei, die potenzielle Rolle jedes zusätzlich modellierten Prozesses in der Erstarrungszeit hervorzuheben.

Es wurde festgestellt, dass die Magma-Ozean-Phase für einen felsigen Planeten von irdischer Größe und Zusammensetzung einige tausend bis mehrere Millionen Jahre dauern kann. Indem ich das Modell des Inneren mit dem Spektralrechnungs-Verfahren in der Atmosphäre verbinde, identifiziere ich die Bedingungen, die bestimmen, ob der Planet einem vorübergehenden Magma-Ozean ausgesetzt ist oder aufgehört hat abzukühlen und einen Magma-Ozean beibehält – unter der Annahme, dass atmosphärische Masse erhalten bleibt. Ich stelle eine Abhängigkeit dieser Unterscheidung gleichzeitig von der Masse der ausgegasteten H_2O -Atmosphäre und von der Schmelztemperatur der Magma-Ozean-Oberfläche fest. Die vorliegende Arbeit diskutiert den gemeinsamen Einfluss von beidem auf die Lebensdauer des Magma-Ozeans zusätzlich zu den bekannten Abhängigkeiten von Albedo, Umlaufdistanz und Sternhelligkeit und stellt Beobachtungs-Entartungen fest, die dadurch für Ziel-Exoplaneten entstehen. Ein möglicher Magma-Ozean-Fall wird kurz für Venus und Mars diskutiert und mit den Ergebnissen der Untersuchung in Beziehung gesetzt.

PUBLICATIONS

Part of the following publications in peer-reviewed journals has been adapted with permission into the content of Chapters 3, 4, 5 and 6:

- Nikolaou, Athanasia, Nisha Katyal, Nicola Tosi, Mareike Godolt, John Lee Grenfell, and Heike Rauer (2019). “What Factors Affect the Duration and Outgassing of the Terrestrial Magma Ocean?” In: *The Astrophysical Journal* 875.1. DOI: [10.3847/1538-4357/ab08ed](https://doi.org/10.3847/1538-4357/ab08ed).
- Katyal, Nisha, Athanasia Nikolaou, Mareike Godolt, John Lee Grenfell, Nicola Tosi, Franz Schreier, and Heike Rauer (2019). “Evolution and Spectral Response of a Steam Atmosphere for Early Earth with a coupled climate-interior model”. In: *The Astrophysical Journal* 875.31. DOI: [10.3847/1538-4357/ab0d85](https://doi.org/10.3847/1538-4357/ab0d85).
- Odert, Petra, Helmut Lammer, Nikolai V Erkaev, Athanasia Nikolaou, Herbert IM Lichtenegger, Colin P Johnstone, Kristina G Kislyakova, Martin Leitzinger, and Nicola Tosi (2018). “Escape and fractionation of volatiles and noble gases from Mars-sized planetary embryos and growing protoplanets”. In: *Icarus* 307, pp. 327–346. DOI: [10.1016/j.icarus.2017.10.031](https://doi.org/10.1016/j.icarus.2017.10.031).

ACKNOWLEDGMENTS

This is going to be a long one. Thank you all. My family, without which I would have never come so far. Benji for the multi-faceted support, regardless of all the difficulties. Nicola Tosi for securing funding for me to work for 4.5 years. All the people that believed in my potential when they had no personal bias to do so: Frank Sohl for inclusivity in research and for giving me the chance to be in a science textbook for the first time, even with a minor contribution. Matthieu Laneuville and Marine Lasbleis for trusting me to give an interior dynamics introductory talk to the ELSI audience. Lena Noack for believing in me. Theresa Lüftinger for believing in me. Manuel Güdel and Tilman Spohn for interesting overview discussions on research. Nicolas Iro. Valerio Lucarini for support. Slava Solomatov for patient lengthy explanations of science and Keiko Hamano for insightful conversations. Vladimir Airapetian for support. Kristina Kislyakova and Colin Johnstone for team spirit on this and on the other side of the Atlantic. Raymond Pierrehumbert for the skiing. Heike for sharing with me her “darwinian selection on researchers” principle. Doris Breuer for being there when I needed her. Ina Plesa for being to me the paradigm of professionalism and collaborator that she is. Thomas Ruedas for endorsing me. Maria Pérez-Ortiz, Francisco Fernandez Navarro, Helmut Lammer, Petra Odert, John Lee Grenfell, Mareike Godolt, Nisha Katyal, Sabrina Schwinger and all coauthors.

Liuba Tupikina, my comradin, for supporting me from day 1 in Berlin until now. Alexis Tantet and Francesco Ragone, for talking through issues in fluid dynamics during walks around the Fattoria d’Asino. Eleftheria for the passion in research. Jessica and Aleke for bringing the Netherlands connection to the rescue. The “Niko” group of trustees. Miri and Irina for unceasing support since the Klimacampus years. Mikhail Khotyakov and Delphine Zemp for the trust. Matthaios Katsanikas for the trust. Daniel Meza for bottom-up hope building. My aunt Olympia for the letters. Mika Baqué for support. Alexandra, Maxime, Gianluigi, Hugo, Max, Falko, Solmaz, Alessandro, Mario, Claudia for support. Special thanks to friend and journalist Claudia Till for the support and for editing the german translation of this thesis’ abstract. I also thank Eleftheria Exarchou, Wladimir Neumann, Alexis Smith, Inga Kamp and Valerio Lembo for proofreading parts of this thesis.

The developers of Fortran and Python.

Those who told me to stop. They sent me back to the books, the most solid base of them all, in an ever moving science scene. Back to the basics. It is needed in more places than we think.

CONTENTS

1	INTRODUCTION	1
1.1	Planet formation	1
1.2	Magma ocean modeling legacy	6
1.3	Motivation of this study	8
1.4	Research questions	9
2	ELEMENTS OF THEORY AND METHODS	11
2.1	Theoretical foundations and assumptions in the MO	11
2.1.1	Bottom-up MO solidification	12
2.1.2	Lava lake as a MO surface analogue	12
2.1.3	Systems in thermal convection	13
2.1.4	Superfluids	17
2.1.5	Planck radiation distribution: application to magma ocean surface-atmosphere system	18
2.1.6	Runaway greenhouse atmospheric state	22
2.1.7	Magma ocean types	23
2.2	Brief numerical model overview	24
2.3	Structure of the interior	24
2.3.1	Melting curves	26
2.3.2	Melt estimation	28
2.3.3	Adiabat	29
2.3.4	Viscosity	29
2.3.5	The three convecting layers	35
2.4	Energy conservation	38
2.5	Outgassing	38
2.5.1	Solubility in a circulating fluid	40
2.5.2	Solubility curves for H ₂ O and CO ₂	41
2.5.3	Volatile mass balance	41
2.6	Secondary atmosphere	42
2.6.1	Grey atmospheric model	43
2.6.2	Line-by-line atmospheric model	45
2.6.3	Incoming stellar radiation	48
2.7	End of the magma ocean phase	48
2.8	Model constants	49
2.9	Experimental setting “Reference A”	50
2.10	Code flow	52
3	MAGMA OCEAN THERMAL EVOLUTION WITH A GREY ATMOSPHERE	53
3.1	Thermal and dynamical evolution	53
3.2	Outgassing and atmospheric build up	58
3.2.1	Mantle solidification and outgassing overview	58
3.2.2	Effect on relative outgassing with varying total volatile reservoirs	62

3.2.3	Partial pressure in a binary gas mixture	63
3.3	Effects of model parameters on the MO lifetime	65
4	QUALITATIVE PATHS IN THE MO THERMAL EVOLUTION	
	- RESULTS	71
4.1	Qualitative difference between grey and line-by-line radiative transfer atmospheric representation	71
4.2	Separating continuous from transient magma oceans	73
4.3	Role of orbital distance and albedo on magma ocean evolution	78
4.3.1	Dependence of F_{lim} on the melting temperature and steam mass	79
4.3.2	Limiting radiation values F_{lim} for pure steam	80
5	MO EVOLUTION ON OTHER PLANETS	83
5.1	Solar system planets	83
5.2	Exoplanets	84
6	DISCUSSION	91
7	CONCLUSIONS	99
	BIBLIOGRAPHY	101

LIST OF FIGURES

Figure 2.1	Bottom up solidification of magma ocean	13
Figure 2.2	Kilauea Volcano lava lake images	14
Figure 2.3	BB wavelength dependent radiation flux	19
Figure 2.4	MO solidification explanation with the use of melting curves and adiabat	25
Figure 2.5	Figure from Nikolaou et al. (2019) © AAS. Reproduced with permission. Variation of melt dynamic viscosity η_l with temperature for hydrous and anhydrous melt	32
Figure 2.6	Radioactive decay energy contribution per element	39
Figure 2.7	$OLR_{TOA}=f(T_{surf}, P_{H_2O})$ (Katyal et al., 2019) data product	47
Figure 2.8	COMRAD model code flow	52
Figure 3.1	Thermal evolution of black body (bb), grey H ₂ O atmosphere (gr-H ₂ O), grey H ₂ O/CO ₂ atmosphere (gr-H ₂ O/CO ₂), and line-by-line H ₂ O atmosphere lbl	54
Figure 3.2	Initial conditions, ΔT , u_{conv} and F_{conv}	55
Figure 3.3	Evolution of Pr and Ra parameters in a solidifying magma ocean	56
Figure 3.4	Solubility in silicate melt for volatiles H ₂ O and CO ₂	59
Figure 3.5	Evolution of H ₂ O and CO ₂ outgassing in Ref-A	60
Figure 3.6	Effect of melting curves on mantle melt fraction with potential temperature	61
Figure 3.7	Maximum relative outgassing of volatiles as a function of initial reservoir	62
Figure 3.8	Effect of binary gas mixture on species partial pressures	64
Figure 3.9	Colormap of solidification time for varying initial H ₂ O and CO ₂ reservoirs	66
Figure 4.1	Net outgoing radiation flux at TOA for (P_{H_2O}, T_{surf}) for grey and non-grey atmosphere	72
Figure 4.2	Figure from Nikolaou et al. (2019) © AAS. Reproduced with permission. Mechanism for separating a continuous (long-term) from a transient (short-term) magma ocean	76
Figure 4.3	MO thermal evolution using interior coupling with the lbl radiative transfer atmosphere	77

Figure 4.4	OLR _{TOA} as a function of surface temperature for varying atmospheric water content	79
Figure 4.5	Maximum albedo-distance combinations for continuous magma ocean with 4–300 bar steam atmosphere	82
Figure 5.1	Earth and Mars global magma ocean duration for variable volatile content	84
Figure 5.2	Example exoplanet candidates at distances suitable to for permanent, conditionally continuous and transient magma oceans	89
Figure 6.1	Cumulative plot of the sensitivity experiments for the solidification time t_s	93
Figure 6.2	Hydrodynamic escape of a Mars-size object atmosphere	95

LIST OF TABLES

Table 2.1	Parameter calibration of Giordano et al. (2008) viscosity	35
Table 2.2	Parameters used in radiogenic heat production calculation	39
Table 2.3	Model constants and parameters	49
Table 2.4	Reference-A setting parameter values and components	51
Table 3.1	Overview of the effects of various parameters on the solidification time	68
Table 4.1	$F_{lim}(P_{H_2O}, T_{RF,0})$ for two indicative $T_{RF,0}$ cases	80
Table 5.1	Planet and host star parameters used in Fig. 5.2	86

ACRONYMS

BB	black body
CAI	Calcium Aluminium-rich Inclusions
CAPE	Convectively Available Potential Energy
CMB	Core Mantle Boundary

COMRAD	COncvective Magma Radiative Atmosphere and Degassing model
ECS	Earth Climate Sensitivity
EM	Electro-Magnetic
EUV	Extreme Ultra Violet radiation (also XUV)
GARLIC	Generic Atmospheric Radiation Line-by-line Infrared Code
GCM	3D General Circulation/Climate Model
HC	Horizontal Convection; where ΔT is applied along the same bottom boundary oriented perpendicularly to the gravity vector
HITRAN	High-resolution TRANsmission molecular absorption database
IC	Initial Conditions
Vis	visible
IR	infra-red
KI	Kombayashi-Ingersoll limit (also Simpson-Nakajima limit)
LHB	Late Heavy Bombardment
lbl	line-by-line radiative transfer scheme
LTE	Local Thermodynamic Equilibrium
MO	Magma Ocean
OLR	Outgoing Longwave Radiation
RBC	Rayleigh-Bénard Convection
REE	Rare Earth Elements
RF	Rheology Front (:=40% melt volume fraction)
RG	Runaway Greenhouse state (\neq greenhouse effect)
TOA	Top Of the Atmosphere (uppermost radiating layer)
UV	ultra-violet
VC	Vertical Convection; where ΔT is applied across two boundaries oriented in parallel to the gravity vector
VFT	Vogel-Fulcher-Tammann equation of viscosity
XUV	Extreme Ultra Violet radiation (also EUV)

INTRODUCTION

The period of the magma ocean (MO) is a transient stage early in the accretion of rocky, also known as terrestrial, planets. With the term “magma ocean” one refers to an extensively molten silicate mantle and the geodynamical conditions associated with it. As of today the accretionary magma ocean state has two traits: it is a system both unobserved and with computationally incalculable dynamics. In particular, its numerical representation has not yet been explicitly computed because the demands for resolving this fluid dynamical regime exceed the contemporary calculation capability. It is hoped that future astronomical missions will remediate the first issue by extending the range of exoplanet observations and eventually capture that stage. In this work I treat the second issue by employing parameterizations that numerically represent the MO dynamics and thermal evolution. Resolving the thermal evolution and the accompanying degassing of that stage is the aim of this study.

What is a magma ocean

1.1 PLANET FORMATION

In order to understand the magma ocean origin it is vital to provide an overview of the planetary formation setting.

Planets are assumed to originate from disturbances of the circumstellar disk that is composed of gas and dust at uniform initial distribution in a flattened structure (Safronov, 1972). The circumstellar disk is alternatively called accretion disk because it loses mass and momentum to the gravitational potential well of the host star (D’Alessio et al., 2004). Astronomical observations of young accretion discs in our galaxy have been gathered through the SPHERE (ESO) instrument (Boer et al., 2016) and they reveal a range of possible dynamical configurations (Garufi et al., 2017). Within those, giant gaseous exoplanets form simultaneously to the evolving host star. Any rocky silicate planet is difficult to be detected within this environment due to the scattering of stellar light from the dust that is suspended in the gas (Klahr et al., 2006).

Circumstellar disks outside our solar system

Motivated by the recent discovery of exoplanets, the fields of astronomy, astrophysics and planetary physics gradually converge (Tasker et al., 2017). As a result, the views on planet formation have been expanded by introduction of otherwise long-standing facts known to accompany stellar formation. One such example is the consideration of stellar evolution simultaneously to the planetary formation. The star’s activity is also crucial to the disk characteristics because its radi-

*Uncertain dynamics
in the early
circumstellar
gas/dust disk*

ation affects the radial temperature distribution. In addition, the photochemical and magnetohydrodynamic interactions between star and disk affect the radial distribution of chemical compounds (Klahr et al., 2006). Moreover, the expected mass of the final planetary system is low compared to that of the host star. This suggests that efficient mass loss processes take place in the disk during its evolution (Klahr et al., 2006). Those dynamics are far from being understood (Nayakshin, 2011; Humphries et al., 2018) and constitute another astronomical observation that affects planetary formation views. In that light, the hypothesis of disk uniformity at the start of planetary accretion is gradually abandoned for more complex models (Haghighipour et al., 2016; Drażkowska et al., 2017; Unterborn et al., 2018).

*Pre-main sequence
and main sequence
stellar role*

The early effect of the star on planetary energy budget has not been quantified due to unresolved energetics and dynamics of its evolution at the pre-main sequence stage. Once that is reached for a G type star, thermal energy is generated at its core by fusion of H into He. Traits of a pre-main sequence star are the transfer of angular momentum away from the star into the disk (Klahr et al., 2006) and high intensity XUV/EUV emission (Güdel, 1997; Johnstone et al., 2018). The steady flux of XUV is also suggested to generate aminoacids, crucial for the development of pre-biotic chemistry (Airapetian et al., 2017), and is potentially important for explaining the emergence of life on a planet. Despite those advances, the uncertainty in the stellar background that is contemporary to the MO remains high. At the beginning of Sun's main sequence, the lower luminosity compared to today's level, known as "faint young Sun" (Feulner, 2012), is one of the few hypotheses that is widely accepted. The reason is that the main sequence is a well studied stage of stellar evolution.

*Planetary system
formation upon
condensation of the
Calcium
Aluminum-rich
inclusions*

The initial composition of the gas and dust disk remains unknown. It is expected to reflect the chemistry of the host star. However, the bulk planetary composition of Earth is depleted with respect to the solar abundances of Si and Fe by up to 20% (H. S. Wang et al., 2019). This implies that the composition of the resulting planets cannot be explained by in situ formation of each planet from the solar composition alone (Dorn et al., 2017). Since astronomical observations in T-Tauri circumstellar disks have high uncertainty in the mid-plane and lower uncertainty at the disk rims, initial disk temperature, composition and total mass are not yet constrained, as well as the gas to dust ratio. This has direct consequences in the propagation of radiation and introduces uncertainty in the temperature distribution of the disk. The latter is particularly important for estimating when and at what radial distance each element condenses from the gas phase (H. S. Wang et al., 2019). The radial distance at which the water vapor condenses is in particular referred to as the snow line. The point in time when the temperature drops below the sublimation temperature of solid Calcium Aluminium-rich Inclusions (CAI), τ_{CAI} , is assumed

to be the starting point of the planetary system (Bouvier et al., 2010). Following that definition, the formation point in time for our solar system is 4.566 ± 0.002 Ga (Allègre et al., 1995; Bouvier et al., 2010). From there onward the planet formation process ensues.

There are various theories that suggest how accretion of dust onto planetesimals initiated (Klahr et al., 2006). Ultimately, impacts between protoplanetary bodies grew the terrestrial planets to their final masses, while the gaseous giant planets' formation preceded them (Morbidelli et al., 2005; Raymond et al., 2017). Especially for the case of Earth more than one impactors are required, in order to justify its large mass relatively to the other rocky planets (Tonks et al., 1993; Izidoro et al., 2014; Haghighipour et al., 2016) and its relative noble gas isotopic abundance (Odert et al., 2018; Lammer et al., 2018). Numerical N-body simulations suggest a few tens up to a hundred million years for the formation of Earth (Wetherill, 1990; Raymond et al., 2006; Haghighipour et al., 2016).

The kinetic energy of impactors, the gravitational potential energy released during core-mantle differentiation and the contribution of heat from decay of short-lived radionuclides are generally thought sufficient energy sources to melt part or all of the Earth's mantle according to prior estimates (Coradini et al., 1983; Melosh, 1990; Tonks et al., 1993; Rubie, 2015). Although it is supported by energetic arguments during rocky planet formation it is not known when the MO stage started. In the case of Earth, the widely accepted hypothesis for the last impact in sequence was the Moon-forming "Theia" impactor at 60 Myr after τ_{CAI} (Barboni et al., 2017), a Mars-size body that extensively melted Earth's mantle (Wetherill, 1990; Canup, 2004; Sleep et al., 2014). The fluid magma ocean environment is favorable for the differentiation of the impacted body into core and mantle. Apart from mass and energy delivery, the impactor sequence is also suggested to have left a signature in the noble gas mass fractionation record due to atmospheric escape (Odert et al., 2018; Lammer et al., 2018).

The uncertainty in accretion sequence (Izidoro et al., 2014; Haghighipour et al., 2016; Raymond et al., 2017) propagates as uncertainty in the timing and quantity of volatile delivery during the MO phase. The suitable combination of proportions from various meteorite populations, that matches both the chemical and isotopic signature of Earth composition, is an issue of continuous research. Isotope geochemists classify the meteorite materials according to their differentiation between primitive and evolved compositions. It is suggested that lower Earth's isotopic composition is closer to that of enstatite chondrites (Javoy et al., 2010; Dauphas, 2017) which are poor in volatiles. Water-rich carbonaceous chondrites are suggested to contribute 10–15% of mass early in the planetary accretion (Braukmüller et al., 2019). A late (3.8 Ga) heavy bombardment (LHB) hypothesis of water-rich impactors was suggested to explain the differences of bulk Earth compo-

*From dust to
protoplanets*

*Magma ocean stage
to occur during
planetesimal and
protoplanetary
accretion*

*Uncertainty in the
accretion dynamics
affects the initial
volatile inventory of
the planets*

sition with meteorite populations (Fischer-Gödde et al., 2017). Original ideas for orbital dynamics of the solar system have been introduced to reproduce this event, such as the Nice model (Morbidelli et al., 2005; Tsiganis et al., 2005) which assumes the Grand Tack scenario to serve as initial condition. This scenario requires an inward migration of gas planet Jupiter and Saturn that disturbed the orbital stability of wet impactors beyond the snow line. This caused them to migrate inwards and deliver volatiles to the inner solar system planets. However, the mere presence of giant planet Jupiter is sufficient to destabilize planetesimals that orbit beyond the snow line (Raymond et al., 2017) and renders the Grand Tack scenario a possibly unnecessary dynamical complication (Izidoro et al., 2014; Haghighipour et al., 2016).

*Uncertainty for the
initial Earth H₂O
inventory*

For the case of water, the hypotheses in literature range from the conservative estimate of the currently observable one ocean reservoir (Lebrun et al., 2013; Hamano et al., 2013) up to 10-fold ocean water worth stored in the deep mantle (Hirschmann, 2006; Hirschmann et al., 2009, 2012; Hallis et al., 2015; Tschauner et al., 2018). Data from the Rosetta mission (Altwegg et al., 2015) reveal that only 1% of the ocean and atmosphere water is compatible with cometary origin. Moreover, the LHB does not remediate the lack of volatiles in the rocky planets as it likely originates from the inner solar system (Fischer-Gödde et al., 2017) which is drier than the outer part. Due to the above uncertainties, the delivery of water in planets remains an unresolved issue.

*Uncertainty for the
initial Earth CO₂
inventory*

Similar uncertainty holds for the amount of CO₂ inventory. The low solubility of CO₂ in silicate melts indicates that its delivery is not straightforward. Chemical conditions have to be taken into consideration for the form in which carbon was delivered. On modern Earth's observable reservoir the majority resides in carbonates in the oceanic crust (Ingersoll, 2013) and a minor portion in the atmosphere. A large portion of Earth's carbon is assumed to exist in the core (Dasgupta et al., 2010) where FeC alloys could be used to explain core seismicity (Chen et al., 2018). Part of the oxygen could also reside atop the core-mantle boundary CMB in the form of silicate oxides (Hirose et al., 2017).

*Physical and
chemical processes
that affect volatile
content in the
magma ocean*

For the chemically inert noble gases such as Ar, He and Ne (Olson et al., 2018) ingassing into the magma ocean is expected to occur, due to ambient pressure of the enveloping protoplanetary nebula. Such process follows Henry's law. Based on observations, the nebula is assumed to dissipate after 10 Myr (Mamajek, 2009). Therefore the ingassing occurs on planetary cores that were completed within this time frame. Mars could have been formed within that period (Hansen, 2009), while Earth requires ~ 60–100 Myr (Wetherill, 1990; Raymond et al., 2006) when such process becomes irrelevant. The dissolution of chemically reactant volatile species into ions in the silicate melt is more difficult to estimate. That is because a solution constitutes

a chemical process and is characterized by a reaction constant that depends on the oxidation state (Schaefer et al., 2010). Such process follows solubility functions that are experimentally defined for silicate melts (e.g. Carroll et al., 1994; Pan et al., 1991). Moreover, there is ongoing debate as to whether the net contribution of volatile mass from the competing effects of impactor-induced atmospheric escape and impactor mass delivery is positive (Ruedas, 2017; Lammer et al., 2018; Sakuraba et al., 2019) or negative (Massol et al., 2016; Ikoma et al., 2018) for the volatile inventory of the target planet.

Because of all the aforementioned uncertainties, the volatile inventories are assumed as parameters in the magma ocean modeling studies (Elkins-Tanton, 2008, 2012; Lebrun et al., 2013; Salvador et al., 2017; Hamano et al., 2013, 2015; Massol et al., 2016; Bower et al., 2018; Ikoma et al., 2018).

It would be a very helpful constraint to have the timing of the first solid surface on Earth. The mineral which comes up more often in the literature of oldest samples on Earth is the zircon. Zircon is a silicate mineral with resistance to weathering. Its low diffusivity rate of oxygen makes it suitable to study oxygen isotope abundances that existed at the time of its formation, preserved from ambient contamination. The item zircon W74/2-36, dated 4.404 ± 8 Ga, Jack Hills, Australia is the oldest terrestrial sample found to date (Peck et al., 2001). Younger zircons of 3.910–4.280 Ga age were found in the same area (Mojzsis et al., 2001).

*Oldest geological
sample on Earth at
4.4 Ga*

Zircon saturation temperatures have been calculated to determine the temperature at which the parent magma began to crystallize it. For this mineral phase, the saturation temperatures of sanukitoids range within 700–800°C (King et al., 1998; Watson et al., 2005).

Since the Hadean (4.6–4.0 Ga) Earth was intensively bombarded, impact features are expected to be common, but those zircons have not been affected by shock metamorphism (Peck et al., 2001). None of the Jack Hills zircons older than 4 Gyrs exhibit shock lamellae or other crystallographic features characteristic of shock metamorphism (e.g. Berg et al., 1985).

Since they lack signs of shock metamorphism they are representative of the local planetary conditions at the time. It is unclear if the pressure conditions at which the zircon enrichment of $\delta^{18}\text{O}$ occurred can be derived from the samples. From the Rare Earth Elements (REE) abundances one can constrain the origin (magmatic or hydrothermal) and the age, but not the depth at which this occurred. “Surface” or “near surface” conditions, are assumed (Peck et al., 2001; Mojzsis et al., 2001) with the surface being implicitly defined as a known standard, but not quantified. One interpretation of the findings suggests water ocean at the surface (Valley et al., 2002). In particular, the Oxygen isotopic fractionation value is attributed to liquid water that efficiently hydrated the crust (Mojzsis et al., 2001). However the U/Pb

clock has been erased due to Pb removal, and this should not have occurred if water was acting as a passive solvent according to Hoskin (2005). Another hypothesis is that crust, that has interacted with water and was then geodynamically reprocessed (Bell et al., 2014), did enrich the melt from which the zircon later precipitated (Mojzsis et al., 2001).

In overview, the zircons' analysis indicates wet parent melt, at 973–1073 K (King et al., 1998; Watson et al., 2005) located at or near the surface. This zircon precipitation is not a product of passive water solvent-silicate mineral interaction. No large scale surface water volume, but rather ephemeral water of volume significant compared to the specific volume of the zircon parent melt, is sufficient to interpret the 4.27 Ga zircon hydrous alteration (Hoskin, 2005). Those formation conditions date within 300 Myr from the beginning of the solar system, are not direct observables of impacts and likely postdate any episodes of terrestrial magma ocean that occurred during the first 100–300 Myr post τ_{CAI} time, including the moon forming large scale melting at 60 Myr (Barboni et al., 2017). Therefore, they indicate that some solid surface had been formed by that time and that the local parent melt was rich in water content. Modeling of the MO stage evolution is necessary to help assess which processes lead to those conditions.

The next available samples are dated at 3.8 Ga (Archean era) (Kröner, 1985; Wetherill, 1990) and additional constraints on the surface pressure conditions are derived from 2.7 Ga (Archean era) samples (Ueno et al., 2009; Endo et al., 2016). This reveals a period of stagnation in observations that is only addressable through modeling. Initial conditions to those models can be provided by the latest thermal evolution of the magma ocean stage.

1.2 MAGMA OCEAN MODELING LEGACY

A mixture of theoretically predicted properties along with proxy conditions found on modern Earth are used in order to describe the MO stage in numerical simulations. As seen above, a lot of its parameters such as the volatile inventory of the planet and composition consist assumptions with high uncertainty. The theoretical work of Abe et al. (1985, 1988), Nakajima et al. (1992), and Abe (1993, 1997), Coradini et al. (1983) and the seminal work of Solomatov et al. (1993b,a) and Solomatov (2007) in the early 80s–90s set the ground for describing the system's thermal evolution by implementing secular cooling and parametrized dynamics. The thermal blanketing of the atmosphere was also considered. Those foundations are ubiquitous in posterior MO studies (Elkins-Tanton, 2008; Lebrun et al., 2013; Monteux et al., 2016; Salvador et al., 2017; Hier-Majumder et al., 2017; Bower et al., 2018; Unterborn et al., 2018; Miyazaki et al., 2019a,b). The later works of

Elkins-Tanton (2008, 2012) and Lebrun et al. (2013) have enriched the pool of modeling approaches by adapting the prior works into simple and comprehensive computational tools, while including additional physical aspects of the system. Such is the parameterized crystallization sequence of minerals in the mantle (Elkins-Tanton, 2012) and the coupling with a k-correlated radiation absorption model (Marcq, 2012; Lebrun et al., 2013) that improved the thermal response of the atmosphere to the MO exsolved heat. The works of Hamano et al. (2013), Marcq (2012), Lupu et al. (2014), Wordsworth et al. (2013b), and Schaefer et al. (2016) that followed, further elaborated the role of the atmospheric component. Expanding on the findings of previous models, they provided crucial information on the vapor saturated atmosphere radiative response. Hamano et al. (2013) first associated the runaway greenhouse atmospheric phenomenon with the MO evolution path and the solar luminosity evolution. Especially Wordsworth et al. (2013b, 2018) paradigms further constrained the atmospheric radiative effects. The latter mainly brought expertise from the Earth climate modeling which is the most mature among planetary climates due to the wealth of ground truth/in situ and remote observations, followed by the Mars climate modeling (Angelats et al., 2005) that has recently reached daily atmospheric condition predictive capability (Rems project et al., 2013).

Recently, advances in the chemical understanding of processes that occur at the MO pressure and temperature conditions, have been introduced in the modeling treatment (Schaefer et al., 2010; Fegley et al., 2014; Gaillard et al., 2014; Schaefer et al., 2017). There, the evolution of chemical properties (fugacity, volatile solubility) between atmosphere-melt is resolved for a wealth of gas species assuming quasi-static chemical equilibrium. Deguen et al. (2014) and Boukaré et al. (2015) examined the chemical interactions and mineral formation during differentiation into mantle and core. Two-phase flow modeling was introduced by Boukaré et al. (2017), Bower et al. (2018), and Miyazaki et al. (2019a,b) in order to refine the effect of phase separation on the bulk thermal properties and to resolve the percolation of melt through the solidified mantle while accounting for compaction of the solid matrix (Hier-Majumder et al., 2017).

Two-dimensional modeling studies (Maas et al., 2015, 2019) together with new laboratory experiments by Shishkina et al. (2016) explore the dynamical evolution of vigorous convective regimes similar to those the MO is estimated to have. By approaching the estimated convective regimes of the MO they provide the closest comparisons to the predicted ultimate convection regime (Kraichnan, 1962; Grossmann et al., 2000). The onset of solid state convection of the terrestrial solid mantle is a precursor of plate tectonics and constitutes another important milestone in Earth evolution. Its relative timing with respect to the magma ocean period, simultaneous or posterior, becomes a

crucial matter. While this is a likely scenario for slowly solidifying magma oceans, establishing whether and to what extent the solid mantle convects during the MO early stages is beyond the scope of this study since this would require the use of fully dynamic simulations (e.g. Maurice et al., 2017; Ballmer et al., 2017).

Apart from certain studies in 2D that focus specifically on MO convection dynamics in a rotating framework (Maas et al., 2015, 2019), the remaining aforementioned processes are implemented exclusively in 1D model configurations. This has matured and technically improved the 1D modeling. However, the physics of magma ocean remains unconstrained and one of the reasons is lack of a benchmark that could help systematize the technical elaboration of the problem by the research community.

1.3 MOTIVATION OF THIS STUDY

The particularity of the MO system, as with most simulations, is that many physical properties are not explicitly resolved and they have to be assumed for. This is common in many problems in physics and constitutes no deviation from the traditional scientific approach. The difference here is that most of the properties that have to be assumed for belong outside the range of experimental validation and do not have astronomical observation coverage. In those cases the physical properties of the system are retrieved from extrapolations of laws that are confirmed in the range covered by experiments.

There is an extensive legacy of models for the MO. However, comparing results from the literature is not straightforward because each magma ocean study involves many ad hoc assumptions. This is inevitable since different research fields focus on a specific niche of the MO system. At the same time, the topic is becoming increasingly multidisciplinary (Tasker et al., 2017) and more of the assumptions are being challenged.

In that setting, it is vital to revise the underlying assumptions and their effect on the numerical simulation of MO evolution. In my thesis I devised a model of intermediate complexity on which a hypothesis can be easily tested, to serve that primary aim.

Main research goal

The presentation and analysis of results is centered around the question: *What is the magma ocean duration?* The direct goal is to estimate the time scale of the MO lifetime.

During thermal evolution, the volatiles that envelop the terrestrial planets are crucial since they quantify the effect of thermal blanketing that delays radiative cooling of the MO by hundreds of thousands of years. This is a known effect but it is poorly explored in the MO geodynamic setting. I therefore choose to set the atmosphere-interior coupling as the minimum modeling base and for resolving the simultaneous volatile degassing from the interior into the atmosphere.

Capturing the energy balance between interior and atmosphere provides the suitable background on which the thermal evolution and the evolution of physical characteristics can be described. In this work I also examine the effect of additional physical parameters, assumptions and processes and I rank them in significance according to the control that they exert on the MO duration. Knowing their relative significance can help guide future model development. The intermediate model complexity keeps the findings comprehensible and it is introduced as a benchmark paradigm.

Through this approach, the MO duration operates as a “kaleidoscope” of comparison to the time scales of various processes. Calculating the MO duration helps evaluate the contemporary processes on their relevance to the planetary evolution. Such are the first hundred Myr of stellar evolution (Tu et al., 2015; Johnstone et al., 2015, 2018), the hydrodynamic escape processes, the frequency of impactors and statistically estimated average time between consecutive impacts, time of oldest known surface $t_{CAI+160}$ Myr (Valley et al., 2002).

I primarily account for the key role of the outgassed atmosphere. Moreover, I examine the specific role of each physical process and parameter included in the model and identify their effect on the thermal evolution, with respect to a simple reference setting of parameters. To this end, I developed and used a 1D interior model with two alternative representations for the atmosphere: i) a grey atmosphere of H_2O and CO_2 , and ii) a line-by-line atmosphere of H_2O only (Katyal et al., 2019). The result is a model of coupled thermal evolution.

Additional research objectives

1.4 RESEARCH QUESTIONS

In this work I address the following research questions:

- Q1 What are the geodynamic characteristics of a solidifying MO during the thermal evolution of the atmosphere-interior coupled system?
- Q2 How was the secondary atmosphere formed following the evolution of volatile outgassing from the magma ocean?
- Q3 How long does the MO last with respect to every physical process included in the simulations?
- Q4 How does MO evolve with distance from the host star and how is it affected by planetary composition?
- Q5 How is the magma ocean on planets other than Earth? What are the likely MO cases for rocky planets (Venus, Mars) and exoplanets?

*If, unwarned by my example, any man shall undertake and shall succeed,
in really constructing an engine embodying in itself
the whole of the executive department of mathematical analysis
upon different principles or by simpler mechanical means,
I have no fear of leaving my reputation in his charge,
for he alone will be fully able to appreciate
the nature of my efforts and the value of my results.*

Charles Babbage (1864)

Numerical representation of the model's processes and their accuracy level is better understood and appreciated with the introduction of their theoretical foundations. Below I introduce those of energy radiation, the convection classical paradigm, states of matter found in the MO system, the magma ocean type studied in this work and the lava lake terrestrial analogue that guides the MO phenomenology. The remainder of this chapter consists of: the technical description of each model process, the setting of a numerical experiment used in the following as a reference and a diagram of the code flow. To aid the reader, a list of the acronyms used throughout the study is found at the beginning of the manuscript.

2.1 THEORETICAL FOUNDATIONS AND ASSUMPTIONS IN THE MO

"The 1D modeling of the MO is relatively easy because it is a theoretical stage that can accommodate versatile assumptions, while its numerical representation is aided by the homogeneity assumed in the convecting volume" (R. Wordsworth, "Environments of Terrestrial Planets Under the Young Sun: Seeds of Biomolecules" Sellers Exoplanet Environments Collaboration Symposium, Greenbelt MD, USA, April 2018). While is true that most of the magma ocean aspects can be represented using a 1D modeling approach ignoring lateral inhomogeneities, certain aspects of the MO theoretical conception are not straightforward. Some phenomena are not accommodated in a modeling approach because the available tools need to be adapted wherever possible or new methods have to be eventually devised or imported from other fields. I introduce those issues below, with the aid of visual means whenever necessary.

*In a model, it is
important to know
how far we are from
the truth.*

2.1.1 Bottom-up MO solidification

The primary counter-intuitive effect about the MO is that it solidifies from its bottom upwards (Solomatov, 2007) and not from its surface that is exposed toward cold outer space. A schematic representation of the bottom-up solidification of the Earth magma ocean, in a spherically symmetric model, is shown in Figure 2.1, redrawn after (Solomatov, 2007). The circles represent crystals that start forming within the MO convecting environment. At each instant in the evolution, the magma ocean extent identifies with the depth D within which liquid-like convection takes place. As a result, at all times, a liquid layer overlays a solidified one. During cooling of the system its liquid volume shrinks upwards as the so-called rheology front (dashed line), moves from the Core Mantle Boundary (CMB) towards the surface. The rheology front (RF) is a boundary that separates liquid-like from solid-like fluids and develops with radial symmetry. According to Tonks et al. (1993), This symmetry is justified by the isostatic adjustment of the melt that spreads out on the surface forming a layer of uniform depth. The technical and quantitative definition of RF is introduced in Section 2.3.

Alternative views based on ab initio calculations of the thermodynamic properties of silicate liquids, attempt to address the mantle chemistry at depth (Stixrude et al., 2009) and contradict the MO solidification from the bottom. Labrosse et al. (2007) suggest formation of an adjacent to the mantle base, therefore “basal”, magma ocean. The hypothesis outlines as follows: the first crystals form at a layer, mid-depth of the convecting MO, such that liquid-like fluid is located both below and above it. Two rheology fronts are defined at each boundary of the solid-like layer with the neighboring domains. The rheology fronts propagate downward (toward the CMB) and upward (toward the surface), respectively, commencing the crystallization process at the middle. This justification requires stability analysis of the mid-layer of crystals in the convective flow, based on chemical and physical characteristics of the crystals and calculation of transport, and of local mixing by quantifying local turbulent thermal and momentum diffusivity. This issue stretches the 1D model capabilities (Laneuville et al., 2018) and requires 2D modeling to be addressed in detail. As of today, the most prominent hypothesis in agreement with experimental data of mantle melting properties at depth is the bottom-up solidification (Solomatov, 2007).

2.1.2 Lava lake as a MO surface analogue

The magma ocean surface cools while located on top of a vigorous convective liquid silicate volume. The non-dimensional parameters of the magma ocean yield boundary layer thickness that equals few

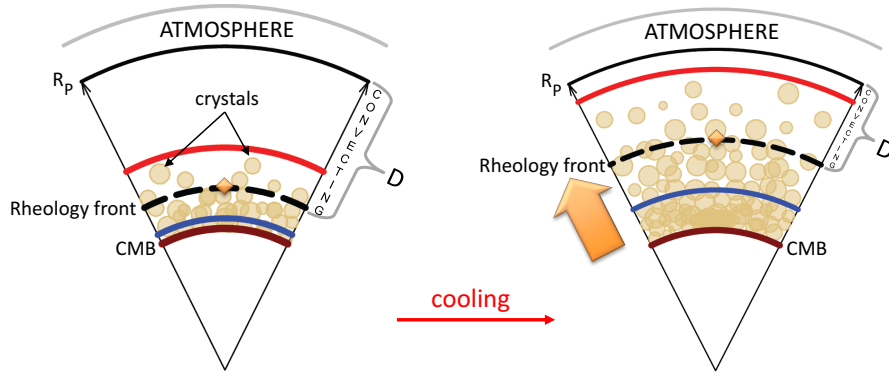


Figure 2.1: Schematic representation of the bottom-up solidification of the Earth magma ocean in a spherically symmetric model redrawn after (Solomatov, 2007). The circles represent crystals forming from the bottom up within a convecting environment. At each instant in the evolution, the magma ocean extends up to the depth of liquid-like convecting region D . During cooling of the system its volume shrinks as the rheology front (dashed line), moves from the CMB towards the surface. Outgassing of the secondary atmosphere occurs simultaneously to solidification. Diagram is not to scale.

mm (Lebrun et al., 2013). Lebrun et al. (2013) equates this to crustal thickness. That crust is prone to fragmentation due to the disturbing stresses of upwelling and downwelling currents. Moreover, the crust cannot support a significant thermal gradient between the cooling top and the above melting point bottom across its limited mm-scale thickness.

A resurfacing lava lake is assumed to be an analogue of the MO surface conditions. Two snapshots of a lava lake with 15 minutes difference are recorded with a thermal camera and shown in Figure 2.2. The mafic crust is generated at an upwelling plume at the upper right and sinks on the lower right rim of the lake where it remelts and gets recycled upon sinking. The pattern is indented with plates that break under the vigor of underneath circulation while their brief flow along the surface (20cm/sec) suggests surface renewal. Viscosity in the lava lake is 6–7 orders of magnitude higher than the estimated viscosity of the magma ocean, which would contribute to a more rapid circulation in the latter, reinforcing the case for resurfacing.

2.1.3 Systems in thermal convection

Here, I separately introduce the phenomenon of thermal convection. It is the main physical process that is parameterized in the system and enables the coupling of atmosphere to the interior.

Every heat transfer process obeys the same thermodynamic laws where: (i) energy is conserved in an isolated system and only trans-

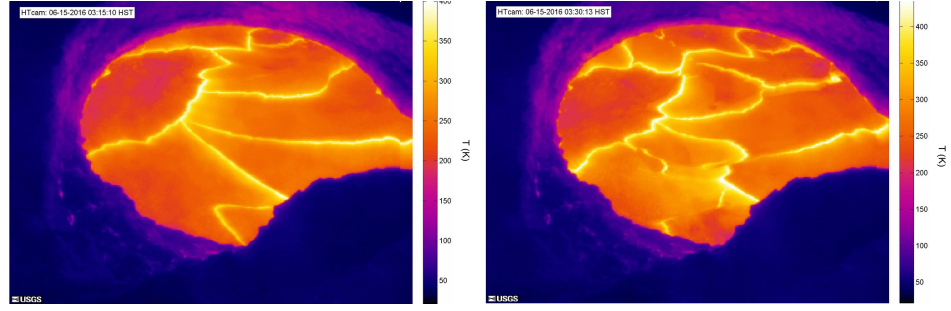


Figure 2.2: Consecutive thermal images of Halema'uma'u vent lava lake on Kilauea Volcano, Hawaii, 2016 demonstrating rapid resurfacing (observed plate motion 20 cm/sec, USGS). **Left:** lake at t_0 . **Right:** lake at $t_0 + 15'$. In 2018 the magmatic system depressurized, and the lake has since drained. Image credit: USGS, Hawaiian Volcano Observatory.

forms from one form to another, (ii) entropy generation tends to reach a maximum in an isolated system at equilibrium, (iii) at absolute zero entropy reaches a constant minimum. The three physical mechanisms of thermal energy transfer are conduction, convection and radiation. To the end of satisfying thermodynamic equilibrium, each of them develops into a different dynamical regime.

Which mechanism will take place depends on the physical properties of the means through which the heat propagates. It also depends on its state of matter. This way, in a stellar atmosphere, convection versus conduction are evaluated versus the Schwarzschild criterion. According to the latter a superadiabatic temperature gradient denotes that convection takes place. In a liquid system, such as a large water volume located within a gravity field in hydrostatic equilibrium state and that is heated from below, heat conduction prevails for slow heating rates (when heat dissipation is faster than momentum dissipation). Convection ensues when viscous friction cannot hinder the sufficiently large buoyancy forcing that originates from the heat source located at the bottom. In the case of solids, conduction dominates in short time scales while in long time scales convection takes place (Jaupart et al., 2011).

In this study, the modeled system is composed of three layers of geophysical fluids that all convect and dispose of heat at their upper boundaries (opposite to the gravity vector direction). Those layers are: the liquid mantle (MO), the solid mantle, and the lower part of the atmosphere. Convection occurs at a different time scale for each.

2.1.3.1 The Rayleigh-Bénard Convection paradigm

In this study I employ convection after the Rayleigh-Bénard convection paradigm (RBC) (Rayleigh, 1900).

Historically, RBC has been one of the most studied regimes in fluid dynamics. It is both relevant in problems of geophysics, for exam-

*The RBC hypothesis
adapted to the MO
problem.*

ple convection in the atmosphere, and in astrophysics, as is for example seen in the convecting solar photosphere. Besides buoyancy, other forcings become important in the wider solar system convection paradigms. Such is the rotation of a planet and magnetism in planetary cores and in the convecting ionized gas within the Sun.

The [RBC](#) setting is described as follows: a fluid is confined between two parallel rigid boundaries at different temperatures, the highest of which is applied at the bottom boundary. Initially, the fluid is found in static equilibrium in response to a gravitational field. The bottom heating perturbs the hydrostatic density profile. If the Rayleigh (Ra) number, which is the ratio of buoyancy forcing against viscous friction, is sufficiently high, the potential energy of the lighter warm fluid accumulated at the bottom converts into kinetic energy and overturning of the fluid volume ensues, aided by symmetric response from the top cold sinking layer. The external boundary condition of prescribed T is a source of potential energy that opposes the stable stratification of the system. Simultaneously, viscous dissipation operates as an energy sink to the system. In the [RBC](#) setting both forcings exist perpetually (Glatzmaier, 2013).

The fluid equation of state relates the density ρ to temperature T and composition X : $\rho = f(T, X)$. Density primarily depends on temperature, and perturbations to the hydrostatic ρ profile result in buoyancy forcing. At thermal convection it is assumed that density perturbations are exclusively produced by temperature differences. A second source of density perturbations is the inhomogeneous concentration of a substance. Here, such effect is neglected.

It is also assumed that any lateral variation of density is negligible with respect to the vertical variations. This approach is also known as Boussinesq approximation of the analytical expression of the system's Navier-Stokes equations. From their non-dimensionalisation one obtains the Nusselt (Nu) number: ratio of convective to conductive heat flux, the Prandtl (Pr) number: ratio of kinematic viscosity to thermal diffusivity and the Rayleigh (Ra) number: ratio of buoyant forcing to viscous friction.

Follow the definitions of Rayleigh (Ra) and Prandtl (Pr) number:

$$Ra = \frac{\rho \alpha_T g (T_p - T_{surf}) D^3}{\kappa_T \eta}, \quad (2.1)$$

$$Pr = \frac{\eta}{\rho \kappa_T}, \quad (2.2)$$

where ρ is the density, α_T the thermal expansivity, g the gravity acceleration, T_p the mantle potential temperature, T_{surf} the surface temperature, D the depth of the convective layer, κ_T the thermal diffusivity, $\frac{\eta}{\rho}$ the kinematic viscosity and η the dynamic viscosity.

Technically, the configuration in which the buoyancy forcing is applied with respect to the domain boundaries can differ. This widens

the experimental settings for investigation. Other than the Rayleigh-Bénard Convection (RBC) configuration there is the horizontal convection (HC) where the temperature difference is applied exclusively along the same surface (Shishkina et al., 2016). A geophysical example of HC is the water ocean surface warmed under modern climate's latitudinally variable temperature forcing (Rossby, 1965). There is also vertical convection (VC) where the boundaries of different temperatures are parallel to the gravity vector (Shishkina, 2016). All those experiments aid in studying the heat propagation efficiency and its various dependences.

*Elements of
Grossmann-Lohse
theory*

2.1.3.2 *Nu-Ra scaling of heat propagation in the RBC*

The quantity of main interest for this study is the heat flux (F) disposal in an RBC setting. A brief overview of the recent advances in its study, that are relevant in the context of magma ocean, is found below. The model details will be introduced in Section 2.2 onwards.

The RBC heat flux parameterization includes elements of the mixing length theory and according to the Kraichnan (1962) formulation it describes a solution to the “turbulence closure” problem (Birkhoff et al., 1960). This heat flux scales as a power law known as “Nu-Ra scaling”:

$$\frac{FD}{k\Delta T} = Nu \sim Ra^\beta \quad (2.3)$$

where β is $\frac{1}{3}$. This relation is assumed to asymptotically converge toward a constant scaling at high Ra values (Niemela et al., 2000b,a; Jaupart et al., 2011).

Recent experiments.

The MO is generally described by low Pr and high Ra numbers, therefore it is of direct interest to confirm if the scaling is preserved at those conditions. In their most recent relevant work, Shishkina (2016) and Shishkina et al. (2016) provide a detailed overview of the Nu-Ra scaling in various convecting regimes according to the Grossmann et al. (2000) theory. In their work they extended RBC to HC and compared it to the RBC at high numbers using the similarities with Grossmann et al. (2000) theory. The highest β exponent they find is $\frac{1}{3}$.

Shraiman et al. (1990) assume: $Nu \sim Ra^{2/7} Pr^{-1/7}$ which is the hard turbulence regime used in Solomatov (2007) and includes a dependence on Pr and aspect ratio of the mean flow λ . Shraiman et al. (1990) assume a turbulent boundary layer and a thermal boundary layer nested therein which was predicted by Kraichnan (1962) and would result in: $Nu \sim Ra^{1/2}$. This corresponds to the so-called “ultimate” regime of convection (Shraiman et al., 1990; Siggia, 1994) that is predicted for high Ra . This is a theoretical state (Lohse et al., 2003) yet not experimentally confirmed neither in the laboratory, nor numerically. Recent numerical experiments in 2D (Grossmann et al., 2011) and 3D (Blass et al., 2019) aimed to invoke the ultimate convection

regime by applying shear to the turbulent boundary layers. They revealed only transient dynamics by observing a raise of the $Nu-Ra^\beta$ coefficient to $\beta = 0.38$, which is lower than the theory-predicted $\beta = \frac{1}{2}$.

The flow tends to self-organize in circular convective cells. The circular shape demonstrates minimal curvature and as such minimizes the viscous resistance to buoyancy and to the diffusion of any temperature perturbation (Glatzmaier, 2013). Therefore it is usual to assume the cell aspect ratio to be 1 in numerical simulations. However, the experiments show that convective cell geometries may differ from 1 and also have an effect on the heat flow efficiency (Shishkina, 2016).

In an alternative effort to obtain details of the flow in 2D, Maas et al. (2015, 2019) rescaled the convecting MO problem to resolvable non-dimensional Ra and Pr parameters. By focusing on the effect of planetary rotation, that is expected to be important in the circulation of low viscosity fluids (Read, 2009), they found it could prevent the settling of crystals entrained in the buoyancy driven flow.

2.1.4 Superfluids

In the thermodynamic conditions typical of the MO stage all three physical states (solid, liquid and vapor) occur naturally within the coupled system. However at certain (P, T) ranges some of the chemical compounds are found in supercritical state of matter:

1. Water vapor reaches criticality at temperature above $T_{crit} = 647$ K and $P_{crit} = 220$ bar and beyond. In order to describe its properties in the atmosphere Hamano et al. (2013, 2015) use expressions for the thermal capacity c_p and the thermal expansivity α_T that are based on data within 130–2000 K (Woolley, 1980). Newest data extend the properties to $P = 500$ bar and $T = 2273$ K (Kretzschmar et al., 2019). Depending on the initial assumptions, those conditions are reached during the magma ocean thermal evolution.
2. Silicate fluid that is found above critical pressure (Makhluf et al., 2017; Manning, 2018) also becomes supercritical. As a consequence, the interval of fractional melting is not defined during experiments at these conditions because the phases are not experimentally detectable. Mibe et al. (2011) state that “the melting temperature can no longer be defined beyond this critical condition and that the fluid released from water rich minerals at depths greater than 100 km is supercritical fluid rather than aqueous fluid and/or hydrous melts.” Outside this interval the mineral phase coexists with a phase that has properties of a hydrous liquid (Manning, 2018). The critical point is located at conditions $P = 3.4$ GPa and $T = 770^\circ\text{C}$ according to Mibe et al.

(2011) and at $P = 5.5$ GPa and $T = 1050^\circ\text{C}$ according to Kessel et al. (2005) in hydrous basalts.

By definition, the interface between vapor and liquid state of the compound disappears at supercritical state. Firstly, this makes unfeasible the definition of water condensation point. Secondly, it introduces an uncertainty to the melting temperature of the water rich silicate minerals at pressures beyond 3.4 GPa.

2.1.5 Planck radiation distribution: application to magma ocean surface-atmosphere system

Assume a state of thermodynamic equilibrium. Let the distribution of energy in the radiation spectrum follow the Planck distribution, that depends on the radiation temperature T (Kondratyev, 1969a):

$$E_\lambda(T) = \frac{2hc^2}{\lambda^5} \frac{1}{e^{hc/\lambda k_B T} - 1} \quad (2.4)$$

Stefan-Boltzmann
law

where h is the Planck constant, c is the speed of light in vacuum, λ is wavelength and k_B is the Boltzmann constant. Integration of Eq. (2.4) over all wavelengths from 0 to ∞ gives the Stefan-Boltzmann law for the radiant flux of a perfectly “black” surface:

$$B(T) = \frac{2\pi^5 k_B^4}{15c^2 h^3} T^4 = \sigma T^4 \quad (2.5)$$

where σ is the Stefan Boltzmann constant. The term “black” denotes that the body absorbs and emits all energy that it receives and constitutes an ideal case. According to Eq. (2.5) the radiation flux depends on the temperature of emitting surface and not on its material.

Stellar black body
radiation examples

On the basis of temperature, the region of Electro-Magnetic (EM) radiation spectrum where the magma ocean emits is compared to other instances in the solar system and beyond (Figure 2.3). This helps introduce the concepts of: radiation temperature, radiation spectrum, absorption, emission, grey absorption, line-by-line absorption and runaway greenhouse state, which are useful in the MO modeling context.

No overlap between
incoming and
outgoing energy in
modern Earth

Let us firstly examine the radiation in the case of modern Earth. The emission spectrum from the solar photosphere corresponds to a radiation temperature of 5772 K, while the Earth surface emits at an average temperature of 288 K (Ingersoll, 2013). The two spectra demonstrate minimal overlap in the range of EM frequencies (Fig. 2.3.A). On the one hand, the solar wavelength of maximum intensity is located at $\sim 0.5\mu\text{m}$ which corresponds to the visible (Vis) range (short-wave). On the other hand, the maximum emission of Earth’s surface occurs at $\sim 10\mu\text{m}$ which corresponds to the infra-red (IR) region (long-wave). The phenomenon of negligible overlap between

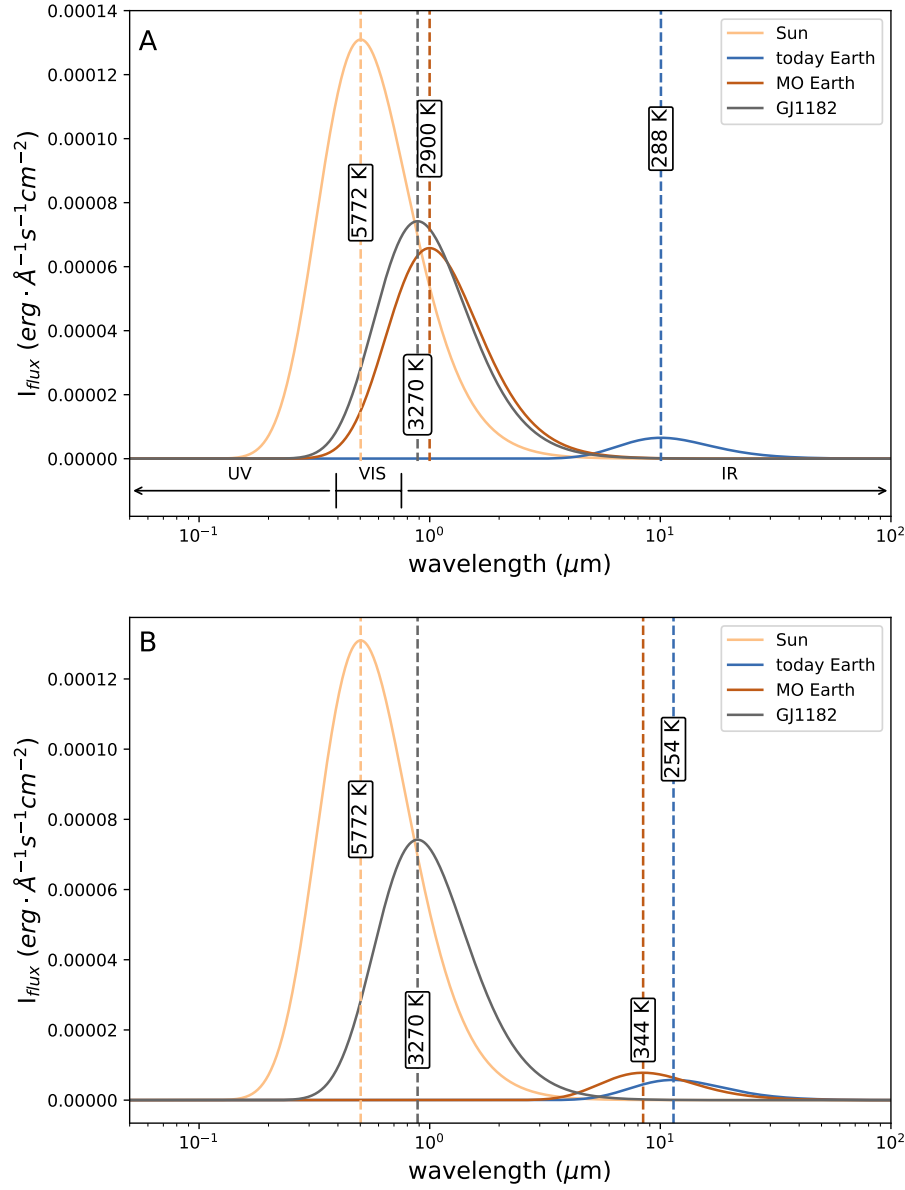


Figure 2.3: Wavelength dependent radiation flux for BB bodies with different effective temperatures A: at surface; B: at outermost radiating layer.

incoming and outgoing radiation is used in the “two-stream” modeling approximation (Pierrehumbert, 2010; Ingersoll, 2013). This effect has guided the planetary radiative energy balance formulation in the

study of modern Earth climatology. It is used to justify that all non-reflected shortwave energy from the Sun is absorbed at the planetary surface and there is no upward radiation generated from the solar energy input (neglecting the scattering effect). This greatly simplifies the associated Schwarzschild radiation equations that describe the upward and downward radiation contributions along the atmospheric profile (Kondratyev, 1969b; Pierrehumbert, 2010).

*Enters atmospheric
radiative
contribution*

The continuously absorbed solar energy transforms into thermal energy and maintains the surface temperature at which the Earth emits back toward space. The overlying atmosphere plays a vital role in this energy balance, modifying it due to the radiation absorbing gas species it contains. These compounds absorb part of the upward surface IR radiation and re-emit it, adding a secondary energy source toward the Earth surface. As a result, the surface temperature is higher than the equilibrium temperature of 255 K, which is expected based on the two-stream planetary energy balance for a black body BB that receives solar energy flux at 1 AU orbital distance. This is known as the “greenhouse effect”. In the magma ocean literature this is also referred to as atmospheric “thermal blanketing” (Abe et al., 1988; Hamano et al., 2013; Lebrun et al., 2013; Salvador et al., 2017; Massol et al., 2016; Ikoma et al., 2018).

*Radiation absorbers
in the atmosphere*

The radiation absorption and emission in the atmosphere typically depends on the frequencies at which the gas molecules vibrate. The geometry of their atomic bonds defines the vibrational/rotational frequencies at which the energy is absorbed and emitted in the form of photons. Under certain conditions, e.g. due to collisions between molecules, they absorb in additional frequencies (Wordsworth et al., 2013a). Despite the existence of multiple gas species with interesting absorption properties, only two gas species are discussed below for the purpose of this section. These are water and carbon dioxide.

H₂O absorption

Water is of paramount importance for IR absorption (Kondratyev, 1969b). Its main bands are located around wavelengths 6.3 μm and 12 μm and they are found near the maximum of outgoing Earth emission. The region 8–11 μm where water vapor does not absorb is called the “atmospheric window”. Water has additional absorption bands in the ultra-violet (UV).

CO₂ absorption

Among the multiple absorption bands of carbon dioxide, the 9.4 μm and 10.4 μm features are crucial because they are located within the atmospheric window that is nested in the IR spectral region, despite the fact that they are characterised as weak (Kondratyev, 1969a). The band centered around 15 μm is also vital as it absorbs in the far IR region (Plass, 1956; Kondratyev, 1969b).

It is evident that both H₂O and CO₂ gas species are important for modern climate because they absorb in the region of outgoing surface radiation flux (Fig. 2.3.A). The CO₂ thermal blanketing effect is

additional to that of water because they generally absorb in different wavelength bands.

Due to such absorbers the idealized black body (BB) spectrum intensity that is plotted in Figure 2.3 is never retrieved from a real emission source. Instead, it is indented at various wavelengths by the absorption effects of the species that interfere between source and observer. Increasing the spectrum analysis resolution to capture the absorption at each separate wavelength would generate a set of monochromatic radiation emission/absorption lines. The examination of radiative transfer at this level of detail is called “line-by-line” lbl and yields wavelength-dependent absorption and transmission of the source radiation. It is a computationally expensive calculation.

Realistic emission spectrum

An alternative treatment to the lbl calculation of atmospheric radiative transfer is the simpler, grey approximation. There, the ratio of absorbed to incident radiation for each species is represented with a single absorption coefficient for the full spectrum. That intermediate complexity representation captures the contribution of greenhouse phenomenon in the energy balance (Pierrehumbert, 2010), after being calibrated to reproduce the modern near surface average temperature. The single representative absorptivity value for each component is calculated studying both responses of climate simulation in 3D General Circulation/Climate Models (GCMs) (Pujol et al., 2003) and observed atmospheric profiles (Yamamoto et al., 1952). The atmospheric layer as a grey body is characterized by a relative emissivity defined as the ratio of radiant intensity at temperature T to that of a BB at the same temperature (Kondratyev, 1969a). Emissivity for grey ranges within 0–0.99, while 1 corresponds to the ideal BB and is not obtained in real conditions.

grey absorption

The radiation spectrum from the BB approximation, despite the missing representation of absorption, still provides reliable information on the radiation temperature of emission source and the spectral range which it occupies. Observing the radiation spectra in Figure 2.3.A helps clarify the absorption role of H₂O and CO₂. The surface temperature of the MO is higher than the silicate melting point, which ranges from 900 to 1500 K for rhyolite to perovskite compositions, respectively. (Parfitt et al., 2008). For a global MO it is equal to or exceeds 2900 K. In terms of radiation temperature it is comparable to that of an M-dwarf star, that occupies the Vis range of the spectrum (Figure 2.3.B). In that context, the H₂O molecule is still a significant absorber as it has additional absorption bands within the short wave emission spectrum. However, there are no CO₂ absorption bands within this range. The transfer of radiative concepts from Earth climate studies across planetary science needs to be revisited for application to the magma ocean, especially since the two stream approximation is likely insufficient. Adjustments to the available modeling tools are performed to address this issue. During the MO stage whose radia-

Comparison of regions of absorption and regions of emission

tion peaks near the visible spectrum, the role of far infra-red (IR) CO₂ is therefore degraded compared to its role in modern Earth climate. CO₂ is here represented with a lower radiation absorption coefficient in the grey approximation.

2.1.6 *Runaway greenhouse atmospheric state*

Under excessive radiative forcing, the planetary energy balance may not be met by the atmospheric radiative response. Such forcing conditions can be the increased atmospheric content in IR absorbers and the elevated shortwave radiation level from the host star. If the downward radiative emission of the atmosphere increases the surface warms and responds by emitting at higher radiation temperatures with additional IR intensity. The surface water reservoir evaporates into the atmosphere and can cause saturation with respect to water vapor. At saturation the Outgoing Longwave Radiation (OLR) reaches a limiting rate value with which the planet disposes of heat. The top of the atmosphere (TOA) becomes opaque to the surface radiation (Pierrehumbert, 2010; Goldblatt et al., 2013; Leconte et al., 2013; Yang et al., 2016; Gómez-Leal et al., 2018). At even higher insolation, the surface responds by raising its temperature, but the atmosphere cannot surpass a certain limit of cooling rate. This qualitative state of the planet is referred to as the “runaway greenhouse state” (RG). The constant rate at which the outer layer radiates toward space is called “Simpson-Nakajima” (Hamano et al., 2013; Goldblatt et al., 2013) or “Kombayashi-Ingersoll” (KI) (Pierrehumbert, 2010) or just runaway greenhouse limiting radiation. The exact value of this limit is a subject of debate and depends on the modeling approach employed for its calculation (Yang et al., 2016).

It is possible that a water-rich atmosphere over the magma ocean will reach saturation (Hamano et al., 2013; Ikoma et al., 2018). Once it reaches the limit of outgoing energy it will become opaque to any radiation from the surface and it will emit at the effective temperature of the atmospheric outermost layer. The emissivity of the vapor-saturated atmosphere at the TOA layer reaches 0.99 and has an effective temperature of 344 K at the RG onset, according to a recent study by Gómez-Leal et al. (2018). As seen in Figure 2.3.B, the radiant intensity of the water vapor saturated TOA is comparable in order of magnitude to that of the TOA in today’s moderate climate. Note a crucial qualitative difference between the two Earth-cases. During the magma ocean phase, the heat release at the surface is that which drives the surface-atmosphere energy balance. On the contrary, the studies that focus on runaway greenhouse onset assume T, P initial conditions (IC) of a moderate Earth climate and the radiative balance there is modified either by the forcing of CO₂ doubling (Leconte et al., 2013; Gómez-Leal et al., 2018) or by an increase in received solar ra-

diation (Kasting, 1988; Goldblatt et al., 2013; Gómez-Leal et al., 2018). Since the causation of the runaway greenhouse is different in each case, the conclusions should be extrapolated with caution.

2.1.7 *Magma ocean types*

Various categorizations have been attempted for the magma ocean, using as distinctive feature either the MO causation or its thermal evolution response. Regarding the thermal evolution response, Hamano et al. (2013) introduced a separation of the magma-ocean stage into short-term (type I) and long-term (type II). Based on the comparison of incoming stellar radiation to the KI limit of a H₂O-dominated atmosphere, Hamano et al. (2013) brought the role of stellar luminosity in the context of magma ocean thermal evolution. Under suitable conditions, they found, the solar input can hinder the planetary cooling altogether.

In this work I study the thermal evolution of the magma ocean without examining the prior stage of its formation. The magma ocean is here a stage of the planetary evolution that finishes when the magma ocean solidifies. Concerning the causation of MO, I here draw specific attention to the difference between “evolutionary” and “permanent” magma ocean which is studied in other works (e.g. Schaefer et al., 2016; Hammond et al., 2017). The cases studied in this work belong to the “evolutionary” magma oceans that are generated during and due to the planetary accretion process. Once the planet cools and the magma ocean solidifies, the equilibrium temperature at that planetary orbit is lower than the melting temperature of the mantle and the planet remains in solid state.

However, within a certain orbital distance the energy for melting the mantle is already provided by the solar irradiation alone and the atmosphere blanketing effect becomes irrelevant for melting, least it contributes with an additional warming forcing that preserves the surface in molten state. The causation of this MO is distinctly different from the evolutionary case. This is the “permanent” magma ocean and it is caused by the host star.

2.2 BRIEF NUMERICAL MODEL OVERVIEW

I introduce a numerical setting to simulate the coupled evolution of the interior and atmosphere, based on the arrangement of Lebrun et al. (2013) with replacements in specific parts. Several models from the literature were accommodated in original form or were developed to include in this work. Their combined implementation into the fortran 95 CONvective Magma Radiative Atmosphere and Degassing model will be hereafter referred to as “COMRAD model”. The following models from the literature were implemented in the code: the Abe et al. (1985) model for the grey atmosphere of H₂O and CO₂, the Giordano et al. (2008) model for calculating the silicate melt viscosity as a function of water and temperature, and the mantle surface temperature iteration method developed by Lebrun et al. (2013) that satisfies the energy balance. I adapted this idea to own numerical implementation.

Apart from the grey, a second model for the atmosphere was developed in collaboration with Katyal et al. (2019) and is described in detail in the respective work. This model makes use of the Generic Atmospheric Radiation Line-by-line Infrared Code (GARLIC) code by Schreier et al. (2014) as well as the external High-resolution TRANsmission molecular absorption database (HITRAN) by Rothman et al. (2013). To enable that model coupling with the interior, I implemented a bilinear interpolation scheme of pre-calculated outgoing radiation values on a 2D grid of pressure and temperature at the surface.

In overview, the COMRAD model resolves the mantle interior profiles of temperature and the liquid and solid fraction, along with the degassing process, initiated from a fully molten mantle up to the end of the magma ocean phase (see Section 2.7). The outgassing of H₂O and CO₂ is calculated according to a melt solubility curve for each volatile that ignores their chemical interaction (Section 2.5). The atmosphere is treated in two alternative ways (Section 2.6): i) As a grey atmosphere accounting for two greenhouse gas species H₂O and CO₂ (Abe et al., 1985; Elkins-Tanton, 2008) and ii) as a pure H₂O atmosphere with a line-by-line (lbl) radiative transfer representation. Its integrated transmission provides Outgoing Longwave Radiation at the Top Of the Atmosphere, henceforth named “OLR at TOA” (OLR_{TOA}).

In the remaining section I will separately introduce each model component.

2.3 STRUCTURE OF THE INTERIOR

A spherically symmetric Earth with outer radius R_p and core radius R_b is considered. This yields a mantle of thickness $R_p - R_b$ whose physical properties are defined by the solidus and liquidus melting curves of KLB-1 peridotite. By comparing the interior thermal pro-

*Thinking in
spherical shells*

file to these curves (Fig. 2.4), I identify the phase of matter (liquid, partially molten, or solid) at each mantle layer.

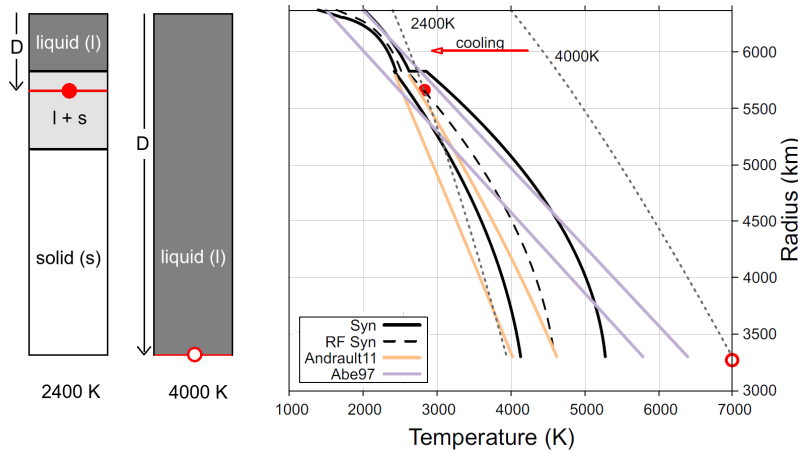


Figure 2.4: Figure from Nikolaou et al. (2019) © AAS. Reproduced with permission. **Right:** Melting curves for three cases: linear according to Abe (1997) (“Abe97”, purple solid lines); synthetic for peridotitic composition according to Herzberg et al. (2000), Hirschmann (2000) and J. Zhang et al. (1994) for the upper mantle, and Fiquet et al. (2010) for the lower mantle (“Syn”, black solid lines); for chondritic composition according to the same data for the upper mantle and Andrault et al. (2011) for the lower mantle (“Andrault11”, yellow solid lines). “Syn” and “Andrault11” differ only in the lower mantle parametrization. Black dashed lines indicate the profile of the rheology transition for the “Syn” curves (“RF Syn”). Dotted lines indicate adiabats with potential temperatures of 4000 K and 2400 K. The red open and full circles indicate the base of the liquid-like magma ocean of thickness D for the two adiabats. **Left:** Depth ranges of liquid (l), solid (s), and partially molten (l+s) regions corresponding to the 2400 K and 4000 K adiabat representation on the right.

The mantle is assumed to be initially fully molten and convecting (global magma ocean), with an adiabatic temperature profile. As it cools, the liquid adiabat intersects with the melting curves (solid lines in Fig. 2.4). Due to the steeper slope of the adiabat compared to the melting curves of primitive mantle, they intersect first atop the CMB and initiate crystallization from the bottom up.

Therefore, at any snapshot in the system’s evolution the mantle is divided at most into three different layers. It is fully molten from the surface until the depth of intersection between adiabat and liquidus; it is partially molten between liquidus and solidus, and completely solid below the solidus (Fig. 2.4). The level of 40% volume melt fraction in the partially molten region separates the solid-like from the liquid-like regime in this study. The 40% interface that separates the two regimes is called “solidification front” or “rheology front” (RF) (solid red circle Fig. 2.4).

2.3.1 Melting curves

*A static
representation of the
mantle composition.*

The melting curves definition is indispensable to the melt fraction calculation.

I use solidus and liquidus curves of KLB-1 peridotite obtained from experimental data. Depending on pressure, I adopt three different parameterizations for various parts in the mantle. For the solidus, I use data from Hirschmann (2000) for $P \in [0, 2.7)$ GPa, Herzberg et al. (2000) for $P \in [2.7, 22.5)$ GPa, and Fiquet et al. (2010) for $P \geq 22.5$ GPa, while for the liquidus, from J. Zhang et al. (1994) for $P \in [0, 22.5)$ GPa, and Fiquet et al. (2010) for $P \geq 22.5$ GPa. Since I here employ data from multiple studies, I refer to the resulting set of melting curves as “synthetic”. Such curves are adopted in the experiments unless otherwise specified.

As shown in Fig. 2.4, I also test the linear melting curves adopted by Abe (1997) and later by Lebrun et al. (2013), as well as those introduced by Andrault et al. (2011) that are representative of a chondritic composition. Expressions fitted to experimental data for all the melting curves employed are given below 2.3.1.1–2.3.1.3:

2.3.1.1 “Synthetic” melting curves

For the solidus temperature (T_{sol}) of nominally anhydrous peridotite and pressures $0 \leq P \leq 2.7$ GPa, I use (Hirschmann, 2000) :

$$T_{sol} = 1120.661 + 273.15 + 132.899P - 5.904P^2, \quad (2.6)$$

with reported uncertainty by the authors of ± 20 K. For $2.7 < P \leq 22.5$ (Herzberg et al., 2000):

$$T_{sol} = 1086 + 273.15 - 5.7P + 390 \log(P), \quad (2.7)$$

with reported uncertainty by the authors of ± 68 K. At higher mantle pressures, for $P > 22.5$ GPa, I use a quadratic fit to the data of Fiquet et al. (2010) for fertile peridotite:

$$T_{sol} = 1762.722 + 31.595P - 0.102P^2. \quad (2.8)$$

For the liquidus of fertile peridotite, I use a fit to data of J. Zhang et al. (1994) for $0 \leq P \leq 22.5$ GPa:

$$T_{liq} = 2014.497 + 37.743P - 0.472P^2, \quad (2.9)$$

and for $22.5 > P$ GPa, again a quadratic fitting to data of Fiquet et al. (2010):

$$T_{liq} = 1803.547 + 50.810P - 0.185P^2. \quad (2.10)$$

2.3.1.2 Linear melting curves

A linear approximation for the melting curves presented in Abe (1997) is used for both solidus and liquidus:

$$T_{sol} = 1500.0 + \frac{4450.0}{3000.0}z, \quad (2.11)$$

and

$$T_{liq} = 2000.0 + \frac{4560.0}{3000.0}z, \quad (2.12)$$

where z is the depth from the surface in km.

2.3.1.3 Andrault melting curves

The following quadratic fitting to the data of Andrault et al. (2011) for a chondritic composition covers the lower mantle for $P > 22.5$ GPa:

$$T_{sol} = 2056.489 + 15.801P - 0.003P^2, \quad (2.13)$$

and

$$T_{liq} = 2049.555 + 24.671P - 0.035P^2. \quad (2.14)$$

Melting curves for the upper mantle are identical to those described above as “synthetic”, unless otherwise specified.

2.3.1.4 Constant melting curves

I above assumed a set of KLB-1 melting curves that belong to the oxidizing end. The melting curves remain constant throughout the simulation. This may not be the case during MO chemical evolution.

The liquidus' and solidus' shapes vary greatly at pressures greater than 3 GPa. Above that pressure level and depending on water content different phases exchange in stability (Katz et al., 2003). Hydrated and oxidized $\text{H}_2\text{O} + \text{CO}_2$ peridotite has the lower solidus at depth while reduced mantle increases the solidus by 50–200 K (Foley et al., 2018). The in-between region produces so called incipient melts. At 6 GPa, a relatively shallow depth with respect to the Earth's mantle extent, the melting curve converges to the oxidized solidus curve (Foley et al. (2018) Fig 1.3). Recent studies (H. L. Zhang et al., 2017) suggest that pressure effects cause the oxidation state to vary throughout the deep mantle, specifically by 2.5 log units in oxygen fugacity. Moreover, the liquidus position is uncertain due to supercriticality observed in the hydrous silicate mineral phases mixture (Kono et al., 2015; Makhlof et al., 2017). In the presence of water, the liquidus position is disputed in pressures as low as 3 GPa because of varying interpretation of the quenched glass products (Manning, 2018).

On the one hand, the initially reduced state of the mantle could increase the solidus temperature. On the other hand the water content

of the enriched mantle could decrease the solidus until the minimum that is defined at water saturation. With respect to these counteracting processes, both of which are ignored in this study, the assumption of constant solidus and liquidus is sufficient as a first order approximation.

2.3.2 Melt estimation

*Simple
representation of a
complex
physical-chemical
process.*

The volumetric melt fraction or melt degree ϕ is calculated by the following linear expression (e.g. Solomatov et al., 1993b,a; Abe, 1997; Solomatov, 2007; Lebrun et al., 2013):

$$\phi_z = \frac{T_z - T_{sol,z}}{T_{liq,z} - T_{sol,z}} \quad (2.15)$$

where T_z is the temperature of the mantle at depth z , and $T_{sol,z}$ and $T_{liq,z}$ the corresponding solidus and liquidus temperatures. Therefore, ϕ_z is nothing but the relative position of T with respect to the melting curves at a given depth.

The partially molten region is qualitatively divided into two regions by comparison of the melt fraction with the “critical melt fraction” $\phi_C = 40\% = \text{const.}$ The ϕ_C distinguishes liquid-like from solid-like behavior (Costa et al., 2009). For $\phi > \phi_C$, the region is considered liquid-like and therefore is part of the convecting magma ocean. That domain has depth D (Fig. 2.4).

Note that ϕ_C varies in the geodynamic literature among 30% (e.g. Maurice et al., 2017; Hier-Majumder et al., 2017), 40% (Solomatov, 2007; Bower et al., 2018) and 50% (Monteux et al., 2016; Ballmer et al., 2017).

The linear calculation of the melt fraction Eq. (2.15) is a simplification. In any P,T phase diagram of a pure molecular species a unique curve that separates liquid from solid phase would be expected. However, the two melting curves (P,T) of the mantle do not coincide. They are separated by a range of pressures/temperatures where the mantle is part liquid and part solid. “The existence itself of such a region is proof of the non-linear melting process of the mantle” (S. Solomatov, pers. comm.)

A mineral phase chemical equilibrium modeling is outside of the scope of this study. The choice of melting curves, however, implies a choice of composition. I will be considering the melt of this system to be primitive, that is defined as follows: It may have been modified since extraction from its source mineral and is not in chemical balance with its parent rock (Foley et al., 2018). The source is assumed to be peridotite KLB-1 which is a historically common approach in mineralogy (Foley et al., 2018).

2.3.3 *Adiabat*

The temperature profile is assumed to be adiabatic throughout both the liquid and solid regions of the mantle, which, besides convection in the magma ocean, also implies sub-solidus convection in the solid mantle beneath the MO. Indeed Maurice et al. (2017) and Ballmer et al. (2017) showed that solid state convection can fully develop already during the magma ocean stage, particularly in the presence of a blanketing atmosphere that delays the solidification.

Convection throughout the mantle

The interior temperature profile is calculated using the expression of the adiabatic temperature gradient for a one-phase system:

$$\frac{dT}{dP} = \frac{\alpha_T T}{\rho c_P}, \quad (2.16)$$

where P is the pressure in GPa, c_P the thermal capacity at constant pressure, and α_T the pressure-dependent thermal expansivity given by (Abe, 1997):

$$\alpha_T(P) = \alpha_0 \left[\frac{PK'}{K_0} + 1 \right]^{-(m-1+K')/K'}, \quad (2.17)$$

where α_0 is the surface expansivity, K_0 the surface bulk modulus and K' its pressure derivative (see Table 2.3 for their values), and $m = 0$. The pressure is simply calculated assuming a hydrostatic profile.

It is worth noting that Solomatov et al. (1993b,a) derived the adiabat for a two-phase system by introducing thermal expansivity and thermal capacity as functions of melt fraction for the partially molten region. However, the expressions derived are explicitly valid for a system with constant rate of temperature drop with depth, which is equivalent to constant phase boundary slope and thus applies only to linear melting curves such as those of Abe (1997). The modified adiabat then tends to align with the slope of constant melt fraction. Since they do not cover the higher order parameterizations of the experimental data that I adopted, I instead employ the one phase adiabat of Eq. (2.17) with constant thermal capacity and pressure-dependent thermal expansivity.

2.3.4 *Viscosity*

2.3.4.1 *Viscosity of the melt*

The typical value for viscosity of polymerized silicate melts is 1 Pa s at normal conditions ($P=1$ bar) (Manning, 2018). The viscosity is affected by the water content, which in turn is defined by its solubility in the silicate at vapor saturation. Kono (2018) cites 10^{-3} Pa s as the minimum value of the silicate melts encountered at sulfur melting experiments at 3.8 GPa and 1703 K. Solomatov (2007) also gives 10^{-2}

Harmonic average along the MO profile.

Poise ($= 10^{-3}$ Pa s) for melt viscosity which is the lowest value I used. He suggests that at $T > T_{liq}$, in the presence of water, the viscosities and thermal diffusivities of water and completely polymerized silicates are similar (Persikov et al., 1990). Therefore the viscosities are not expected to differ much between completely depolymerized hydrous magma and anhydrous magma (Solomatov, 2007).

On the contrary the role of water for melts generated near the solidus temperatures is crucial. The H_2O depolymerizes the mineral structure for pressures greater than 3 GPa (Manning, 2018). At low pressures < 3 GPa the mineral remains water-saturated due to the stability of pargasitic amphibole (Green et al., 2010). At water content higher than 20% H_2O remains molecular and there is no additional effect on the viscosity even if the concentration further increases (Manning, 2018).

In the region of partial melt, the viscosity η is defined by the two-phase flow. The Einstein (1906) formula for diluted suspensions describes the viscosity of partial melts where melts and crystals coexist. Roscoe (1952) reformulated the relation for the case of silicate melts:

$$\eta = \eta_l(1 + 2.5\phi) \quad (2.18)$$

where η_l is the viscosity of the melt without crystals and ϕ is the melt fraction.

The effect of pressure on viscosity is not monotonic with depth due to changes in structure above and below the depth of 5 GPa (Sakamaki et al., 2013). For peridotitic melts at $P > 5$ GPa the viscosity increase with depth is slight. Karki et al. (2010) suggest an overall variation of one order of magnitude along the Earth mantle depth.

Experiments defining viscosity have been performed for pressure conditions $P < 7$ GPa (Fig. 10.5 in Kono et al. (2014)). The limitation to measuring viscosity is defined by the frame-rate of the X-ray camera which can capture until 0.0003 Pa s (Kono, 2018). More advances are required to capture the metallic tracer's motion within lower viscosity melts.

The melt viscosity is one of the main factors that set the time scale for the cooling and solidification of the magma ocean (Eq. 2.25). Hence it is important for the system's thermal evolution (Eq. 2.28).

The transition between the two mantle regimes, namely liquid-like and solid-like, is a complex phenomenon that depends, among other factors, on composition and cooling rate (Speedy, 2003). While the viscosity dependence on temperature follows an Arrhenius law below the solidus temperature (Kobayashi et al., 2000), non-linear effects take place near and above it (Dingwell, 1996; Kobayashi et al., 2000; Speedy, 2003). The solidification into a crystal structure differs from the solidification into a glassy amorphous state. Silicate liquids that contain a certain percentage of crystals retain a liquid-like character as long as that is lower than a critical value. With increasing crystal

content during cooling, the rheology is expected to make a discontinuous jump from the liquid- to solid-like state over a short crystallinity range (Marsh, 1981). On the contrary, for glasses continuous variations in viscosity across five orders of magnitude are expected (Kobayashi et al., 2000). Above the glass temperature the theory is still debated related to the Kauzmann paradox of entropy (Speedy, 2003). The Vogel-Fulcher-Tammann (VFT) equation is employed in our work for calculating the water dependent viscosity above the glass temperature.

Recently, Salvador et al. (2017) proposed a “smoothing” of the sharp viscosity jump occurring at the liquid-like to solid-like change, in order to mitigate the transition into solid state found during magma ocean numerical simulations such as Lebrun et al. (e.g. 2013). However, since such discontinuous behavior is actually observed in fractional solidification experiments (Marsh, 1981; Speedy, 2003), I based our description of the viscosity on an abrupt transition that occurs at the critical melt fraction ϕ_C .

Below I explain the viscosity employed during the MO lifetime, which is the liquid-like viscosity (η_l). Note here that the solid-like viscosity (η_s) is employed only after the MO phase ends.

The viscosity of the melt without considering the presence of crystals (η_l), is calculated assuming a VFT expression as also used in Giordano et al. (2003) and Karki et al. (2010). It has the following generic form:

$$\eta_l(T) = A \exp \left[\frac{B}{T - C} \right], \quad (2.19)$$

where A , B , C are constants, and T is the temperature.

The VFT expression is employed for fluids that deviate from the Arrhenius-like description of the viscosity for which viscous flow is a strictly thermally-activated process. In the VFT case, the viscosity additionally tends to an infinite (hence not physically meaningful) value for a threshold temperature $T = C$. I consider two such expressions for the dynamic viscosity: one that depends on the temperature only $\eta_l = f(T)$ (Karki et al., 2010) and a second one that depends on both temperature and water content $\eta_l = f(T, X_{H_2O})$ (Giordano et al., 2008).

Karki et al. (2010) studied the effects of pressure and temperature throughout the Earth’s mantle for a nominally anhydrous (0% water) and a hydrous (10 wt% water) composition using ab initio calculations. They found that for hydrous melts, the viscosity at a given potential temperature can be well fitted with Eq. (2.19) with constants $A = A_K$, $B = B_K$ and $C = C_K$:

$$\eta_l(T) = A_K \exp \left[\frac{B_K}{T - C_K} \right], \quad (2.20)$$

where A_K , B_K , C_K are calculated for a fixed water content of 10 wt% (See Table 2.3 for their values).

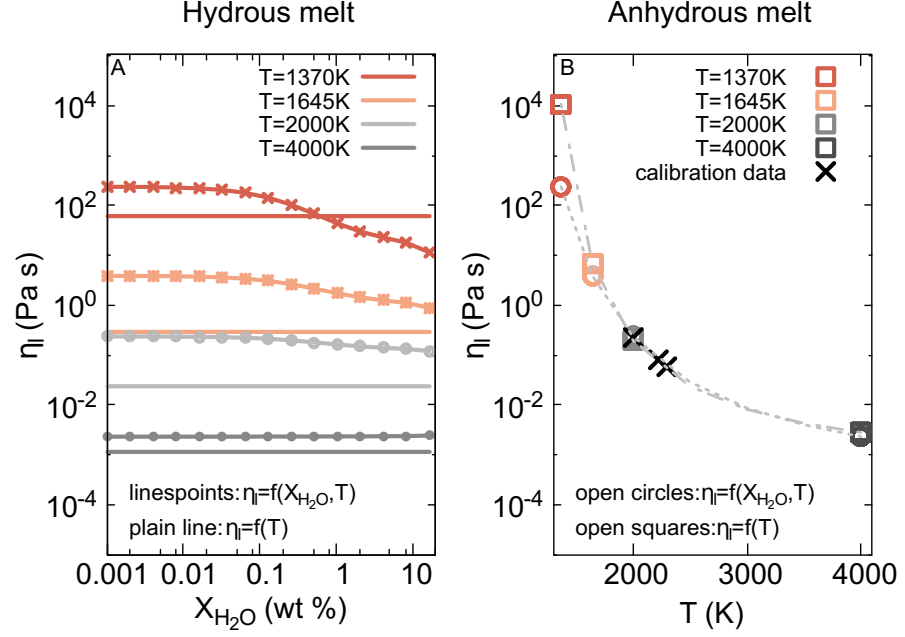


Figure 2.5: Variation of melt dynamic viscosity η_l with temperature for hydrous and anhydrous melt. **A:** Melt viscosity as a function of water content for different temperatures. Equation (2.20), which assumes a fixed water concentration of 10 wt% (solid lines), while Eq. (2.21) explicitly includes the effect of water concentration (linepoints). **B:** Viscosity of anhydrous melt as a function of temperature. Squares and circles are obtained with Eq. (2.20) and Eq. (2.21) with $X_{H_2O} = 0$, respectively. Experimental values of anhydrous peridotitic melt are obtained from Urbain et al. (1982) (see Section 2.3.4.2).

However, approach (2.20) does not explicitly include the effect on the magma ocean viscosity of the water content, which is expected to vary during the simulations (see Section 3.2). The presence of water tends to lower the melt viscosity (Marsh, 1981; Dingwell, 1996; Giordano et al., 2008; Karki et al., 2010). Therefore it is important to include it as a time-dependent variable in our model.

In order to study this effect, I implemented the empirical model of Giordano et al. (2008), which takes into consideration the water concentration, together with the concentration of 13 different oxides in the silicate melt. It calculates two of the three parameters of the VFT equation (2.19) (B_G and C_G in Eq. (2.21) below). The viscosity for a given temperature T and water concentration X_{H_2O} is given by:

$$\eta_l(T, X_{H_2O}) = 10^{A_G} \log_{10} \left[\frac{B_G}{T - C_G} \right] \quad (2.21)$$

where the parameter $A_G = -4.55 \pm 1$ is a constant pre-exponential factor. The parameters $B_G(X_{H_2O})$ and $C_G(X_{H_2O})$ are not constant and are calculated by the model at each time step according to the evolving concentration of water (see Sect. 2.5). Even though our model is unable to resolve the evolution of melt composition, it does resolve the evolution of the water content with time, which allows us to use the model of Giordano et al. (2008) with a new input of the water content at each time step.

In order to use this model, it is required that a suitable composition is chosen as a constant, non-evolving basis. To be consistent with the assumption of a peridotitic composition, it is important to use a composition as close to a primitive one as possible. Indeed the composition of basanite is among the least evolved in the classification of melts (Le Bas et al., 1986). I found that the composition of basanite (Giordano et al., 2003, 2008) is able to reproduce the experimental values for the temperature dependent viscosity for the anhydrous case (Urbain et al., 1982) after calibration of the prefactor A_G (see Section 2.3.4.2. This fitting provides us with a parameterized description of the composition that allows us to treat the decrease in melt viscosity with increasing water content (Fig. 2.5A).

In contrast to Eq. (2.21), the parametrization of Karki et al. (2010) yields a viscosity that is independent of the explicit water content (Eq. 2.20). For anhydrous melt, the viscosity calculated with Eq. (2.21) and $X_{H_2O} = 0$ yields similar values as those proposed by Karki et al. (2010) according to Eq. (2.19) at high temperatures, though the two tend to depart significantly for temperatures near the solidus (Fig. 2.5B). The competition between the effects of temperature and water content on the resulting viscosity shows that while the temperature dependence plays a decisive role at high temperatures, at low temperatures ($T < 1645$ K) the viscosity varies by up to two orders of magnitude over the range of water concentrations examined. Therefore, the effect of water becomes dominant at lower temperatures where the solidification is expected (Fig. 2.5A).

The pressure dependence of the viscosity for the hydrous case is not explicitly provided by Karki et al. (2010). The authors report that it varies by a relatively small factor between 2.5 and 10 over the pressure range [0, 140] GPa spanned by a global terrestrial magma ocean. In the following, for simplicity, I will neglect such dependence and use the liquid viscosity evaluated at the potential temperature T_p of the magma ocean as representative for the fully molten part.

The melt viscosity η_l is further corrected for the crystal fraction content in each layer before it is employed for the calculation of the average viscosity of the magma ocean. In the liquid-like partially molten

region, the effect of crystals is taken into account with the Roscoe (1952) expression reformulated by Lebrun et al. (2013) as follows:

$$\eta = \frac{\eta_l}{\left(1 - \frac{1-\phi}{1-\phi_c}\right)^{2.5}} \quad (2.22)$$

and this version is employed in the COMRAD model.

By combining equations (2.20) or (2.21) with (2.22) for each layer that belongs to the magma ocean, I obtain the volumetric harmonic mean viscosity η that is then used in the calculation of parametrized convective heat flux in Eq. (2.25). The effect of the layer with the lowest viscosity value is prioritized in the calculation of harmonic mean viscosity. This sets the leading order of magnitude for the η_l value that is then used in the Ra calculation (2.1).

2.3.4.2 Calibration of the melt viscosity prefactor

The composition of anhydrous peridotite, which I employed to define our “synthetic” melting curves (a list of the corresponding oxides can be found in Hirschmann (2000)), is not covered by the empirical model of Giordano et al. (2008) that I used to determine the liquid viscosity and its dependence on the water concentration (2.3.4). However, I found that the composition of basanite, that belonged to the Giordano et al. (2003, 2008) model calibration database, is able to reproduce the temperature-dependent viscosity values of anhydrous peridotite obtained experimentally (Urbain et al., 1982).

Assuming such composition and fitting the model of Giordano et al. (2008) to the experimental data of Urbain et al. (1982) (see Fig. 2.5), I obtained a modified prefactor in Eq. (2.21), namely $A_G = -3.976$. The result is within the acceptable range of $A_G = -4.55 \pm 1$ log unit, given by the model authors (Giordano et al., 2008). As shown in Table 2.1, the use of this prefactor yields an error relative to the experimental values that lies within $\pm 10\%$. That error is comparable to the uncertainty in laboratory experiments (Kono, 2018).

Note that I use this calculation only to provide a first-order estimate of the water effect on the melt viscosity, without needing to explicitly describe the evolution of melt composition. The latter aspect is beyond the scope of the present work.

2.3.4.3 Solid-like viscosity η_s

The solid-like dynamic viscosity η_s is employed only when the rheology front reaches the surface. By model construction it is only employed after the MO phase ends. I calculate η_s according to the Arrhenius law for diffusion creep as formulated by Karato et al. (1993):

$$\eta_s = \eta_0 \exp\left(\frac{E + PV}{RT}\right) \quad (2.23)$$

Table 2.1: Comparison between values of the viscosity of anhydrous liquid peridotite obtained experimentally and calculated with the model of Giordano et al. (2008) assuming a basanite composition and a prefactor $A_G = -3.976$ in Eq. (2.21).

T (K)	Experimental η_l (Pa s)	Calculated η_l (Pa s)	Error (%)
2000	0.22	0.2350	6.84
2220	0.08	0.0788	-1.47
2300	0.06	0.0579	-5.01

η_0 is a pre-exponential factor, E the activation energy, V the activation volume, and R the gas constant (see Table 2.3 for the values of these parameters).

The viscosity of the partially molten solid-like region below the rheology front (i.e. for $\phi < \phi_C$) is modified by the presence of crystals according to the expression (Solomatov, 2007):

$$\eta = \eta_s \exp(-26\phi), \quad (2.24)$$

where η_s is the dynamic viscosity obtained from Eq. (2.23).

2.3.5 The three convecting layers

The modeled system is composed of three layers of geophysical fluids that all convect and dispose of heat at their upper boundaries. Those layers, represented as spherical shells in our 1D model, are: the liquid mantle (MO), the solid mantle, and the lower part of the atmosphere. Each of them is at different pressure, temperature conditions and state of matter and convects at differing time scales.

2.3.5.1 Liquid mantle (MO) convection

In the MO, $\eta \approx 10^{-3}$ Pa s for $T_p \approx 4000$ K at surface pressure. Evaluating the parameters into Ra and Pr for a magma ocean that fully extends to the mantle thickness results in $Ra \approx 10^{30}$ and $Pr \approx 1$.

The high Ra value predicts that the buoyancy force is much higher than the viscous friction, and ensures convective instability for critical Rayleigh number $Ra_C \approx 1700$ (Zahnle et al., 1988). In a fluid with such relatively low dynamic viscosity $\eta \approx 10^{-3}$ Pa·s, the instability is expected to develop within short time interval, even when assuming a low temperature difference imposed at the surface.

The MO convective heat flux F is described as a function of Ra and Pr . I consider two different F parameterizations for “soft” and “hard” turbulence. The first considers that turbulence affects the heat flux

through the boundary layers, while the flow is laminar in the bulk of the fluid (Siggia, 1994; Solomatov, 2007):

$$F_{\text{soft}} = 0.089 \frac{k_T (T_p - T_{\text{surf}}) Ra^{1/3}}{D} \quad (2.25)$$

where $k_T = \kappa_T \rho c_p$ is the thermal conductivity. Constants 0.089 and $1/3$ are defined by the pattern of convection. In the above formulation, the heat flux becomes independent of the convective layer depth since the Rayleigh number is proportional to D^3 . The second formulation depends additionally on the inverse Prandtl number so that increasing values of Pr in a progressively more viscous fluid yields lower F values at constant Ra regime (Solomatov, 2007):

$$F_{\text{hard}} = 0.22 \frac{k_T (T_p - T_{\text{surf}})}{D} Ra^{2/7} Pr^{-1/7} \lambda^{-3/7} \quad (2.26)$$

where $\lambda = \text{basin Length/Depth}$ is the aspect ratio of the mean flow. For very high Ra , the hard turbulence parameterization is suggested (Solomatov, 2007). This represents a regime where the heat flux is assumed to be controlled not only by boundary layer friction but also has a contribution from turbulence generated in the bulk volume of the fluid. Both parameterizations were implemented and tested, but the soft turbulence one is employed in most experiments.

Based on Solomatov (2007) the typical time scale for a MO convective overturn is:

$$\tau_{MO} = \frac{D}{u_{\text{conv}}} = \frac{L}{0.6 \left(\frac{\alpha_T g L F}{\rho c_p} \right)^{1/3}} \quad (2.27)$$

where u_{conv} is the convective velocity and D is the magma ocean depth. The typical time scale for the global magma ocean overturn during early thermal evolution is ~ 24 days ~ 3 –4 weeks.

2.3.5.2 Lower atmosphere convection

The forcing of atmospheric convection is the surface warming by absorption of the solar incoming radiation. In the MO this heat is provided directly by the mantle. The main visible feature of a convecting atmosphere is the cloud generation within the troposphere. The atmosphere demonstrates a stability against overturn. Atmospheric stability is estimated as a function of its relative humidity profile and its temperature profile. The moist air feeds into a potential energy reservoir, known as convectively available potential energy (CAPE). Upon instability, CAPE transforms into kinetic energy, precipitation and/or cloud generation in the atmosphere. The temperature profile then establishes to satisfy the convective-radiative balance.

The study of Abe et al. (1985) compared the convective-radiative temperature profile to the radiative profile and found negligible differences between the two. They thus resolved for the numerically less complex net heat flux of the radiatively balanced atmosphere and assumed it to be a sufficient representation of the heat flux through a convectively-radiatively balanced atmospheric layer. Here I adopt their approach for the grey atmosphere.

Precipitation is intermittent and needs non hydrostatic balance models in order to be resolved. Since local thermodynamic equilibrium (LTE) is assumed, precipitation events are, consequently, not resolved. The effect of clouds and vapors in the water saturated atmosphere is accounted for with the constant albedo value 0.30 after Leconte et al. (2013).

The convective time scale for the atmosphere during early thermal evolution using equation 2.27 is ~ 6 hours. Neglecting photochemistry effects, the radiative transfer process is assumed to reach balance almost instantaneously.

*Atmosphere typical
convective overturn
time scale τ_{atm} .*

2.3.5.3 Solid mantle convection

According to 3D simulations the mantle overturn is episodic. A rapid time scale of 100 yr is calculated if thermal diffusion is ignored and the overturn is treated as Rayleigh-Taylor instability at the end of the MO, despite the high mantle viscosity (Turcotte et al., 2002; Miyazaki et al., 2019b). According to Davaille et al., 2005, laboratory experiments for thermally driven convection in a fluid with temperature dependent viscosity at $Pr > 3$ and $Ra = 10^6$ predicts plume lifetimes of 10 and 200 Myr for Earth mantle viscosity 10^{19} Pa s and 10^{22} Pa s, respectively. By these arguments one cannot uniquely constrain the time required for the onset of solid-state convection.

*Solid mantle typical
convective overturn
time scale τ_S*

In this work I assumed the end member case of a solid mantle which has established convection. In particular I assume that the solid part convects from the moment of its formation, that is simultaneously to the MO evolution as well as after its end. Among the multiple values that have been given (Jaupart et al., 2011) for the $Nu-Ra$ scaling constants for the solid mantle, I here use the same constant values as in Eq. 2.25 but a different expression for the solid viscosity. This is a simplification since I assume one dynamic viscosity value, averaged across layers, to represent the solid mantle convection.

In the simulations, solid mantle's heat flux is two orders of magnitude lower than the lowest heat flux during the MO. It is expected not to have an effect on the MO thermal evolution, in the case where no crust is formed. The solid mantle is therefore neglected as a heat source at the MO bottom as long as the MO overlies it. After the MO ends, the solid mantle is the only remaining heat source to the surface and it is resolved in balance to the heat flux through the coupled atmospheric layer. The mean surface heat flow today, where convection

in the mantle is established, is 87 mW/m^2 (Turcotte et al., 2002), but it is expected to differ at end of a warm magma ocean.

2.4 ENERGY CONSERVATION

Assuming that the mantle temperature profile $T(r)$ is adiabatic, the evolution of the magma ocean is obtained by integrating the energy-balance equation (Abe, 1997) over the evolving magma ocean volume:

$$\rho \left(c_P + \Delta H \frac{d\phi}{dT} \right) \frac{dT}{dt} = - \frac{1}{r^2} \frac{\partial(r^2 F_{conv})}{\partial r} + \rho q_r, \quad (2.28)$$

where ρ is the density, ΔH the specific enthalpy difference due to phase change, F_{conv} the parameterized convective cooling flux out of the magma ocean, and q_r the internal heat released by the decay of the radioactive elements.

The heat production due to the long-lived radioactive elements ^{238}U , ^{235}U , ^{40}K and ^{232}Th , and the short-lived elements ^{26}Al and ^{60}Fe is taken into account in the energy balance equation (2.28) via the term q_r whose explicit expression reads:

$$q_r = \sum_i f_i X_i^0 Q_i \exp \left(- \ln(2) \frac{t + t_0}{\lambda_i} \right), \quad (2.29)$$

where, for each element i , f_i is the abundance of the radioactive isotope relative to the sum of all isotopes of the element, X_i^0 the isotope concentration in the silicate mantle at the formation time of the Calcium Aluminium Inclusion Calcium Aluminium-rich Inclusions (CAI) (4.55 Gyr ago), Q_i the specific heat production, λ_i the half-life, t_0 the assumed formation time of the magma ocean (e.g. 2 or 100 Myr after the CAI as in experiment 4 in Table 3.1), and t the time (with $t > t_0$). For the long-lived elements, the initial isotope concentration X_i^0 is calculated by scaling back in time the present-day concentration of the corresponding element according to the isotope half-life. Table 2.2 displays the parameters of Eq. (2.29) for each isotope. Q_r is plotted in Fig. 2.6.

The energy released by the radioactive isotopes' decay is made available to the whole magma ocean volume, which implies complete incompatibility in the solid mantle upon crystallization. This formulation maximizes their contribution as a source to the energy balance.

2.5 OUTGASSING

The building blocks of the outgassing calculation is the solubility curve and the mass conservation between the three components of the system: solid mantle, liquid mantle and atmosphere.

Table 2.2: Parameters used in radiogenic heat production calculation (Eq. (2.29))

Radioactive isotopes	Abundance f	Concentration X^0	Half-life λ (yr)	Heat production Q (W/kg)
^{238}U (*)	0.9928	$6.23 \cdot 10^{-8}$	$4.47 \cdot 10^9$	$9.46 \cdot 10^{-5}$
^{235}U (*)	0.0072	$2.6 \cdot 10^{-6}$	$0.704 \cdot 10^9$	$5.69 \cdot 10^{-4}$
^{40}K (*)	$1.19 \cdot 10^{-4}$	$3.77 \cdot 10^{-3}$	$1.25 \cdot 10^9$	$2.94 \cdot 10^{-5}$
^{232}Th (*)	1	$1.53 \cdot 10^{-7}$	$14.5 \cdot 10^9$	$2.54 \cdot 10^{-5}$
^{26}Al (†)	$5.25 \cdot 10^{-5}$	$8.86 \cdot 10^{-3}$	$0.717 \cdot 10^6$	0.455
^{60}Fe (†)	$1.15 \cdot 10^{-8}$	$1.81 \cdot 10^{-1}$	$2.61 \cdot 10^6$	0.041

(*) Parameter values for undepleted mantle (Schubert et al., 2001)

(†) Parameter values for CI abundances (Barrat et al., 2012)

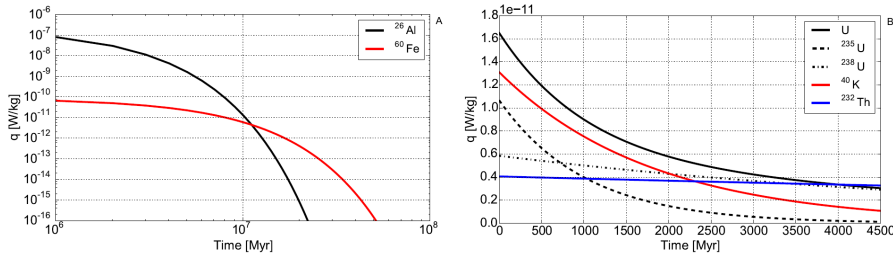


Figure 2.6: **A:** Energy contribution by radioactive decay of short-lived elements ^{26}Al and ^{60}Fe with time; **B:** Energy contribution of long-lived radioactive decay elements ^{235}U , ^{238}U , ^{40}K and ^{232}Th with time.

2.5.0.1 Henry's law and solubility difference

Henry's law is often mistaken for the solubility phenomenon. Henry's empirical law does not include dissolution of the solvent molecules in the solute. It only concerns molecular diffusion, enhanced by pressure, into a liquid reservoir and it often has the form of a power law. Instead, the solubility of water into silicate melt is a chemical reaction that involves both molecules and ions of water. At equilibrium the following relation holds:



It is evident that $\text{O}_{\text{melt}}^{2-}$, or else the oxidation state of the mantle, modulates the balance. Solubility of a volatile in liquid volume is evaluated at the liquid-vapor interface as the concentration X_i in the volume that is balanced by a vapor of partial pressure P_i .

The evolution of the concentration of volatiles in the mantle and their outgassing into the atmosphere is calculated along with the thermal evolution. Assuming that the volatile pressure in the gas phase

and their concentration in the melt are at saturation, I use solubility curves to calculate the concentration and gas pressure in the melt for each volatile.

2.5.1 Solubility in a circulating fluid

In the overturning [MO](#) the melt circulates along the streamlines of a convective cell. The melt equilibrates with vapor at the minimum pressure that it is subjected to. It is explained below why the volatile pressure that matters for a well mixed melt volume is therefore the pressure at the boundary $z=0$ i.e. at surface. I refer to the example of water but the same holds for carbon dioxide.

The solubility of volatiles H_2O in silicate melts is monotonic (see [Figure 3.4](#)). It increases with compression until 0.2 GPa and shallows further on the increase as [Manning \(2018\)](#) review characteristically observes. A minimum vapor partial pressure corresponds to a low concentration in the melt. Any unit volume of melt that is equilibrated at the surface has water concentration $X_{i,0}$ and vapor pressure $P_{i,0}$. It is found at saturation point for that depth, let it be $z=0$. When the unit volume incompressibly sinks deeper ($z>0$), the fluid parcel will become undersaturated with respect to water at greater depth because pressure $P_{i,z}$ will increase. The concentration $X_{i,0}$ will not likewise raise because the water content will be retained in the constant unit volume. Unless there is another source of water into the melt at large depth, there is no reason to assume that the increase in water content at in situ generated melts or the change in saturation state of the sinking volume will affect the amount of water stored in the unit volume along its convective trajectory. The solidified volume of minerals, at least those in the partial melt region where $\phi > 0.40$, also store water in their structure according to the partition coefficients. However, those crystals could not melt and serve as sources of water into the mixed melt volume at the same depth, because the local temperature conditions ensure that those minerals form and remain solid, hence their existence. This is a principle of the [COMRAD](#) model, on which I justify the existence of neutrally buoyant solidified volume that follows the melt volume fraction $\phi = \frac{T-T_{sol}}{T_{liq}-T_{sol}}$ distribution throughout the [MO](#) depth.

For a parcel on the upwelling branch of the convective cell, the saturation varies as follows: assume a unit volume of melt at large depth $P_{i,z}$ that contains $X_{i,z}$ volatile and equilibrated in situ at the saturation point ($P_{i,z}, X_{i,0}$). When it upwells to the surface it will become oversaturated due to the pressure drop to $P_{i,0}$ and the constant concentration it maintains ([Figure 3.4](#)). Consequently it will outgas its volatile content. This will decrease the concentration $X_{i,z}$ until it matches the vapor saturation once at the new ambient pressure $P_{i,0}$. By the above argument, in the dynamical setting of the circulation, the solubility

evaluated at the surface vapor pressure serves as a global minimum of the convecting domain. Solubility in [COMRAD](#) is evaluated at $z=0$.

2.5.2 Solubility curves for H_2O and CO_2

For H_2O the (Caroll et al., 1994) solubility expression is used:

$$P_{sat,H_2O} = \left(\frac{X_{H_2O}}{6.8 \cdot 10^{-8}} \right)^{(1/0.7)}, \quad (2.31)$$

and for CO_2 (Pan et al., 1991):

$$P_{sat,CO_2} = \frac{X_{CO_2}}{4.4 \cdot 10^{-12}}. \quad (2.32)$$

This way I obtain the saturation vapor pressure over melt with a given volatile concentration. Due to efficient mixing the volatile concentration is assumed homogeneous throughout the magma ocean.

Since the outgassing at a certain temperature depends on the amount of melt in the system, the solidus profile plays a decisive role in it. Katz et al. (2003) found a T_{sol} dependence on water that covers a range of pressure until 3 GPa and a range of temperature until 1600 K. The T_{sol} behavior at the remaining depth is often extrapolated. The water solubility isopleths P-T predict the water content along the solidus. A similar plot of the water solubility isopleths for the $CaMgSiO_6$ - H_2O system has been formerly calculated by Perchuk et al. (1991) as well as by Makhlufov et al. (2017) who both find a shallower solidus slope in comparison to Katz et al. (2003). Solidus dependence on the water content is debated. In this work such dependence is ignored.

2.5.3 Volatile mass balance

Upon solidification, part of the volatile budget partitions into the solid mantle according to the partition coefficients of lherzolite for the upper mantle ($\kappa_{vol,lhz}$) and of perovskite for the lower mantle ($\kappa_{vol,pv}$) (see Table 2.3 for values). By calculating the volatile content stored in the liquid and solid phases of the mantle, I estimate the mass balance for each volatile at every time iteration t as follows:

$$\begin{aligned} M_{l,t_0} X_{vol,t_0} = & P(X_{vol,t}) \frac{4\pi R_p^2}{g} \\ & + M_{s,pv} \kappa_{vol,pv} X_{vol,t} + M_{s,lhz} \kappa_{vol,lhz} X_{vol,t} \\ & + M_{l,z < z_{RF}} X_{vol,t} + M_{l,z > z_{RF}} X_{vol,t} \Pi \\ & - M_{l,z > z_{RF}} X_{vol,t-dt} (1 - \Pi), \end{aligned} \quad (2.33)$$

where M_{l,t_0} is the initial ($time = t_0$) mass of the liquid mantle, X_{vol,t_0} the initial volatile concentration in the melt, $P(X_{vol,t})$ the saturation pressure of the volatile for the respective concentration $X_{vol,t}$ at time t ,

M_s is the mass of solid mantle in perovskite and in lherzolite, $\kappa_{vol,pv}$, $\kappa_{vol,lhz}$ the partition coefficients of the volatile in lherzolite and perovskite, respectively, M_l the mass of the melt at depth z either shallower ($z < z_{RF}$) or deeper than the rheology front ($z > z_{RF}$), and $X_{vol,t-dt}$ the concentration of the volatile in the previous time step; Π takes values within 0 and 1. Comparing the percolation velocity (Solomatov, 2007) to the rheology front velocity I calculate a volumetric fraction Π of the total melt volume that circulates across the RF. Therefore, $\Pi = 0$ indicates that none of the melt located below the RF percolates above it and thus its enclosed volatiles are not available for outgassing at the surface. Likewise, $\Pi = 1$ indicates that all the melt below the RF percolates and gets mixed in the convection occurring above, rendering the included volatiles available for outgassing. The last term on the RHS of Eq. (2.33) thus represents the volatile mass trapped in the liquid below RF and is evaluated at the concentration of the previous time step.

Equation (2.33) combined with either Eq. (2.31) or (2.32), forms a system of two equations in the unknowns (P, X) for each volatile. In the case of H_2O , Eq. (2.31) is non-linear with respect to X_{H_2O} . An iteration scheme based on the bisection method (Newton) is built in order to find a numerical solution with an error of 0.01 bar. For CO_2 , the relation is linear and it is sufficient to substitute Eq. (2.32) into Eq. (2.33).

2.6 SECONDARY ATMOSPHERE

No prior nebular atmosphere is assumed in the simulations. Note however, that the atmospheric vapor partial pressure is non-zero at the first time step. Upon initialization of the model, the total volatile reservoir is distributed between the global MO melt volume and the atmosphere, such that the initial $P_{i,0}$ and $X_{i,0}$ satisfy the saturation assumption. I call such process of finding the initial equilibrium state, the spinup phase of the model.

For every new mantle layer that solidifies volatile enrichment takes place in the remaining melt. Since the volatiles' saturation pressure increases monotonically with concentration (Section 2.5), the equilibrium gas pressure also increases, and results in a progressive build-up of atmospheric mass at the planet surface.

Both atmospheric models employed in this study incorporate several assumptions for the atmospheric properties profile. By way of being 1D models certain simplifications are inevitable, however, they capture the effect of thermal blanketing which is the focus of this study.

The adoption of the convective-radiative approach for the lower atmosphere corresponds to either a dry or moist adiabat for the profile of temperature. In addition, the optical thickness of the atmo-

sphere determines the altitude where the separation between the troposphere (convective) and the stratosphere (radiative) regime occurs.

I adopt two alternative approaches to model the atmosphere generated upon magma ocean outgassing: i) a grey approximation after Abe et al. (1985) and ii) a non-grey based on a spectrally resolved OLR (Katyál et al., 2019). Two gas species H_2O and CO_2 are treated in the first, while a pure H_2O vapor composition is assumed in the second Katyál et al. (2019). Turbulent mixing ensures efficient heat diffusion into and warming of the surface boundary layer. It is assumed that the lowermost layer of the atmosphere has the same temperature as that of the surface ($T_{\text{surf}} = T_{\text{atm}}$).

2.6.1 Grey atmospheric model

The grey approximation that I use is derived in Abe et al. (1985). It considers the absorption of thermal radiation to be independent of the wavelength. Both outgassed species H_2O and CO_2 absorb significantly in the spectral region where thermal energy is emitted from the surface of the Earth, and are therefore greenhouse contributors. By absorbing radiative energy, they exert a direct control on the surface temperature. Water is the most potent greenhouse agent of the two under normal atmospheric conditions ($P_0 = 101325 \text{ Pa}$, $T_0 = 293 \text{ K}$) (see e.g. Pierrehumbert, 2010). For the H_2O absorption coefficient the value $k_{0,\text{H}_2\text{O}} = 0.01 \text{ m}^2/\text{kg}$ in the mid-infrared window region 1000 cm^{-1} is adopted, after Abe et al. (1988). CO_2 is accounted for with absorption coefficient $k_{0,\text{CO}_2} = 0.001 \text{ m}^2/\text{kg}$ (Yamamoto et al., 1952). Basic description of the Abe et al. (1985) model workings can be found in the next section 2.6.1.1.

2.6.1.1 The Abe & Matsui 1985 model

Assuming optical thickness 1 for a dense atmosphere and evaluating radiative balance at normal optical depth $2/3$, Abe et al. (1985) find that the opacity τ_i for a given species i is proportional to the absorption k' :

$$\tau_i = \frac{3k'P_i}{2g}, \quad (2.34)$$

where P_i is the partial pressure of the species i in the atmosphere and k' is the absorption coefficient under a certain pressure P_i . k' is proportional to the atmospheric absorption coefficient $k_{0,i}$ under normal atmospheric conditions (P_0, T_0) and can be defined as follows:

$$k' = \left(\frac{k_{0,i}g}{3P_0} \right)^{1/2}. \quad (2.35)$$

Upon including Eq. (2.35) into the opacity relation (2.34), the opacity τ_i for each volatile is obtained for an atmosphere of pressure

higher than the normal conditions P_0 (as in Pujol et al. (2003) and Elkins-Tanton (2008)):

$$\tau_i = \frac{3kM_{i,atm}}{8\pi R_p^2}, \quad (2.36)$$

where, k is the absorption coefficient of the volatile at the surface, R_p the planetary radius, and $M_{i,atm}$ the mass of the volatile i in the atmosphere.

In the grey approximation, the total opacity of the atmosphere (τ) is given by the sum of the opacities of each gas, i.e. $\tau = \sum_i \tau_i$ (Pujol et al., 2003; Elkins-Tanton, 2008). The opacity is a measure of the radiative absorption through atmospheric layers and is inversely proportional to their emissivity ϵ . Following Abe et al. (1985), the two quantities are linked as follows:

$$\epsilon = \frac{2}{2 + \tau}. \quad (2.37)$$

The atmosphere is assumed to be in radiative-convective equilibrium and the TOA is defined to occur at the base of the stratosphere, above which the temperature is governed by pure radiative balance. The assumptions include the plane-parallel approximation for the atmospheric layers and ignore radiative contributions from directions wider than 60° degrees between neighboring layers. More information on the derivation of the above equations can be found in Abe et al. (1985).

2.6.1.2 Grey - interior coupling

What is especially important for coupling the grey model of Abe et al. (1985) with our model is that the downward radiation at the TOA is set to the incoming stellar flux F_{Sun} , which depends on the incident radiation S_0 at the assumed orbital distance. This in turn is related to the BB equilibrium temperature T_{eq} of the planet through the Stefan-Boltzmann law:

$$F_{Sun} = (1 - \alpha) \frac{S_0}{4} = \sigma T_{eq}^4, \quad (2.38)$$

where α is the albedo and σ the Stefan-Boltzmann constant. The resulting net upward flux at the top of the atmosphere (F_{grey}) is given by (Abe et al., 1985):

$$F_{grey} = \sigma \epsilon (T_{surf}^4 - T_{eq}^4). \quad (2.39)$$

According to Eq. (2.39), the net radiative flux at the TOA is positive for $T_{surf} > T_{eq}$. I adopt the convention of positive flux to represent planetary cooling. In order to find a state of the system that satisfies

the energy balance, assuming that the radiative atmospheric adjustment is instantaneous, I require that the convective heat flux F_{conv} at the top of the magma ocean is equal to the flux at the TOA, i.e.

$$F_{conv} = F_{grey}. \quad (2.40)$$

Eq. (2.40) together with Eq. (2.25) form a system of two equations for two unknowns T_{surf} and F_{conv} . For a given potential temperature, I solve this system using an iterative scheme built according to the method of Lebrun et al. (2013) with an accuracy of 10^{-2} W/m².

Unless $T_{surf} < T_{eq}$, the RHS of Eq. (2.40) is always positive, so cooling is ensured. With this approach I can estimate finite solidification intervals of a magma ocean coupled to a grey atmosphere composed of H₂O and CO₂.

2.6.1.3 The CO₂ absorption coefficient

A higher $k_{0,CO_2} = 0.05$ m²/kg value has been employed by Elkins-Tanton (2008) (along with other values) and by Lebrun et al. (2013) that was calculated by Pujol et al. (2003) in order to reproduce present day's Earth Climate Sensitivity (ECS). ECS corresponds to an increase of about 2°C in surface mean temperature (Flato et al., 2013) and is a combined response of the climate system to the radiative forcing from doubling the atmospheric CO₂ abundance relative to its pre-industrial levels. Using it is a good practice for studying the role of CO₂ radiative forcing on today's temperate Earth climate, within which the water vapor is not saturated in the atmospheric column. The presence of a liquid ocean is a strong constraint on the ECS and affects the overlying atmospheric profile through the inter-component exchange of vapor or "hydrological cycle" (Held et al., 2006), provided that no runaway greenhouse regime ensues. Extrapolating today's climate sensitivity to the mean surface temperature of the magma ocean (1500 K) that is well above today's average surface temperature (288 K) is unsuitable for our study. In addition, the radiation spectra of the MO is shifted to shorter wavelengths where the IR absorption lines of CO₂ (Plass, 1956) become less important (Section 2.1.5). I therefore avoid using the ECS-product value for k_{0,CO_2} because it could overestimate the role of its radiative forcing on a planet with qualitatively different surface and atmospheric dynamics. Therefore, I use for k_{0,CO_2} the lower value of 0.001 m²/kg (Elkins-Tanton, 2008).

2.6.2 Line-by-line atmospheric model

An alternative approach to using the grey model is to employ a line-by-line (line-by-line radiative transfer scheme (lbl)) atmospheric approach to calculate the outgoing radiation. The advantage of this approach is that it provides a detailed calculation of wavelength-

dependent long-wave emission. I assume a 100% water vapor atmosphere (“steam atmosphere”) as commonly used by various authors when treating magma ocean planets or exoplanets with water-dominated atmospheres (e.g. Hamano et al., 2013; Massol et al., 2016; Schaefer et al., 2016).

2.6.2.1 The Katyal et al. 2019 lbl model

Note that the MO surface temperature is above the critical point of water ($T = 647$ K). The lower atmosphere is assumed to be unsaturated and follows a dry adiabat. The upper atmosphere follows the moist adiabat. The two adiabats’ intersection marks the tropopause height and the system is extended upwards until pressure level of 1 Pa. This approach is similar to the one adopted by Kasting (1988) and Goldblatt et al. (2013).

For a range of surface temperatures T_{surf} and surface pressures P_{H_2O} , the emitted radiation is calculated for the spectral range 20–29,995 cm^{-1} . The temperature profiles of the atmosphere as described above are used and the radiation transfer is evaluated with a line-by-line model (Schreier et al., 2014). Integrating the emitted radiation at the TOA (corresponding to pressure 1 Pa), the total outgoing radiation flux OLR_{TOA} is obtained. The model is described in detail in Katyal et al. (2019).

2.6.2.2 Lbl atmospheric data product

Figure 2.7 shows the OLR on a 50×8 grid of (T_{surf}, P_{H_2O}) points respectively, which I used as input for the lbl simulations. The OLR data at each grid point have been obtained with the method described in the companion paper by Katyal et al. (2019) using a line-by-line code (GARLIC) of Schreier et al. (2014) with HITRAN 2012 (Rothman et al., 2013).

The grid spans surface temperature from 650 to 4000 K and water vapor surface pressure from 4 to 300 bar. It is irregularly spaced. The sampling is sparser (8 values) on the pressure axis for $P \in [4, 300]$ bar. For the surface vapor pressure the values 4, 25, 50, 100, 200 and 300 bar were used. The grid is denser over the temperature range where the highest rate of outgassing takes place. For the melting curves used in this study (J. Zhang et al., 1994; Hirschmann, 2000; Herzberg et al., 2000; Fiquet et al., 2010; Andraut et al., 2011), this region is mostly confined to the interval $T_s \in [1400, 1800]$ K where the OLR was sampled with 20 K resolution. A coarser resolution of 100 K was employed outside this range. In order to obtain the OLR values at (P, T) points intermediate to the grid points, an interpolation method was implemented after Rossum et al. (2001). The method of interpolation is subject to limitations. The minimum number of data points required along the interpolation axis is: $(N + 1)^2$, with $N=1$

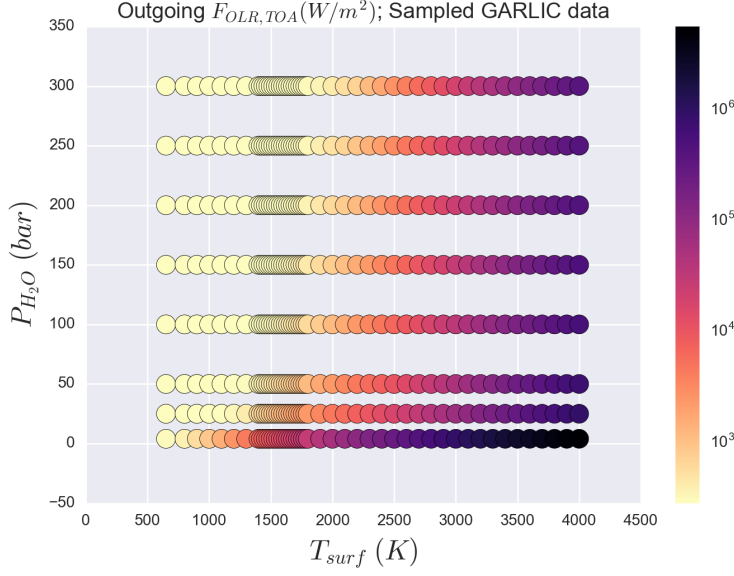


Figure 2.7: Figure from Nikolaou et al. (2019) © AAS. Reproduced with permission. OLR_{TOA} data product sampled on the (T_{surf}, P_{H_2O}) -space. Obtained using the [bl](#) radiative transfer model, detailed calculation in Katyal et al. (2019).

for bilinear, and $N=3$ for cubic interpolation (Rossum et al., 2001). A cubic spline would need by definition minimum 12 points on every axis. That criterion was not met by the available 8 pressure values, therefore the bilinear method was chosen as suitable for this dataset.

In order to estimate the interpolation error, the interpolated field was compared with an independent set of grid-intermediate data points obtained from the atmospheric model. The relative interpolation error amounts from 10%, for fluxes of the order of 10^6 W/m^2 , to about 1%, for fluxes of the order of 10^2 W/m^2 . The 10% maximum of occurs at pressures lower than 10 bar and high temperatures. The minimum 1% occurs for high pressures and temperatures at the lower end of the dataset. Therefore, the interpolation quality is acceptable for this study that focuses on the coolest end of magma ocean phase where the outgassed atmosphere has high pressure and the error minimizes (1-2 W/m^2).

The data of Fig. 2.7 represent the OLR at the TOA with a viewing angle of 38° .

Finally, in order to satisfy the requirement of our iteration algorithm for surface temperatures lower than $T_{crit} = 647$ K, which are not covered by the gridded data product, I use a fit to the [OLR](#) data of (Nakajima et al., 1992). This aspect does not affect our results for the solidification process, which occurs for $T_{surf} \approx T_{RF,0} \gg T_{crit}$, but ensures that the iteration algorithm runs unhindered until convergence to the solution.

2.6.2.3 Lbl atmospheric radiation transfer - interior coupling

I impose a balance between the net energy flux at TOA and the magma ocean cooling flux F_{conv} such that:

$$F_{conv} = OLR_{TOA} - F_{Sun}. \quad (2.41)$$

Equations (2.25) and (2.41) form a system of two unknowns T_{surf} and F_{conv} , which I solve iteratively with a tolerance of 10^{-1} W/m². The resulting flux that balances the RHS of Eq. (2.41) can be either positive or negative, corresponding to a cooling or warming case, respectively.

2.6.3 Incoming stellar radiation

The incoming stellar radiation is accounted for in the calculation of the net atmospheric outgoing flux in both methods I employed for the atmosphere (Eq. (2.40) and (2.41)). For the young Sun I used a lower irradiation value following the expression for the time dependence of the solar constant of Gough (1981); otherwise I used today's value (1361 W/m², see Table 2.4).

Calculating the planetary albedo is outside the scope of this study and is instead used as an input parameter. The suggested albedo (α) for a cloudless steam atmosphere lies within the range 0.15–0.40 (Kasting, 1988; Goldblatt et al., 2013; Leconte et al., 2013; Pluriel et al., 2019). Unless otherwise stated the value 0.3 is employed.

2.7 END OF THE MAGMA OCEAN PHASE

The end of the magma ocean phase is defined as the point in time when the rheology front reaches the surface. At that stage, the mantle adiabat has potential temperature $T_{RF,0}$ such that all mantle layers have a melt fraction lower than ϕ_c . Although some melt still remains enclosed in the solid matrix, the mantle subsequently behaves as a solid. Moreover, the adiabatic profile used for the solid mantle implies that solid state convection has fully developed. I apply the scaling of Eq. (2.25) in order to represent the convective heat flux, replacing the melt viscosity with the solid viscosity (calculated with Eqs. (2.23) and (2.24)) in the calculation of Ra . This results in much lower values of F_{conv} for the same potential temperature compared to the liquid-like regime. As such the surface conditions following the end of the MO stage, represent the specific case of an immediate onset of solid state mantle convection after end of the magma ocean and apply only for the grey atmosphere. That is an end member case within the geodynamic assumptions. However, it is stressed that the thermal evolution model is designed to cover only the time until solidification is reached.

2.8 MODEL CONSTANTS

Table 2.3 includes the constants and parameters used in the simulations unless otherwise explicitly stated.

Table 2.3: Model constants and parameters.

Parameter	Value	Unit	Description
R_p	6371	km	Planetary radius
R_b	3481	km	Core mantle boundary radius
g	9.81	ms^{-2}	Gravity acceleration
$k_{0,\text{H}_2\text{O}}$	0.01	m^2/kg	Absorption coeff. at P_0, T_0
k_{0,CO_2}	0.001	m^2/kg	Absorption coeff. at P_0, T_0
P_0	101325	Pa	Normal atmospheric pressure for $k_{0,\text{vol}}$
T_0	300	K	Normal atmospheric temperature for $k_{0,\text{vol}}$
α_0	$3 \cdot 10^{-5}$	K^{-1}	Mantle thermal expansivity
K_0	200	GPa	Mantle bulk modulus
K'	4	–	P -derivative of mantle bulk modulus
m	0	–	Parameter in Eq. (2.17)
c_P	1000	$\text{J kg}^{-1}\text{K}^{-1}$	Mantle isobaric thermal capacity
κ_T	10^{-6}	m^2s^{-1}	Mantle thermal diffusivity
k_T	$\kappa_T * (\rho c_P)$	$\text{W K}^{-1}\text{m}^{-1}$	Mantle thermal conductivity
ρ_l	4000	kg m^{-3}	Melt density
ρ_s	4500	kg m^{-3}	Solid density
ϕ_C	0.4	–	Critical melt fraction
η_0	$4.2 \cdot 10^{10}$	Pa s	Solid viscosity prefactor in Eq.(2.23)
E	240	kJ mol^{-1}	Activation energy
V	5	$\text{cm}^3 \text{mol}^{-1}$	Activation volume
R	8.314	$\text{J mol}^{-1} \text{K}^{-1}$	Ideal gas constant
A_G	3.9759	–	Prefactor in Eq. (2.21) calibrated for basanite
B_G	*	K	Parameter in Eq. (2.21)
C_G	*	K	Parameter in Eq. (2.21)
A_K	0.00024	Pa s	Prefactor for hydrous liquid in Eq. (2.20)
B_K	4600	K	Parameter for hydrous liquid in Eq. (2.20)
C_K	1000	K	Parameter for hydrous liquid in Eq. (2.20)
$\kappa_{\text{H}_2\text{O},pv}$	$1.0 \cdot 10^{-4}$	–	H_2O partition coeff. in solid perovskite
$\kappa_{\text{H}_2\text{O},lhz}$	$1.1 \cdot 10^{-2}$	–	H_2O partition coeff. in solid lherzolite
$\kappa_{\text{CO}_2,pv}$	$5.0 \cdot 10^{-4}$	–	CO_2 partition coeff. in solid perovskite
$\kappa_{\text{CO}_2,lhz}$	$2.1 \cdot 10^{-3}$	–	CO_2 partition coeff. in solid lherzolite

*The value of this parameter is dynamically calculated during the simulation.

2.9 EXPERIMENTAL SETTING “REFERENCE A”

Since the model has numerous input parameters, I define a set of parameter values, hereafter called “Reference-A” (Ref-A for brevity) model setting, with respect to which I perform changes and comparisons. Hereafter it will be referred to as “Ref-A” setting. Parameter values of Ref-A setting are reported in Table 2.4. This model is intended to be as straightforward as possible, to facilitate model comparison. It does not include radioactive heat sources, the melt viscosity only depends on temperature according to Eq. (2.20), the abundance of volatiles is set to today’s Earth observed reservoirs (e.g. Ingersoll, 2013), and it uses the atmospheric grey model for the two species H_2O and CO_2 . Additional aspects such as the solar irradiation and type of melting curves used are also defined. For completeness, note here that the suffix “-A” is necessary in order to mark a clear distinction to the “Reference-B” special setting that is used in Section 3.3. “Ref-B” differs from the “Ref-A” in that it employs the [lbi](#) atmosphere approximation which by construction does not include CO_2 .

The experiments are organized as follows: I firstly examine the thermal and dynamical evolution of the magma ocean in the absence of atmosphere and under the influence of grey or [lbi](#) atmospheric blanketing (Section 3.1). I examine the simultaneous evolution of H_2O and CO_2 outgassing (Section 3.2), and vary the initial volatile abundances in order to calculate their effect on the magma ocean solidification time (Section 3.2). I quantify the minimum remnant volatiles in the mantle at the end of the magma ocean (Section 3.2.2) and I study in particular the influence of the choice of melting curves on the evolution of water outgassing. Upon concluding the overview of the coupled interior-atmosphere system, I study the separate influence of each parameter (or parameterized process) upon the solidification time (Section 3.3). In Sections 4.1–4.3.1 I shift the focus to the influence of the steam [lbi](#) atmosphere and use the atmospheric calculations of Katyal et al. (2019). I show the qualitative difference between the grey and [lbi](#) water vapor atmospheres (Section 4.1). I discuss the mechanism which distinguishes the short-term from the long-term magma ocean regime (Section 4.2), and I find the critical albedo that separates the two, for a constant water inventory at a given distance from the star (Section 4.3). Finally, in Section 4.3.1, I expand the calculations of the critical albedo to depend on the outgassed water vapor and the temperature of the rheology front at the surface. The relevance of the results in the context of Venus and Mars are presented in Section 5.1 followed by the results for exoplanets in Section 5.2. A cumulative overview of the solidification time according to the factors examined is provided in Chapter 6 together with the discussion.

Table 2.4: Reference-A setting parameter values and components. For complementary use to the results presented in Table 3.1.

Parameter	Description	Value/Type	Unit/Info
Atmosphere	Type of approximation	grey	Eq. (2.39) Abe et al. (1985)
k_{0,H_2O}	Absorption coeff. at normal atmospheric conditions	0.01	m ² /kg
k_{0,CO_2}	Absorption coeff. at normal atmospheric conditions	0.001	m ² /kg
H ₂ O content	Total water reservoir	300	bar
$X_{H_2O,0}$	Initial H ₂ O mantle abundance	410	ppm
CO ₂ content	Total CO ₂ reservoir	100	bar
$X_{CO_2,0}$	Initial CO ₂ mantle abundance	130	ppm
S	Solar constant (S_0)	1361	W/m ²
α	Planetary albedo	0.30	-
$T_{p,0}$	Initial potential temperature	4000	K
D	Initial MO depth	2890	km
η_l	Melt viscosity parameterization	$\eta_l = f(T)$	(Eq. 2.20)
q_r	Radioactive heating	0	not included
t_{planet}	Planet accretion time	100	Myr (employed for q_r only)
T_{sol}, T_{liq}	Melting curves	“synthetic”	Herzberg et al. (2000), Hirschmann (2000) and Fiquet et al. (2010) (Section 2.3.1)
$T_{RF,0}$	Temperature of rheology front at $z = 0$	1645	K
F_{conv}	Convective heat flux parameterization	soft turbulence	Eq. (2.25) Solomatov (2007)

2.10 CODE FLOW

A schematic of the code flow is shown in Figure 2.8.

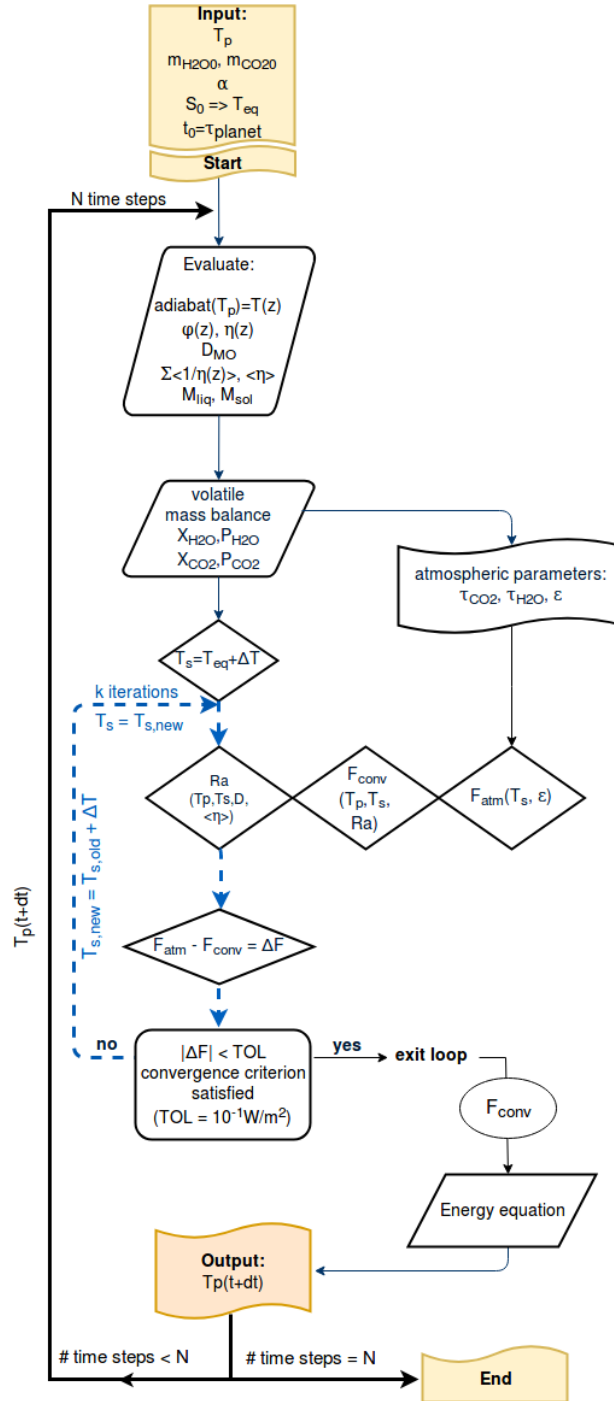


Figure 2.8: COMRAD model code flow

MAGMA OCEAN THERMAL EVOLUTION WITH A GREY ATMOSPHERE

In this chapter I use the Ref-A setting to answer the research questions Q1, Q2 and Q3:

- Q1 What are the geodynamic characteristics of a solidifying MO during the thermal evolution of the atmosphere-interior coupled system?
- Q2 How was the secondary atmosphere formed following the evolution of volatile outgassing from the magma ocean?
- Q3 How long does the MO last with respect to every physical process included in the simulations?

3.1 THERMAL AND DYNAMICAL EVOLUTION

In a similar fashion to prior studies of the magma ocean solidification (Zahnle et al., 1988; Abe, 1997; Elkins-Tanton, 2008; Hamano et al., 2013, 2015; Lebrun et al., 2013; Monteux et al., 2016; Schaefer et al., 2016; Hier-Majumder et al., 2017) I present the thermal evolution using the state variables: surface temperature, potential temperature, heat flux, Ra number, and MO depth evolution. This enables both model validation and comparison. I adopt the multi-panel approach of Lebrun et al. (2013) that is convenient for comparisons between varying modeling approaches. I performed three simulations for the following cases: i) absence of atmosphere referred to as the black body case, ii) a grey atmosphere composed of both H_2O and CO_2 “gr- H_2O/CO_2 ”, iii) a grey atmosphere composed of only H_2O “gr- H_2O ” (Fig. 3.1). A fourth simulation iv) a H_2O atmosphere treated with the line-by-line `lbl` radiative transfer model is included. This serves as a brief point of comparison to address the effect of atmospheric representation and appears only in Figure 3.1 and in Table 3.1. Apart from the representation of the atmosphere or absence thereof, all aspects of the model follow the Ref-A case (Table 2.4), which employs the grey approximation.

Commonly in all simulations, the T_p and T_{surf} co-evolve until an abrupt difference between the two marks the end of the magma ocean (Fig. 3.1B dashed lines); the liquid-like behavior comes to an end and a layer with a melt fraction of 40% or lower remains. The average viscosity increases by more than 8 orders of magnitude across the critical melt fraction, taking values from 10^8 to 10^{18} Pa·s (not shown).

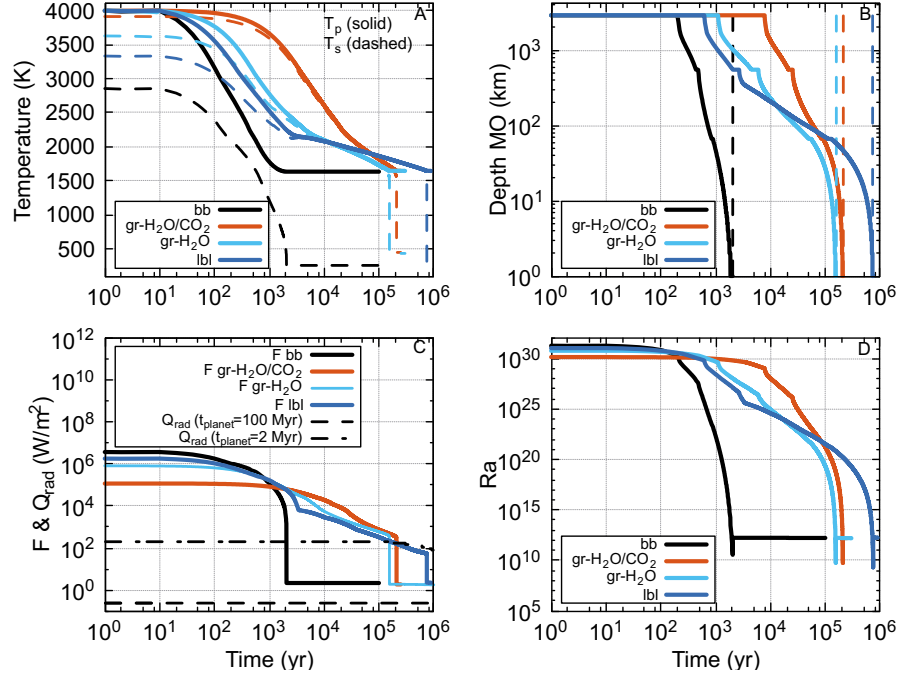


Figure 3.1: Figure from Nikolaou et al. (2019) © AAS. Reproduced with permission. Thermal evolution of black body (bb), grey H_2O atmosphere (gr- H_2O), grey H_2O/CO_2 atmosphere (gr- H_2O/CO_2), and line-by-line H_2O atmosphere (lbl). **A:** Evolution of potential (solid) and surface (dashed) temperature; **B:** Evolution of the depth of the magma ocean (dashed lines indicate the end of MO); **C:** Evolution of convective energy sink compared to the energy source of radioactivity. Note that the contribution of the radioactive heat sources is not included in the Ref-A settings and is only plotted for comparison; **D:** Evolution of Ra number. Apart from the explicit differences in the atmospheric component, all other parameters are taken from the Ref-A case (Table 2.4).

A smooth variation across this interval would be difficult to justify under the assumption of fractional crystallization (e.g. Marsh, 1981). At this point, the whole domain switches to low cooling flux that characterizes solid-like convection (Eq. 2.25) and the surface temperature drops abruptly, while the potential temperature remains unaffected.

The BB thermal evolution compares well with that presented by Lebrun et al. (2013). It demonstrates the highest $T_p - T_s$ difference. The mantle consequently cools rapidly (0.002 Myr) with the highest convective flux ($F = 5 \cdot 10^6 - 10^4 \text{ W/m}^2$), caused by this large temperature difference. Longer solidification times (0.150 Myr) are found by Monteux et al. (2016) who assume a BB radiative cooling ($F = 10^5 - 10^2 \text{ W/m}^2$) but a different interior model with a heat contribution from the core. The BB case is only relevant for planets that lose their outgassed atmosphere instantaneously.

For a planet that retains its atmosphere, the grey approximations show that the presence of the additional greenhouse species CO_2 con-

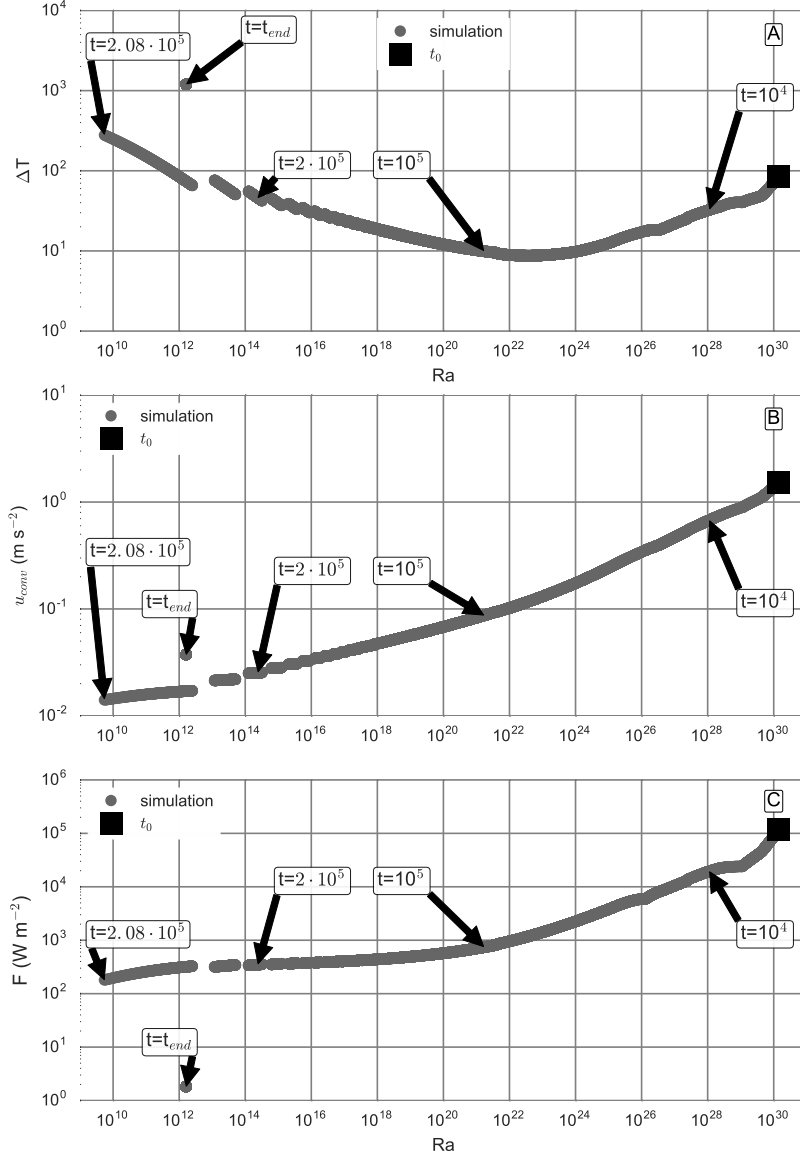


Figure 3.2: Evolution of **A**: ΔT , **B**: u_{conv} convective velocity and **C**: F_{conv} as a function of Ra throughout the **MO** phase. Various points in time are indicated in units of years. t_{END} corresponds to the Ref-A simulation result (208,600 yr) for the **MO** duration.

tributes only 0.05 Myr to the solidification time and is less significant in comparison to the water (0.16 Myr vs 0.21 Myr **MO** duration). The longer solidification time (≈ 0.4 Myr) obtained by Lebrun et al. (2013) for their grey two-species case is consistent with absorption coeffi-

cient $k_{0,CO_2} = 0.05$, which is likely to be rather high for those climates (see Section 2.6.1). The grey approach employed in this study follows Abe et al. (1985) and should not be identified with other grey models used in the literature: The study of Hamano et al. (2013) expands on the Nakajima et al. (1992) grey model and employs supercritical water thermal capacities. The study of Hier-Majumder et al. (2017) formulates a hybrid energy balance for the atmosphere employing elements from both Abe et al. (1985) and Hamano et al. (2013). For potential temperature equal to the equilibrium temperature it results in net radiative warming of the planet. Moreover, the study of Hier-Majumder et al. (2017) preserves the mantle fully molten for the majority of the MO period due to the lack of convective cooling sink. The slow solid-matrix compaction process provided from their detailed melt/volatile percolation model further increases the solidification time (3 Myr) in comparison to our study. Lastly, I obtain lower solidification time in comparison to Hamano et al. (2013) who define the MO end at the surface solidus and not at the higher temperature of the critical melt fraction.

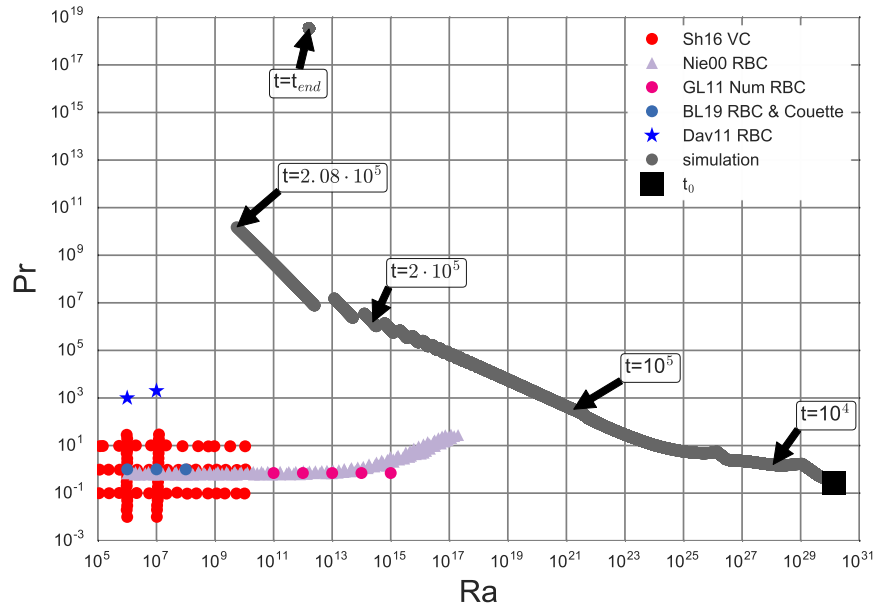


Figure 3.3: Evolution of Pr and Ra parameters in a solidifying magma ocean simulation. The range of laboratory (Niemela et al., 2000b; Davaille et al., 2011; Shishkina et al., 2016) or numerical (Grossmann et al., 2011; Blass et al., 2019) experiments is plotted for comparison to the this study's simulations. Simulation parameters follow the Ref-A setting. Initial conditions (t_0) and various points in time are indicated in units of years. t_{END} corresponds to the Ref-A simulation result (208,600 yr) for the MO duration.

The cooling path can be followed from the convective heat flux, the MO depth and the Ra number (Fig. 3.1B,C,D). For about 50% of its lifetime, the magma ocean has a depth equal to or smaller than 50 km for the Ref-A case. The adiabat intersection with the rheology front at the two pressure depths where switches in the parameterization of the melting curves occur (see Sections 2.3.1 and 2.3.1.2), results in equal characteristic jumps in MO evolution. The decrease in cooling flux is independent of the decrease in depth D , since D is explicitly overwritten when using the soft turbulence parameterization (see Eqs. 2.1 and 2.25). Nevertheless, D defines the average viscosity within the convecting domain, which enters the Ra calculation (Eq. 2.1). Ra is ultimately responsible for the decrease in heat flux.

The role of radioactive decay as energy source in the MO evolution of an Earth-sized planet is insignificant (Fig. 3.1C), unless the planet is formed within few Myr, which includes the contribution of the short-lived elements ^{26}Al and ^{60}Fe . This becomes comparable to the long-lived element contribution after 9 Myr and insignificant to the MO evolution by 7 Myr after CAI formation, in agreement with Elkins-Tanton (2012) findings.

Comparing the two atmospheric approaches, I find that the pure water vapor grey approximation underestimates the thermal blanketing in comparison to the lbl model because of the low absorption coefficient used to represent the whole thermal radiation spectra ($k_{0,\text{H}_2\text{O}} = 0.01$). The lbl pure H_2O model resolves better the steam IR absorption, although it overlooks the role of CO_2 .

The “bb-grey-lbl” atmosphere comparison captures the decreasing convective fluxes at the last MO time step as in the “bb-grey-spectrally” resolved atmosphere” comparison of the Lebrun et al. (2013) model. In our approach this is due to the decrease in temperature difference and in Ra towards the MO end. However, upon evaluation at the last time step before solidification the Ra drop to 10^{10} is not seen in their work (where $Ra = 10^{14} = \text{const}$), likely due to differing average viscosity calculation and spatial resolution.

On a technical note, a Ra overshoot towards lower values is observed near the end of the magma ocean phase (Fig. 3.1D). Consequently, the switch to solid occurs abruptly from $Ra = 10^{10}$ to 10^{12} , two orders of magnitude higher than the value obtained during convection of the last 1-km-deep liquid-like layer of magma ocean. This is a numerical artifact that correlates with high radial resolution of the model layers (≈ 1 km). Therefore, care should be taken when using convective heat flux parameterizations with high spatial resolution very close to the critical melt fraction, because the rheology becomes more complex at high crystal values.

The evolution of ΔT , u_{conv} convective velocity, F_{conv} and Nu as a function of Ra during the MO gives an informative overview of the regimes expected during the MO (Figure 3.2). The evolution of T_{surf}

due to the role of the coupled radiative atmosphere prescribes a new ΔT on the system at each time step. The thermal buoyancy forcing re-defines the adimensional numbers either directly ($Ra=f(\Delta T)$) or indirectly through the viscosity dependence on temperature ($Pr=f(\nu(T))$).

The $Ra - Pr$ conditions reproduced in numerical experiments or in laboratory experiments and published in literature (Niemela et al., 2000b; Grossmann et al., 2011; Davaille et al., 2011; Shishkina et al., 2016; Blass et al., 2019) are plotted for comparison to the obtained from the MO simulations (Fig. 3.3). The evolution of Ra and Pr reveal the distance of the MO regime to the experimentally evaluated thermal convection regimes.

3.2 OUTGASSING AND ATMOSPHERIC BUILD UP

3.2.1 Mantle solidification and outgassing overview

The assumption of greenhouse gases H_2O and CO_2 as major species is in accordance with an oxidized MO surface (Hirschmann, 2012; H. L. Zhang et al., 2017) and bulk silicate Earth (Lupu et al., 2014).

As far as the volatile solubility is concerned, molten silicate is a poor CO_2 solvent. The melt is oversaturated with respect to CO_2 at Ref-A conditions (Fig. 3.4.B). Consequently, the mantle operates as a “ CO_2 -pump” into the atmosphere. In contrast, H_2O is highly soluble in the silicate melt (Fig. 3.4.A) and does not leave the mantle until the latest stage of the magma ocean, where the enrichment in the melt peaks. The evolving atmospheric composition reflects those features as it transitions from a CO_2 -dominated to a H_2O -rich one (Fig. 3.5). The major release of the water vapor, from 2.5 to 220 bar, occurs when the total melt fraction of the mantle reduces from 30% to 2% or as the potential temperature drops from ~ 2200 to ~ 1650 K (Fig. 3.6). This effect is the basis for the so-called “catastrophic” outgassing of a steam atmosphere (e.g. Lammer et al., 2013). It reflects the progressive replacement of melt mantle volume with solid mantle volume that has small volatile storage capacity.

In addition, the choice of melting curves defines the degree of melting throughout the magma ocean lifetime, and similarly affects the accompanying outgassing process. I find that over the T_p range 3000–2200 K the melt fraction differs by 10–43% at the same potential temperature, comparing chondritic and peridotitic composition for the lower mantle (Fig. 3.6). The choice of lower mantle melting curves does not affect the final outgassing but modifies the onset of catastrophic outgassing by maximum 5% of the total volatile volume. Therefore, chondritic composition for the lower mantle disfavors early water release for a cooling magma ocean for potential temperatures above 2200 K.

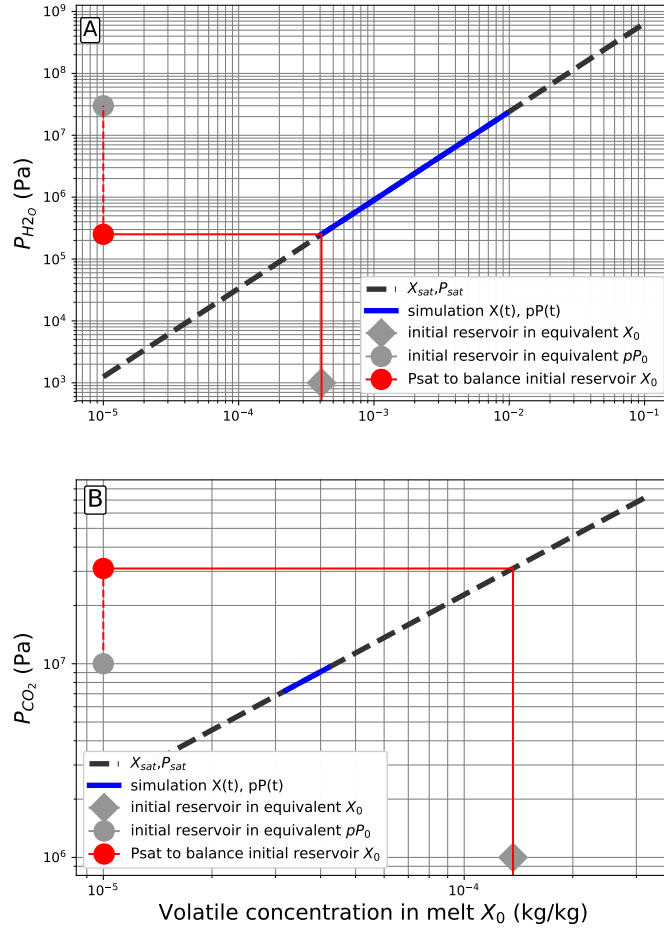


Figure 3.4: P_{sat} and X_{sat} solubility expressions for volatiles **A:** H_2O and **B:** CO_2 . Comparison between oversaturated (CO_2) and undersaturated (H_2O) initial conditions. Ref-A total reservoirs are expressed in equivalent vapor pressure (grey circle) and equivalent concentration in silicate melt (grey diamond). The latter is matched (red line) to the corresponding pressure that satisfies saturation (red circle). Comparison between the reservoir-equivalent pressure and the vapor pressures required to satisfy saturation reveal if the volatile is supersaturated or undersaturated in the silicate melt.

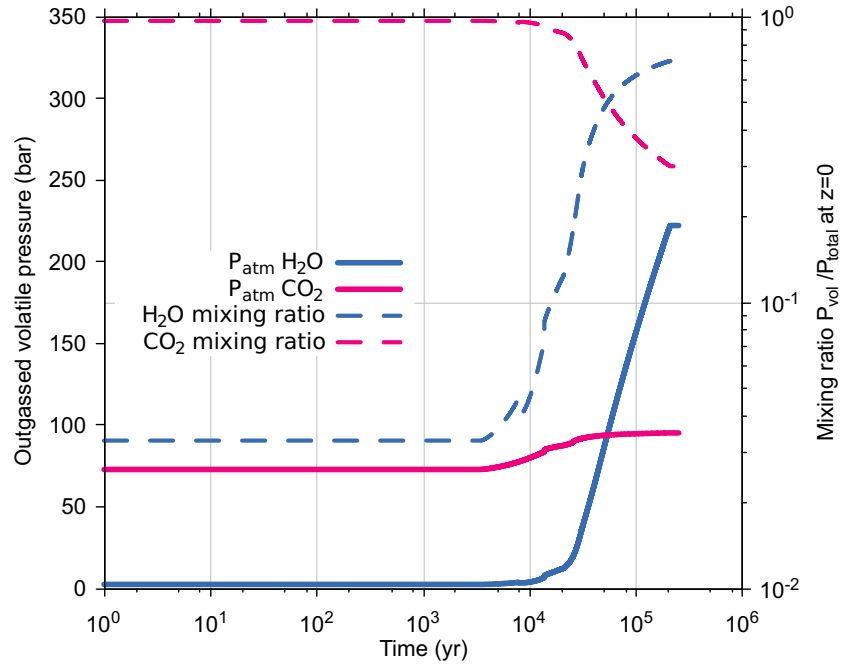


Figure 3.5: Figure adapted from (Nikolaou et al., 2019) © AAS. Reused with permission. Evolution of H₂O and CO₂ outgassing based on the Ref-A case (see Table 2.4). Absolute quantity of outgassed volatile in the atmosphere (solid lines) and relative mixing ratio at the surface (dashed lines) are shown.

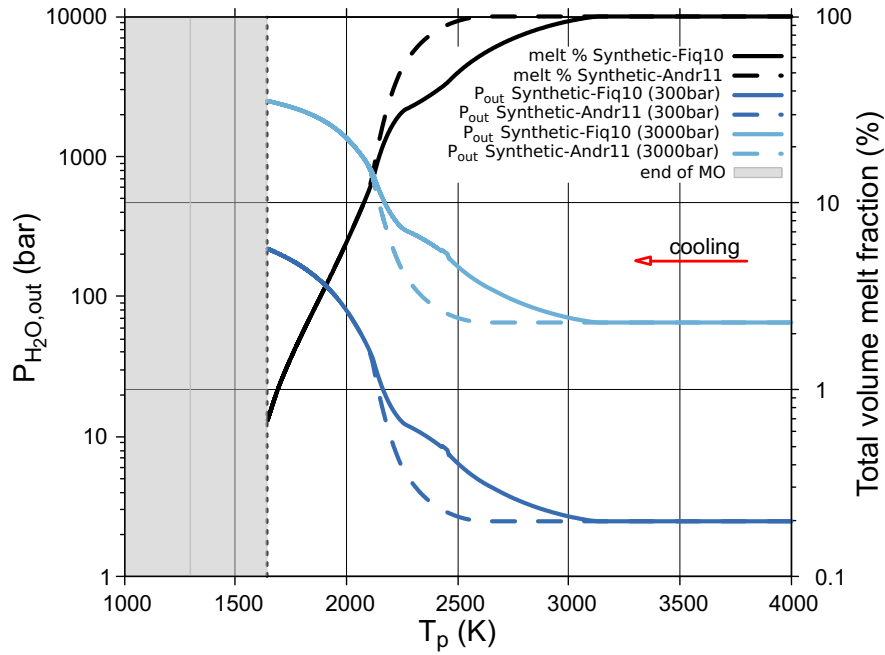


Figure 3.6: Figure from Nikolaou et al. (2019) © AAS. Reproduced with permission. Effect of melting curves on the variation in mantle melt fraction with potential temperature. The magma ocean end occurs at 99.3% solidification (grey shaded area). Two sets of melting curves are compared: “Synthetic-Fiq10” (dashed lines) and “Synthetic-Andr11” (solid lines) that share the Herzberg et al. (2000), Hirschmann (2000) and J. Zhang et al. (1994) parameterization for the upper mantle and use the Fiquet et al. (2010) or the Andraut et al. (2011) parameterization for the lower mantle respectively. Different volatile inventories: 300 bar (dark blue lines; Ref-A) and 3000 bar (light-blue) are shown for comparison. The global melt fraction for each case is shown in black color.

3.2.2 Effect on relative outgassing with varying total volatile reservoirs

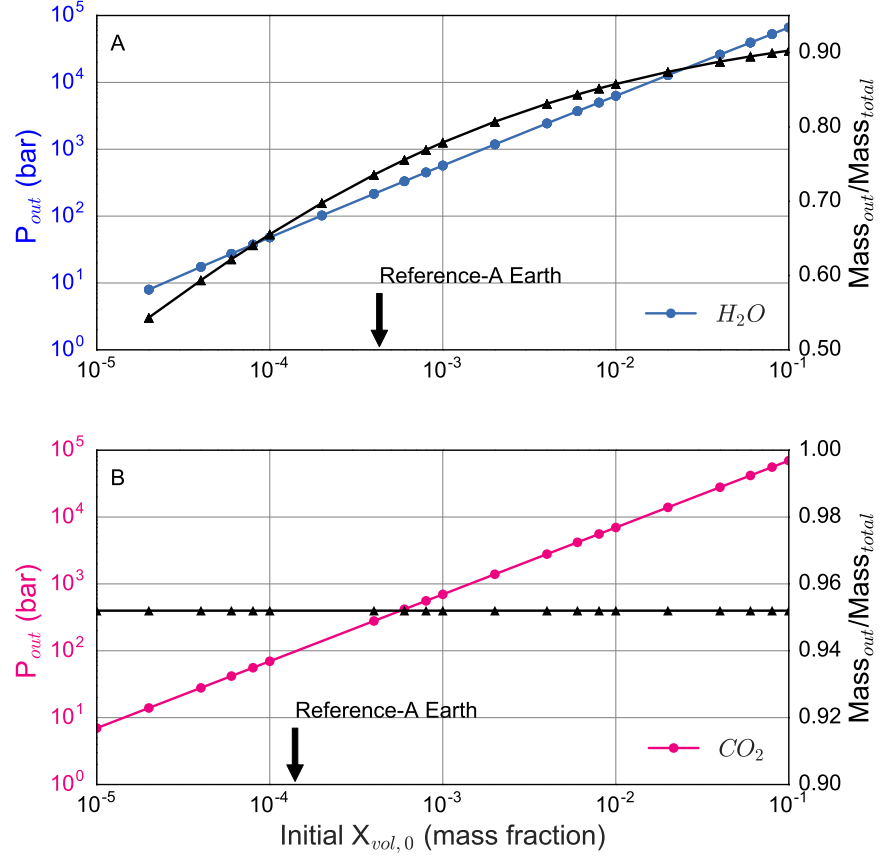


Figure 3.7: Figure from Nikolaou et al. (2019) © AAS. Reproduced with permission. Estimates of maximum outgassing at the magma ocean end (99.3% solid), depending on initial bulk abundance for volatiles H_2O and CO_2 . **A:** The absolute amount of H_2O outgassed by the end of the magma ocean (colored line, left y-axis) is plotted against the initial concentrations in the mantle. The mass of outgassed volatile relative to the mass of the total volatile reservoir is plotted on the right axis (black line, right y-axis). **B:** Same as in panel A but for the CO_2 volatile. The performed experiments are plotted with points.

Simultaneous to the final outgassed quantity, I also calculate the relative volatile inventory extracted from the mantle assuming different initial concentrations (Fig. 3.7). As expected, the higher initial concentration results in higher outgassing. However, the relative quantity varies as follows: I find that [45%, 10%] of the initial water reservoir remains in the mantle for the examined range $X \in [10^{-5}, 10^{-1}]$ respectively, while the rest [55%, 90%] is in the atmosphere. This suggests

that the lower the initial mantle abundance, the larger is the relative amount of water stored in the planet's interior after the magma ocean ends. By contrast, only $\approx 6\%$ of CO_2 remains in the mantle for an Earth-sized planet independently of the initial concentration assumed.

3.2.3 Partial pressure in a binary gas mixture

Due to the existence of two gas species the partial pressure in the atmosphere differs to that of pure species (Pierrehumbert, 2010). This is known as Dalton's law of partial pressures. The reason is that the average molecular weight is modified according to the presence of other gases and the intra-species molecular collisions have to be calculated in the kinetic energy. I examine the change in a binary gas mixture for the two gases H_2O and CO_2 by post processing the Ref-A results.

The laws are:

$$p_{\text{H}_2\text{O},A} + p_{\text{CO}_2,A} = p_{\text{TOT}} \quad (3.1)$$

The mass of each volatile is:

$$m_{\text{H}_2\text{O}} = \frac{p_{\text{H}_2\text{O},A}}{4\pi R_p^2} \quad (3.2)$$

$$m_{\text{CO}_2} = \frac{p_{\text{CO}_2,A}}{4\pi R_p^2} \quad (3.3)$$

The molecular weight of each species (in atomic mass units) is:

$$MB_{\text{H}_2\text{O}} = 1 + 1 + 16 = 18 \text{ amu}$$

$$MB_{\text{CO}_2} = 12 + 16 + 16 = 44 \text{ amu}$$

Mols of each substance are:

$$n_{\text{H}_2\text{O}} = \frac{m_{\text{H}_2\text{O}}}{MB_{\text{H}_2\text{O}}} \quad (3.4)$$

$$n_{\text{CO}_2} = \frac{m_{\text{CO}_2}}{MB_{\text{CO}_2}} \quad (3.5)$$

The mean molecular weight of the atmosphere based on the outgassed volatile masses is:

$$\langle MB \rangle = \frac{(m_{\text{H}_2\text{O}} MB_{\text{H}_2\text{O}} + m_{\text{CO}_2} MB_{\text{CO}_2})}{(m_{\text{H}_2\text{O}} + m_{\text{CO}_2})} \quad (3.6)$$

Updated partial pressures in binary gas mixture:

$$p_{H_2O,binary} = \frac{m_{H_2O}g}{4\pi R_p^2} \frac{MB_{H_2O}}{\langle MB \rangle} \quad (3.7)$$

$$p_{CO_2,binary} = \frac{m_{CO_2}g}{4\pi R_p^2} \frac{MB_{CO_2}}{\langle MB \rangle} \quad (3.8)$$

Figure 3.8.A shows the difference in pressures for the same molar mass outgassed while considering the presence of the other gas and while ignoring it. The binary pressures reveal that the switch from a CO₂-dominated to H₂O-dominated atmosphere that occurs during Ref-A simulation is not attained in the binary gas mixture case of partial pressures calculated using equations (3.7),(3.8). The reason is the high molecular weight of the CO₂ that compensates the outgassed mass of the light weight water. However, the switch of atmospheric quality is expected to occur at simulations where the molar inventory of H₂O is higher than that of Ref-A.

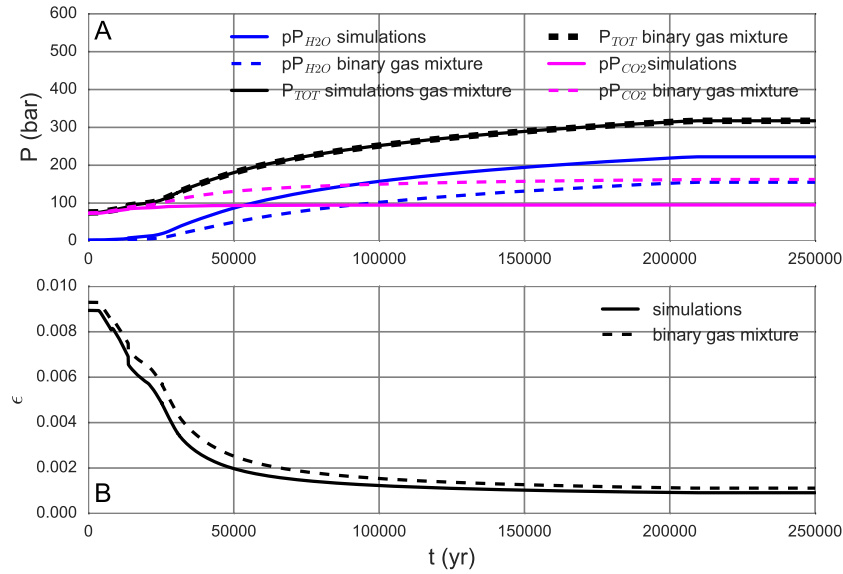


Figure 3.8: (A) Partial pressures of gas species assuming a binary gas mixture of H₂O, CO₂ at Ref-A setting. (B) Change in grey emissivity with partial pressures compared for single and binary gas mixtures. The ϵ change assuming Ref-A abundances is negligible.)

The partial pressure enters the emissivity calculation which controls the thermal evolution through the energy balance equation. The Dalton-modified partial pressures of a binary mixture are shown in Figure 3.8.B. The effect of the updated partial pressures on the atmospheric opacity for the Ref-A scenario is negligible. Specifically,

the Dalton case results in 0.1–2 fold higher emissivity than the Ref-A throughout the evolution. The atmosphere in the binary mixture case has higher emissivity and it thermally radiates more efficiently toward space. The reason lies in the constants employed for each species' absorptivity (see Table 2.3). The role of CO₂ in the absorption spectra over the heat emitting MO is secondary to that of H₂O based on the absorption coefficients. Consequently, despite increased CO₂ partial pressure in comparison to Ref-A P_{CO₂} simulation, the effect of H₂O prevails. The expected acceleration in the system cooling is not significant. The Ref-A solidification times remain maximum with regard to the binary gas mixture case. The effect on solidification times is expected to become significant at simulations where the molar inventory of CO₂ is much higher than that of water. Such inventory combination is, however, not likely.

In general, note that any partial pressure calculation is relative to the atmospheric inventory that precedes the outgassing. This is not exhausted in the H₂O and CO₂ species but could include gases without greenhouse potential, which however modify the mean molecular ratio in the atmosphere. Such are Nitrogen (2-fold present atmospheric level according to Goldblatt et al. (2013)), as well as species captured from the circumstellar nebula (e.g.: CO, H, He, Ar) which are not taken into account in lack of an accretion model to provide such IC for the MO. Moreover, chemical interactions between the gas compounds in the atmosphere and the magma modify the amount of volatiles that is in molecular form at equilibrium, on which the partial pressure is based.

Consequently, the problem of partial pressure calculation in multi-species gas mixtures is degenerate. For simplicity, I assess H₂O, CO₂ as single gases whose solubility is covered by the available expressions and I ignore the chemical interactions among them as well as capture of gases. The resulting mixing ratios are indicative of atmospheric mixtures where the remaining species constitute trace gases.

3.3 EFFECTS OF MODEL PARAMETERS ON THE MO LIFETIME

The combined H₂O/CO₂ inventory was found to delay the MO termination in prior works (e.g. Zahnle et al., 1988; Abe, 1997; Lebrun et al., 2013). The Elkins-Tanton (2008) work considers different MO depths (2000km, 1000km, 500km) than our global MO for Earth (2890 km). Consequently, the volatile masses differ for the same assumed concentration and a direct comparison is not possible. Recently, Salvador et al. (2017) have studied the effect of water abundances on the global MO solidification time yielding longer durations likely due to the use of a non-grey atmospheric model.

In our study I quantify the solidification time (t_s) by sampling a larger domain of initial abundances for the two species and assum-

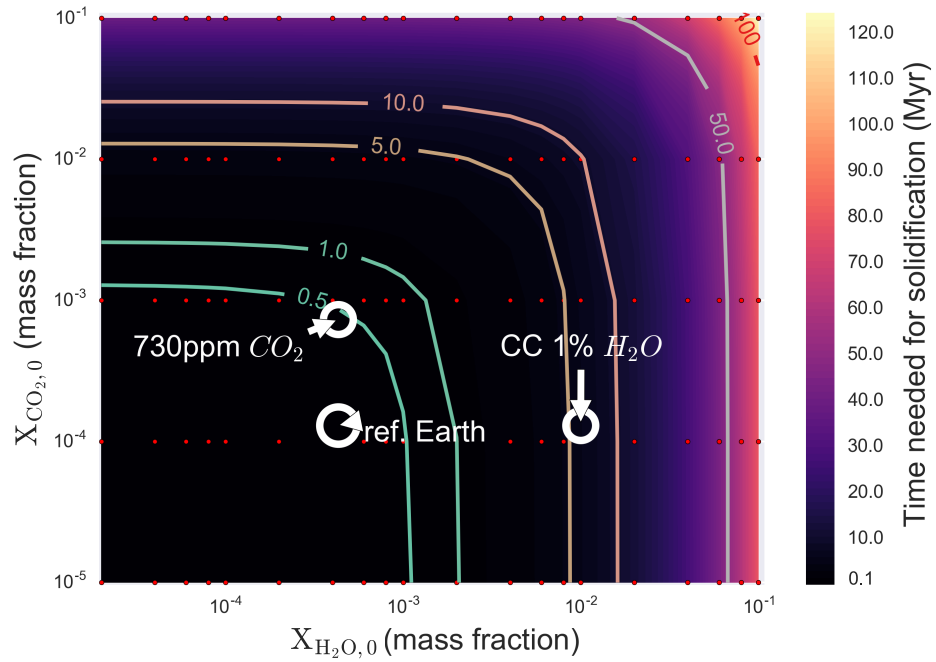


Figure 3.9: Figure from Nikolaou et al. (2019) © AAS. Reproduced with permission. Colormap of solidification time for varying initial H_2O and CO_2 abundances in the mantle, expressed in initial concentrations $X_{\text{volatile},0}$ (at model time 0). **Open circles** annotate: CC 1 wt% H_2O -abundance, estimated terrestrial CO_2 abundance 730 ppm by Marchi et al. (2016), and the abundances used in the Ref-A scenario. Red points correspond to the model experiments carried out. **Isolines** of t_s : 0.5, 1, 5, 10, 50 and 100 Myr are plotted for reference.

ing a grey atmosphere (Fig. 3.9). The MO duration amounts to ≈ 0.21 Myr for conservative Earth volatile abundances while it would reach 5-10 Myr for an (unlikely) Earth-sized planet made entirely out of carbonaceous chondritic (CC) material with 1 wt% of H_2O . Our results confirm that the atmosphere is the most important solidification delaying factor.

However the effect of each separate interior process on the duration of the magma ocean stage remains difficult to disentangle and it would help clarify future modeling priorities. In Table 3.1 I present an overview of the effect of additional factors and parameters on the MO solidification time (t_s). Each t_s is obtained through varying parameters and/or including a different process (first column). The second column states the number of parameters (three at most) that have been modified in each experiment with respect to a reference case. The third column gives the details on the experiment changes with respect to the reference case. I calculate the solidification time (t_s , fourth column), as well as the absolute (Δt_s , fifth column) and relative

difference ($\Delta t_s / t_{s,ref}$, sixth column) with respect to the solidification times ($t_{s,ref}$) obtained during two reference simulations: Ref-A (Table 2.4) and Ref-B. The latter uses the same parameters as the Ref-A settings but does not include CO₂. I thus obtain the tendency of each factor to increase or decrease the solidification time (“+” or “−” sign respectively) as well as its magnitude. Below I discuss only the most crucial contributions.

When accounting for the water dependence of the melt viscosity in experiment 3 I expect a shorter solidification time, that reflects the more efficient convection due to lower viscosity. η_l decreases due to progressive enrichment of water concentration in the melt during the MO evolution, from 410 ppm to $\approx 10,000$ ppm (Fig. 3.4.A; Ref-A). The atmospheric radiative forcing remains identical to the Ref-A case. The expected cooling acceleration is counteracted by the delaying role of the outgassed vapor atmosphere (experiment 3), even so for particularly water-rich settings (as seen by the almost identical t_s of water-rich experiments 1b and 3b). The effect of viscosity on t_s becomes evident in the BB cases (experiments 11, 12). With respect to the BB case of experiment 11 ($t_s = 2000$ yr) that uses constant 10 wt% water content (Karki et al. (2010)), I observe an increase in the solidification time ($t_s = 2713$ yr) in experiment 12b that uses water dependent viscosity. This is explained by the fact that in experiment 12b, the 10 wt% water enrichment is attained only at the final MO time step and not throughout the whole run. Our parameterizations show that one order of magnitude enrichment in H₂O in the melt causes a decrease of up to two orders of magnitude in the viscosity (Fig. 2.5). This becomes important at lower melting temperatures $T_{RF,0} < 1400$ K which correspond to evolved silicate melts (Parfitt et al., 2008). Experiments 12a and 12b confirm the tendency I hypothesized for the viscosity role in decreasing t_s assuming increased water content (410 ppm and 10,000 ppm respectively). Therefore the water-enriched melt accelerates the solidification process and it should be taken into account for evolved surface compositions or planets around EUV and XUV active host stars that lose their atmospheres. According to Abe (1997) low viscosity enhances the differentiation of minerals. Therefore, such a η_l parameterization is also vital in better modeling the mineral solidification sequence.

Using the hard turbulence approximation for the convective flux rather than the soft approximation yields a slight increase in the solidification time (experiment 5). The abrupt decrease of ≈ 1000 K in the surface temperature at the MO termination is reduced by up to 300 K by employing the hard turbulence parameterization. During this, the Pr number is updated according to the evolution of the liquid viscosity and the flow aspect ratio (λ) takes values between 1 and 2. Significant work that has been done in this direction shows numerical proof of the hard turbulence regime (Grossmann et al., 2011) and

Table 3.1: Overview of the effects of various parameters on the solidification time. Different scenarios are compared to a reference case. The scenarios consist of varying or replacing a parameter or physical process as indicated in the first column. The total number of changed parameters (three at most) with respect to the reference scenario is indicated in the second column. The employed parameter values and/or the description of the process are in the third column. The fourth column shows the solidification time t_s , and the fifth and sixth columns the absolute and relative difference of t_s with respect to the reference cases A or B.

Modified parameter	#	Value / Description	t_s (yr)	Δt_s (yr)	$\Delta t_s / t_{s,ref}$
Reference-A					
1a: H ₂ O content	1	As in Table 2.4 $X_{H_2O,0} = 10$ ppm	208,600	–	–
1b:	1	$X_{H_2O,0} = 10^5$ ppm	58,900	–149,700	–72%
2a: CO ₂ content	1	$X_{CO_2,0} = 10$ ppm	69,699,000	+69,490,400	+33000%
2b:	1	$X_{CO_2,0} = 10^5$ ppm	160,500	–48,100	–23%
3a: Liquid viscosity	1	$\eta_l = f(T, X_{H_2O})$	3,919,000	+3,710,400	+18000%
3b:	2	$\eta_l = f(T, X_{H_2O}), X_{H_2O,0} = 10^5$ ppm	213,400	+4,800	+2%
4a: Radioactive sources	1	$t_{planet} = 100$ Myr	69,711,000	+69,502,400	+33000%
4b:	2	$t_{planet} = 2$ Myr	208,600	0	0%
5:	1	Heat flux parametrization $F_{hard}/F_{max} = 1$	6,036,780	+5,828,180	+2793%
6a: Upper mantle solidus	1	$T_{sol} - 20$ K $\Rightarrow T_{RF,0} = 1625$ K	260,770	+52,170	+25%
6b:	1	$T_{sol} - 50$ K $\Rightarrow T_{RF,0} = 1595$ K	216,400	+7,800	+4%
6c:	1	$T_{sol} - 100$ K $\Rightarrow T_{RF,0} = 1545$ K	228,700	+20,100	+10%
6d:	1	$T_{sol} - 400$ K $\Rightarrow T_{RF,0} = 1245$ K	250,600	+42,000	+20%
7:	2	Lower mantle melting curves $T_{sol/liq}^*$ (Andraut et al., 2011)	434,600	+226,000	+108%
8:	2	Alternative melting curves $T_{sol/liq}^*$ Linear (2.3.1.2) $\Rightarrow T_{RF,0} = 1360$ K	207,100	–1,500	–1%
9: Irradiation	1	72% S_0	126,670	–81,930	–39%
10a: Irradiation & albedo	2	$S_0, \alpha = 0.15$	208,500	–100	0%
10b:	2	72% $S_0, \alpha = 0.60$	208,600	0	0%
11: No atmosphere & $\eta_l(T)$	1	No atmosphere	208,500	–100	0%
12a: No atmosphere & $\eta_l(T, X_{H_2O})$	2	No atmosphere, $X_{H_2O,0} = 410$ ppm	2,000	–206,600	–99%
12b: No atmosphere & $\eta_l(T, X_{H_2O})$	3	No atmosphere, $X_{H_2O,0} = 10^4$ ppm	2,958	–205,642	–99%
13:	3	No atmosphere, $X_{H_2O,0} = 10^4$ ppm	2,713	–205,887	–99%
Reference-B					
13: Lbl atmosphere	–	As Reference-A with $X_{CO_2,0} = 0$	156,700	–	–
	1	Steam lbl	736,100	+579,400	+278%

suggests that it could affect the thermal transport controlled by the boundary layers (Grossmann et al., 2003; Lohse et al., 2003).

In experiment 6 I examine the role of uncertainty in the upper mantle's (0 – 22.5 GPa) solidus. The ± 20 K error in the solidus expression of Herzberg et al. (2000) has a measurable impact (+4%) on the solidification time. The mere uncertainty in the experimental data can thus affect the magma ocean solidification time by a few thousands of years.

Further decreasing the upper mantle solidus by 50, 100 and 400 K causes the solidification time to decrease by 10, 20 and 108% respectively. Compositions more silicate-evolved compared to the KLB-1 peridotite have such lower melting temperatures. The -400 K value corresponds to rhyolite (Parfitt et al., 2008). Lebrun et al. and Salvador et al. (2017) previously acknowledged that the chemical composition of the magma ocean at its latest stages would be a decisive factor in the evolution. Schaefer et al. (2016) and Wordsworth et al. (2018) further resolved the chemical evolution for specific compositions. Our result emphasizes the controlling role of the surface melting temperature in the solidification duration and reveals a linear dependence between them.

The solidification time is however insensitive to changes in the lower mantle melting curves (experiment 7) as long as bottom-up solidification is ensured. The reason is that they affect neither the amount of CO_2 in the atmosphere, the majority of which is degassed at the beginning of the magma ocean phase, nor the water enrichment which does not occur at high MO depths.

In experiment 8 I test the effect of linearizing the melting curves of Abe (1997), where the solidification time decreases significantly (-39%). The higher melt fraction preserved at the end of the magma ocean is tied to lower final outgassing, which explains the difference to the Ref-A setting. Lebrun et al. (2013) has previously discussed a similar effect of the curve linearisation. A quantitative comparison is however inconclusive due to the different atmospheres used.

QUALITATIVE PATHS IN THE MO THERMAL EVOLUTION - RESULTS

Below I show the results based on the coupling of the [COMRAD](#) model with the non-grey, [lbl](#) radiative transfer atmosphere to answer the research question:

- Q4 How does [MO](#) evolve with distance from the host star and how is it affected by planetary composition?

This Chapter focuses on the magma ocean net cooling/warming limits found with the [lbl](#) radiative transfer atmospheric absorption treatment, which will hereafter be referred to as “[lbl-atmosphere](#)” or “[lbl-approach](#)” for brevity.

4.1 QUALITATIVE DIFFERENCE BETWEEN GREY AND LINE-BY-LINE RADIATIVE TRANSFER ATMOSPHERIC REPRESENTATION

I firstly clarify a fundamental difference between the atmospheric approaches that were implemented in this work. I illustrate this by assuming a high ($F_{Sun}(S = 1361 \text{ W/m}^2, \alpha = 0.11) = 303 \text{ W/m}^2$) and a low ($F_{Sun}(S = 1361 \text{ W/m}^2, \alpha = 0.30) = 238 \text{ W/m}^2$) incoming solar radiation (Fig. 4.1). The difference is only in the assumed albedo value, 0.11 or 0.30.

In the [lbl](#) approach (Fig. 4.1.A, B), the colormap combinations of P_{H_2O} and T_{surf} lead to planetary cooling. In the high F_{Sun} case, for each value of the surface temperature T_{surf} between 700 and ≈ 1700 K there exists a threshold value of outgassed water P_{H_2O} across which the net radiation balance at [TOA](#) is negative and the planet warms. This effect is absent in the low F_{Sun} case, which yields a cooling regime for all combinations of P_{H_2O} and T_{surf} . On the contrary, the grey approach shows a negligible difference of the magma ocean cooling flux of the order of 10^{-1} W/m^2 , accounting for the T_{eq} of our solar system’s inner planet orbits (Fig. 4.1.C). In fact the grey atmosphere is insensitive to variations in the incoming stellar radiation. The reason is that in the grey energy balance (Eq. 2.39), the incoming solar flux enters only in the calculation of equilibrium temperature (T_{eq}). The latter does not vary more than a factor of 2 over the insolation range in our solar system history ($T_{eq} = 144 \text{ K}$ for the young Sun case and $T_{eq} = 256 \text{ K}$ for today’s Sun at 1 AU, assuming albedo 0.30). The fourth power of T_{eq} has a minor contribution compared to the fourth power of the surface temperature of the magma ocean, which is higher than $T_{RF,0} = 1645 \text{ K}$ (Ref-A) throughout the evolution.

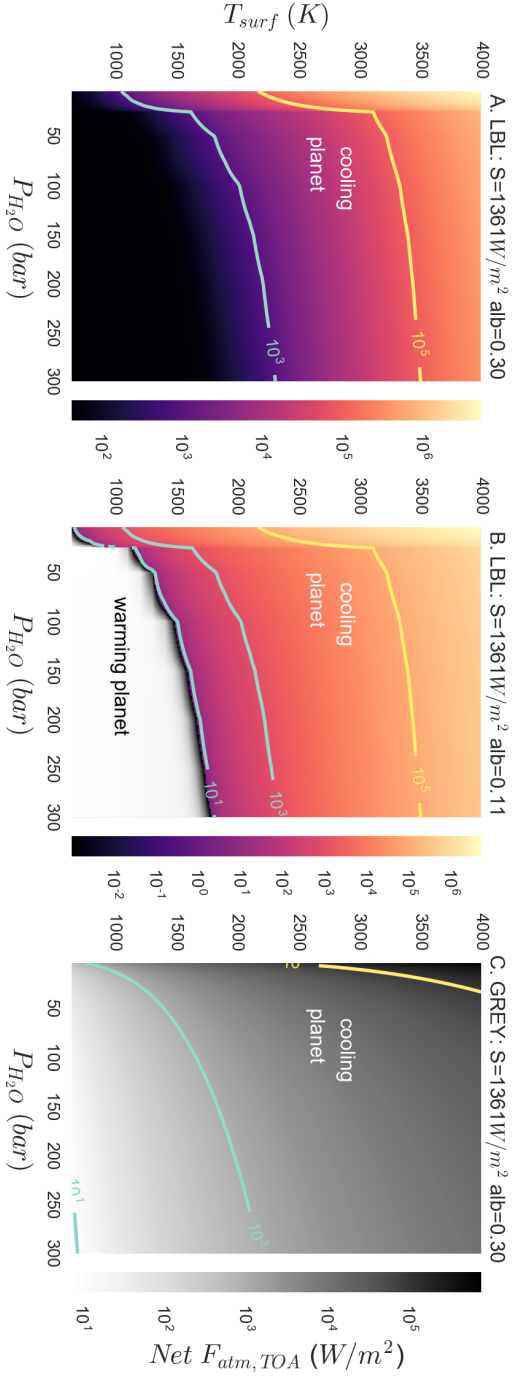


Figure 4.1: Figure from Nikolaou et al. (2019) © AAS. Reproduced with permission. Net outgoing radiation flux at TOA for (P_{H_2O} , T_{surf}) calculated for two specific incoming solar radiations (F_{Sun} ($S = 1361 W/m^2$, $\alpha = 0.11$) = $303 W/m^2$ and F_{Sun} ($S = 1361 W/m^2$, $\alpha = 0.30$) = $238 W/m^2$) employing **A**, **B**: the [lbl](#) approach of Katyal et al. (2019) and **C**: the grey approach of Abe et al. (1985) as used in Elkins-Tanton (2008). In all three plots only the net cooling $F_{atm, TOA}$ (positive sign convention) is shown in the colored legend. The grey approach results exclusively in cooling fluxes for both cases examined.

In the limit of the convecting magma ocean model, I only explore cooling regimes and obtain the relevant solidification times. The convective cooling flux out of the magma ocean F_{conv} requires $T_{surf} < T_p$ to ensure the necessary gravitational instability for convection to occur (see Eq. (2.25)). However, if the flux at TOA becomes negative (RHS of Eq. (2.41)) the system would warm and result in $T_{surf} > T_p$, a condition which describes a stably stratified system. That system will not convect and as such is not covered by the present model (Fig. 2.8).

The remaining three Sections 4.2–4.3.1 focus on the cooling/warming limit found with the [lbi](#) atmosphere.

4.2 SEPARATING CONTINUOUS FROM TRANSIENT MAGMA OCEANS

The lifetime of a magma ocean with a steam atmosphere is controlled by the longwave radiation through its steam layer, the energy received from the star, and the melting temperature of the mantle at its surface. All above factors combine into a comprehensive mechanism that distinguishes between a “transient” (or “short-term”, or “type-I” after Hamano et al. (2013)) and “continuous” (or “long-term”, or “type-II” after Hamano et al. (2013)) MO evolution path. Goldblatt (2015) and Ikoma et al. (2018) have discussed the warming/cooling distinction, always in relation to the constant radiation limit for the runaway greenhouse (RG) $\approx 300 \text{ W/m}^2$. I exemplify this idea with an emphasis on the additional role of $T_{RF,0}$.

I use two simulations that are subject to different insolation conditions, namely $F_{Sun,low} = 238 \text{ W/m}^2$ and $F_{Sun,high} = 563 \text{ W/m}^2$ (Fig. 4.2a black solid line and black dashed line respectively), leaving all other parameters unchanged. The $F_{Sun,high}$ is obtained using $S = 2648 \text{ W/m}^2$ that corresponds to the incident radiation at the orbital distance of Venus for today’s Sun and $\alpha=0.15$, while the $F_{Sun,low}$ is equal to the incoming radiation at Earth orbit today. Since F_{Sun} is independent of T_{surf} , it is plotted as a line parallel to the T_{surf} axis (Fig. 4.2a). Both simulations have the same water reservoir (405 bar or 550 ppm initial concentration) to ensure outgassing of 1 Earth ocean (300 bar) at the end of the magma ocean stage. OLR_{TOA} as a function of T_{surf} is plotted for three values of atmospheric water content (4, 100, and 300 bar), which we term “isovolatiles” (grey lines). F_{Sun} intersects with each isovolatile over a temperature value T'_{surf} . The cooling flux F_{conv} (read on the right axis) becomes zero for that specific water content and the planet ceases to cool. If T'_{surf} is higher than the mantle rheology front temperature at the surface ($T_{RF,0}$), the steam quantity indicated by the respective isovolatile balances the energy flux from the star and the MO does not solidify.

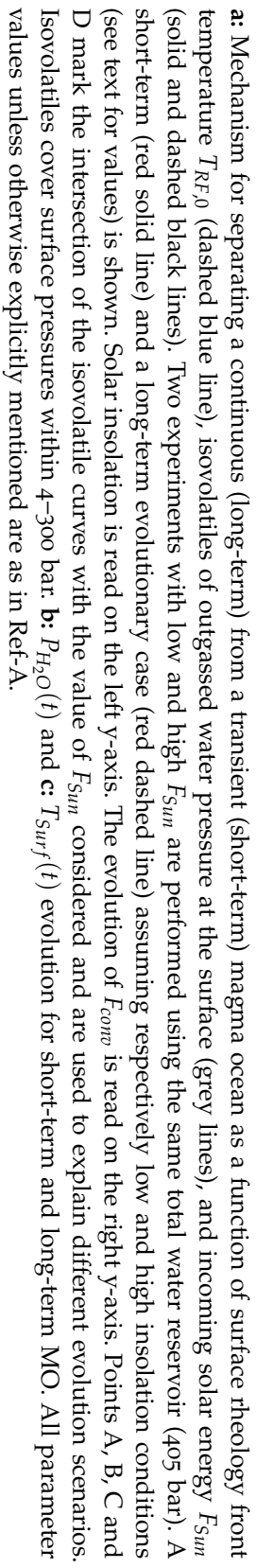
Firstly, we examine the trajectory of the convective flux of the transient magma ocean on the (T_{surf}, F_{conv}) plane as it cools from $T_{surf} =$

3000 K and with an insolation $F_{Sun,low}$ (Fig. 4.2a, red solid line). F_{conv} progressively crosses isovolatiles of higher water content. As it approaches the highest outgassed quantity of 300 bar, the difference $OLR_{TOA} - F_{Sun,low} = F_{conv}$ remains always positive since the 300 bar isovolatile allows the system to dispose of heat at a higher rate than it receives solar radiation. The high convective flux value ensures cooling until $T_{surf} = T_{RF,0}$, which marks the end of the magma ocean. The abrupt cooling after the end of the magma ocean stage and the final outgassing quantity are shown in the evolution of $T_{surf}(t)$ and $P_{H_2O}(t)$ (Fig. 4.2b, 4.2c.)

Secondly, we obtain a long-term magma ocean (Fig. 4.2a, red dashed line) in a scenario that assumes $F_{Sun,high}$. Initially, for high values of T_{surf} , the same amount of water as before is outgassed and its F_{conv} almost coincides with the one of the short-term case (the difference hardly noticeable on the logarithmic graph is $\approx 10^3$ W/m²). During evolution the outgassing proceeds and the simulation trajectory crosses isovolatiles of higher water content. F_{conv} drops to very low values that tend to numerical zero for $T_{surf} = T'_{surf} \approx 1915$ K. The intersection of the incoming radiation $F_{Sun,high}$ with the respective isovolatile over T'_{surf} reflects the steam atmosphere already outgassed when the system ceased to cool. I obtain a point that falls between the isovolatiles of 100 and 300 bar (167 bar read in Fig. 4.2b). Consequently, a continuous magma ocean is maintained at potential temperature $\approx T'_{surf}$ (Fig. 4.2c) due to a specific combination of incoming solar radiation, its intersection with the 167 bar isovolatile, and the solidification temperature (Fig. 4.2a). Note that the long term MO ocean is maintained with less water than one Earth ocean and at an insolation higher than the Runaway Greenhouse state (\neq greenhouse effect) (RG) limit.

The prominent role of $T_{RF,0}$ on the MO type becomes evident when comparing the point (T'_{surf}, P_{H_2O}) where the isovolatiles intersect $F_{Sun,high}$ with $T_{RF,0}$. For the short-term magma ocean the intersection point A occurs well below $T_{RF,0}$. That magma ocean stage will be transient for every possible outgassing scenario within the [4,300] bar range. In the case of the higher solar irradiation, we have intersection points with each isovolatile (B, C, and D), which indicate different thermal evolution paths. On the one hand, the points B and C are located at surface temperatures higher than $T_{RF,0}$, which means that if the MO has outgassed the respective quantities of 300 and 100 bar by the time T'_{surf} is reached, it will cease cooling. On the other hand, the point D corresponds to a much lower temperature than $T_{RF,0}$, which means that a steam atmosphere of 4 bars under those insolation conditions can counteract the cooling process only if T_{surf} decreases to 900 K. The respective magma ocean stage is transient, since it solidifies at a much higher temperature (i.e. 1645 K). The variation of the OLR as a

function of P,T is explored in detail in the companion work of Katyal et al. (2019).



a: Mechanism for separating a continuous (long-term) from a transient (short-term) magma ocean as a function of surface rheology front temperature $T_{RF,0}$ (dashed blue line), isolvolatiles of outgassed water pressure at the surface (grey lines), and incoming solar energy F_{Sun} (solid and dashed black lines). Two experiments with low and high F_{Sun} are performed using the same total water reservoir (405 bar). A short-term (red solid line) and a long-term evolutionary case (red dashed line) assuming respectively low and high insolation conditions (see text for values) is shown. Solar insolation is read on the left y-axis. The evolution of F_{cont} is read on the right y-axis. Points A, B, C and D mark the intersection of the isolvolatile curves with the value of F_{Sun} considered and are used to explain different evolution scenarios. Isolvolatiles cover surface pressures within 4–300 bar. **b:** $P_{H_2O}(t)$ and **c:** $T_{surf}(t)$ evolution for short-term and long-term MO. All parameter values unless otherwise explicitly mentioned are as in Ref-A.

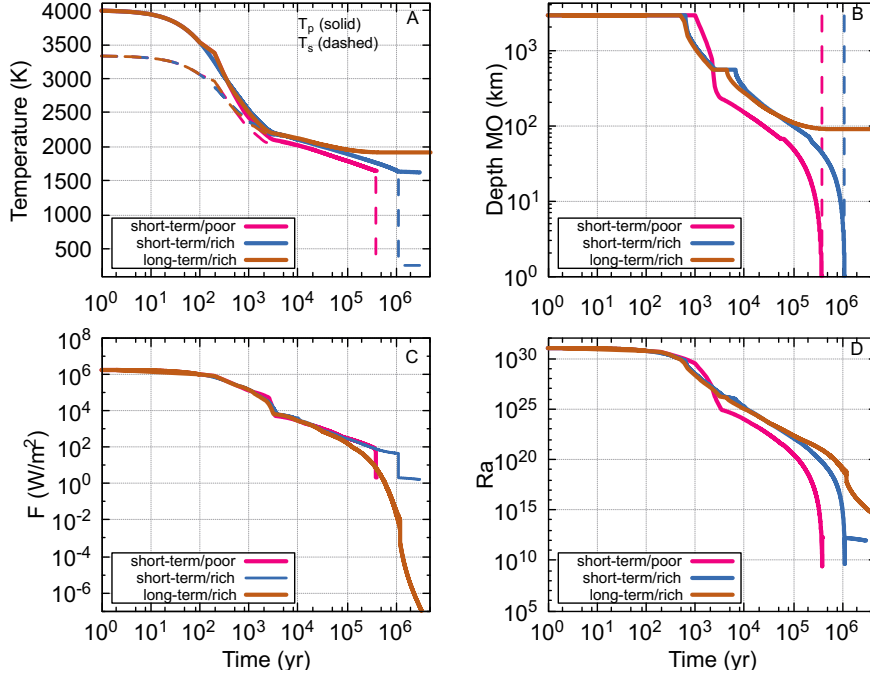


Figure 4.3: **MO** thermal evolution using interior coupling with the **lbl** radiative transfer atmosphere. Insolation intensity and/or initial water content differs from the Ref-A settings. Simulated settings: short-term magma ocean with water reservoir of 200 bar, $F_{Sun} = 238 \text{ W/m}^2$ (magenta lines); short-term magma ocean with water reservoir of 405 bar, $F_{Sun} = 238 \text{ W/m}^2$ (blue lines); long-term magma ocean with water reservoir of 405 bar, $F_{Sun} = 563 \text{ W/m}^2$ (brown lines). All other parameters are as in Ref-A case (Table 2.4). The vertical dashed lines mark the **MO** phase end. Note that such line misses from one scenario (brown line). **A**: Evolution of potential and surface temperature (solid and dashed lines, respectively). **B**: Evolution of the magma ocean depth. **C**: Evolution of the convective flux. **D**: Evolution of Ra .

In the same fashion as Figure 3.1 I examine in Figure 4.3 the **MO** thermal evolution for three different cases of coupling with the **lbl** atmosphere: i) with poor initial water content (200 bar or $X_{H_2O,0} = 270$ ppm) and ii) with higher water abundance (405 bar or $X_{H_2O,0} = 550$ ppm). The incoming solar radiation is the same in both simulations ($F_{Sun} = F_{Sun,low} = 238 \text{ W/m}^2$ corresponding to $S = 1361 \text{ W/m}^2$ and $\alpha = 0.3$). An additional simulation iii) is performed with the richer water content of 550 ppm but subjected to higher insolation conditions. For this case I chose $F_{Sun} = F_{Sun,high} = 563 \text{ W/m}^2$ (obtained using $S = 2648 \text{ W/m}^2$ that corresponds to the incident radiation at the orbital distance of Venus for today's Sun and $\alpha=0.15$). The higher abundance (550 ppm) was deliberately chosen so that the final outgassed quantity is equal to one Earth ocean (Fig. 3.7) (here one Earth ocean is defined equal to 300 bar of water although the value of 270 bar has also been used in the literature (e.g. Tosi et al., 2017)).

Justified by the mechanism here presented, one follows how cases i) and ii) yield transient (short-term) MO while case iii) yields a continuous (long-term) MO.

4.3 ROLE OF ORBITAL DISTANCE AND ALBEDO ON MAGMA OCEAN EVOLUTION

Clearly, the essential quantity regarding the planetary heat budget is F_{Sun} , since it distinguishes the fate of the magma ocean between transient and continuous. Below we refer to this limiting incoming flux as F_{lim} (where $F_{conv}=0$) and we specify the incident solar radiation and albedo combinations which satisfy it.

On combining the stellar luminosity (L_{Star}):

$$L_{Star} = (4\pi R_{Star})^2 \sigma T_{eff,Star}^4, \quad (4.1)$$

where R_{Star} is the stellar radius and $T_{eff,Star}$ the effective temperature at the star's photosphere; with the expression of Gough (1981) for the evolution of solar luminosity we get $T_{eff,Star}(\tau)$. Combining with the blackbody radiation law for the equilibrium temperature of a planet, we obtain the following equation:

$$R = \frac{R_{Star} \cdot T_{eff,Star}^2(\tau) \cdot \sqrt{1 - \alpha_{max}}}{2 \sqrt{\frac{F_{lim}(P_{H_2O}, T_{RF,0})}{\sigma}}}. \quad (4.2)$$

Eq. (4.2) relates with F_{lim} the maximum albedo α_{max} that an Earth-sized planet at orbital distance R from a star of effective temperature $T_{eff,Star}$ can possess, in order to maintain a continuous magma ocean stage. The limiting flux included in the denominator of Eq. (4.2) is not constant but equal to:

$$F_{lim}(P_{H_2O}, T'_{surf}) = \frac{(1 - \alpha_c) S(\tau)_{1AU}}{4}, \quad (4.3)$$

where α_c the critical albedo found with a sensitivity experiment for a given planetary volatile inventory. There $S(\tau)_{1AU}$ is the solar constant at an orbital distance of 1 AU and stellar age τ , P_{H_2O} (in bar) the mass of the water vapor outgassed and T'_{surf} is the temperature over which the stellar insolation crosses the P_{H_2O} isovolatile (Section 4.2). The obtained limiting flux F_{lim} maps to the data product $OLR_{TOA}(T'_{surf}, P_{H_2O})$. Using the Katyal et al. (2019) values of the limiting flux, we compared our Eq. (4.2) with an equivalent expression calculated by Hamano et al. (2013). The solution is similar with minor differences due to the astrophysical properties assumed. I generalise the formulation to cover our Sun or any other host star with a known photospheric temperature T_{eff} and radius.

4.3.1 Dependence of F_{lim} on the melting temperature and steam mass

The irradiation conditions which can pinpoint an Earth-sized planet stalling in a magma ocean stage just above the 40% melting temperature, are extended here to include a range of steam atmosphere masses that span [4,300] bar for two different $T_{RF,0}$ values (the lower melting temperature is representative of a more evolved composition than the KLB-1 peridotite of Ref-A).

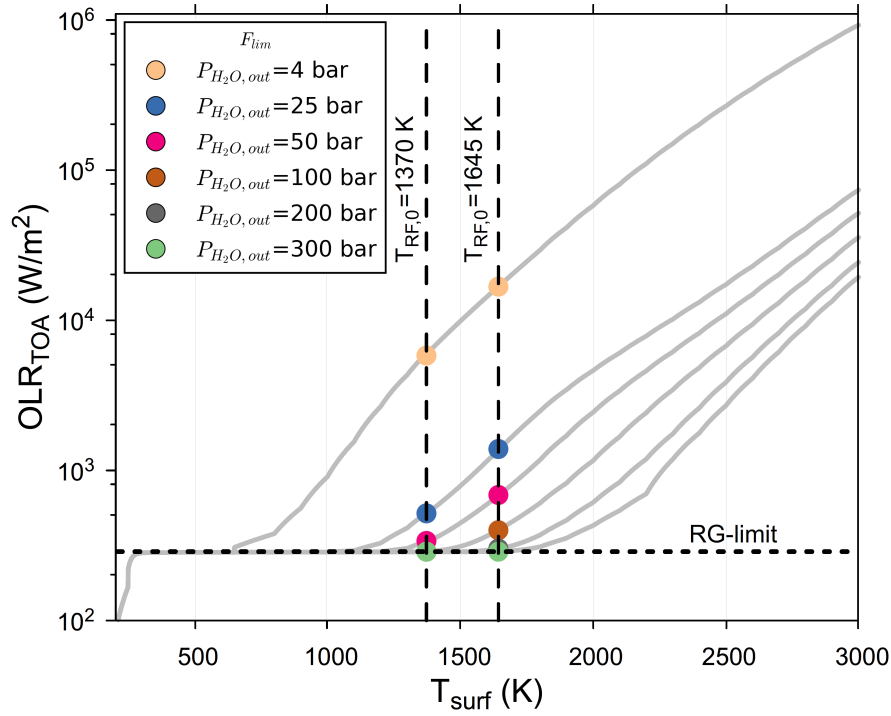


Figure 4.4: Figure from Nikolaou et al. (2019) © AAS. Reproduced with permission. OLR_{TOA} as a function of surface temperature and outgassed water surface pressure 4–300 bar, based on data from Katyal et al. (2019). I consider two different surface solidification temperatures: $T_{RF,0} = 1370$ K as in Hamano et al. (2013) and $T_{RF,0} = 1645$ K as in Ref-A case. Colored points correspond to OLR_{TOA} values obtained for the respective isovolatiles for different outgassed steam atmospheres 4, 25, 50, 100, 200 and 300 bar that overlie magma oceans of different $T_{RF,0}$ (see Table 4.1 for explicit values). Note the variation in temperature coverage of $OLR = \text{const} = 282$ W/m², for different isovolatiles. Data by Nakajima et al. (1992) are used to complement the plot in the region where $T_{surf} \ll T_{H_2O,crit}$.

Different radiative flux limits F_{lim} are obtained for the two values $T_{RF,0} = 1370$ K and 1645 K, depending on the vapor amount (Fig. 4.4). From the superposition of points that correspond to 200 and 300 bar at $T_{RF,0} = 1645$ K in Fig. 4.4, we note the tendency of steam atmospheres exceeding 200 bar to converge to the constant RG limit ($RG = 282$ W/m² Katyal et al. (2019)). For $T_{RF,0} = 1370$ K atmospheres

already equal to or higher than 100 bar suffice to reach the [RG](#) limit. A similar tendency is found in Hamano et al. (2013).

I also find that at lower steam contents the F_{lim} is greater than the [RG](#)-limit. All F_{lim} values can be found in Table 4.1.

4.3.2 Limiting radiation values F_{lim} for pure steam

I use Eq. (4.2) to estimate the orbital distance for which a planet of given albedo is located at the boundary that separates a long-term and short-term magma ocean. To this end, the value of the limiting radiation F_{lim} corresponding to a specific water vapor pressure P_{H_2O} and rheology front temperature at the surface $T_{RF,0}$ is needed. Table 4.1 reports $F_{lim}(P_{H_2O}, T_{surf})$ for two different rheology front surface temperatures as obtained by interpolating the [OLR](#) data product of Katyal et al. (2019) (Fig. 2.7). The same values are plotted in Fig. 4.4 and are used to calculate the critical distances for the young Sun in Fig. 4.5.

Table 4.1: $F_{lim}(P_{H_2O}, T_{RF,0})$ for indicative $T_{RF,0}$ cases calculated with the Katyal et al. (2019) data.

P_{H_2O} (bar)	$F_{lim}(T_{RF,0} = 1645 \text{ K}) \text{ (W/m}^2\text{)}$	$F_{lim}(T_{RF,0}=1370 \text{ K}) \text{ (W/m}^2\text{)}$
4	16724.2	5885.6
25	1362.8	519.4
50	677.3	332.8
100	398.5	286.6
200	298.1	283.6
300	285.8	283.6

Using Equation (4.2) I calculate the orbital distance-albedo combinations for which the radiation limits (Table 4.1) of different iso-volatiles are attained (Fig. 4.5). I assume the solar luminosity at the beginning of its main sequence evolution at $\tau = 100 \text{ Myr}$ (72% of today's value) (Gough, 1981). Not all the calculated albedo values are realistic. The albedo for a cloudless steam atmosphere, based on 1D models and 3D [GCM](#) calculations lies between [0.15, 0.40] (Kasting, 1988; Goldblatt et al., 2013; Leconte et al., 2013; Pluriel et al., 2019).

Apart from the new radiation limits found, our results are in line with those of previous studies, as far as the insolation role is concerned. In Hamano et al. (2013) the threshold distance between continuous and transient [MO](#) types for albedo 0.3 and solar constant 0.72 S_0 is 0.77 AU, whereas under the same conditions our calculations show 0.79 AU. The difference is due to the lower absolute [OLR](#) steam

atmosphere limit of $282 \pm 1 \text{ W/m}^2$ that we obtain compared to the 294 W/m^2 limit employed in that study.

By raising the albedo to the critical value $\alpha_c = 0.146$ found in our simulations for an Earth-sized planet at 1 AU that outgasses 1 earth ocean at today's Sun, we obtain $\approx 12 \text{ Myr}$ MO duration. The longer solidification times of 10–30 Myr reported in Hamano et al. (2013) at the same $F_{\text{Sun}} = 285.5 \text{ W/m}^2$ for the same steam atmosphere are due to the lower surface melting temperature used ($T_{\text{RF},0} = 1370 \text{ K}$).

With an albedo of 0.63, solar constant of $0.7S_0$, and total planetary water content $X_{\text{H}_2\text{O},0} = 5.53 \cdot 10^{-2} \text{ wt\%}$ (equivalent to 405 bar) and $X_{\text{CO}_2,0} = 1.4 \cdot 10^{-2} \text{ wt\%}$ (equivalent to 100 bar), Lebrun et al. (2013) found that the distance at which the outgassed water vapor could no longer condense is 0.67 AU. Under the same conditions, excluding the influence of CO_2 , we find in our model that the atmosphere would exist in a runaway greenhouse state trapped in a continuous magma ocean at a critical distance of 0.59 AU. The reason for this discrepancy is two-fold. Firstly, the present [lbi](#) approach does not include CO_2 that also contributes to the greenhouse effect. Secondly, the absolute [OLR](#) limit used by Lebrun et al. (2013) is $\approx 200 \text{ W/m}^2$ (Marcq, 2012) (see Marcq et al. (2017) for an updated limit). This is substantially lower than the limit of 282 W/m^2 used in our study. Therefore, the shift of our limit inward towards the star corresponds to the higher critical flux that needs to be achieved in order to trigger the qualitative shift from a transient to a continuous magma ocean regime. Considering the orbital distances of the inner terrestrial planets of the solar system (Mercury–0.38 AU, Venus–0.72 AU, Earth–1 AU and Mars–1.52 AU), we find that the planets inwards of Earth could sustain a continuous MO within the range of albedos expected for a cloudless steam atmosphere (Fig. 4.5). Moreover, a 100-Myr-old Earth at 1 AU around the Sun cannot exist in a continuous MO state under any albedo for a steam atmosphere of up to 300 bar (Fig. 4.5) or of up to 1000 bar according to the recent study of Ikoma et al. (2018).

Note that in this work “continuous” magma ocean refers to planets that would cease cooling if the amount of steam in the atmosphere was conserved. This cannot be ensured under atmospheric escape processes, which have not been accounted for, and as such the limits calculated here yield the furthest possible distance from the Sun for achieving a continuous MO with a constant atmospheric steam content.

Using the database of F_{lim} that depends on both the atmospheric water content and $T_{\text{RF},0}$ that we provide in this (Table 4.1) and in the companion work, Eq. (4.2) is qualitatively extended. It covers MO type transitions for intermediate levels of outgassing below the 300 bar reference value, hence has higher F_{lim} . This database is backwards compatible and can also be used in the Hamano et al. (2013) equation.

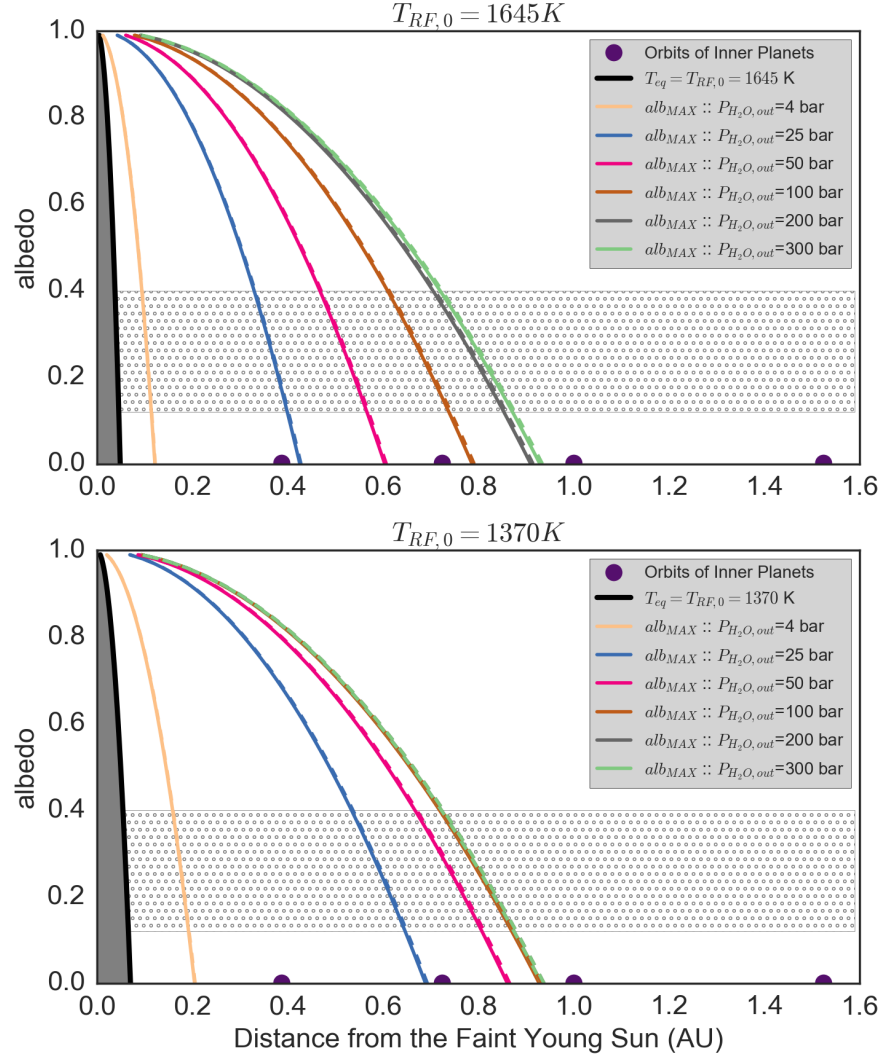


Figure 4.5: Figure from Nikolaou et al. (2019) © AAS. Reproduced with permission. Maximum albedo that a planet with a 4–300 bar steam atmosphere can possess at a given distance from the young Sun in order to maintain a long-term magma ocean, assuming two values of $T_{RF,0}$ **Upper:** $T_{RF,0} = 1645 K$, **Lower:** $T_{RF,0} = 1370 K$. I plot the critical values that separate continuous from transient magma ocean cases calculated with the use of Eq. (4.2) for several P_{H_2O} (colored lines) and employing the respective steam atmosphere mass limiting outgoing longwave fluxes (extracted from Fig. 4.4; see Table 4.1 for values). Dashed lines are obtained using the equation of Hamano et al. (2013) employing the present study’s F_{lim} limits. Not all obtained albedos are realistic. Hatched region shows the possible range of albedos for a cloudless steam atmosphere (Kasting, 1988; Leconte et al., 2013; Goldblatt et al., 2013). Black solid lines mark distances from the star for which T_{eq} is equal to the surface melting temperature of the magma ocean for the full albedo range (permanent magma ocean).

MO EVOLUTION ON OTHER PLANETS

In the following chapter the prior findings are implemented on different rocky planets, provided that those are of comparable size to the Earth. The following research question is addressed:

- Q5 How is the magma ocean on planets other than Earth? What are the likely MO cases for rocky planets (Venus, Mars) and exoplanets?

5.1 SOLAR SYSTEM PLANETS

The F_{lim} value discussed in Chapter 4 is not significantly affected by the gravitational acceleration of the planet as long as this has between 0.1 and 2 Earth masses (Goldblatt et al., 2013). For greater planetary mass the pressure levels in the atmosphere change height, as does the level of opacity depth which is crucial for the calculations of the outgoing radiation. Goldblatt et al. (2013) also calculated that for a planet of half the Earth mass, the OLR limiting flux is lowered by only 5 W/m². In comparison, $F_{lim} \approx 282 \text{ W/m}^2 \pm 1 \text{ W/m}^2$ as calculated for the Earth by Katyal et al. (2019) has a lower uncertainty. Therefore, Eq. (4.2) can be applied without loss of generality to planets between 0.1 and 2 Earth masses, using the $F_{lim}(P_{H_2O}, T_{RF,0})$ (Table 4.1) calculations by Katyal et al. (2019).

5.1.0.1 Venus

Given their similarity in mass and radius, the criteria for a continuous magma ocean applied to Earth can be extended to Venus. This study finds that Venus orbit qualifies for a long-term magma ocean within a wide range 0.15–0.40 of planetary albedos proposed for cloud-free steam atmospheres, as long as its outgassed steam atmosphere amounts to 200 bar or more for a surface solidification temperature of 1645 K (Fig. 4.5). In the case of the lowest solidification temperature ($T_{RF,0} = 1370 \text{ K}$), the minimum atmosphere required for a continuous magma ocean at Venus orbit is 50 bar (Fig. 4.5). This highlights that the melt composition alone could dictate a different magma ocean evolution path for two hypothetical planets with equal water vapor atmosphere masses.

5.1.0.2 Mars

Extending the findings of Chapter 4 to Mars it is found that its orbit does not qualify for a continuous magma ocean stage. This is seen in

Fig. 4.5 for the orbital distance 1.52 AU. Any magma ocean on Mars would therefore be transient. A first order assessment of its duration is here done by aid of the grey atmospheric coupling.

The comparison between Earth and Mars MO duration (Figure 5.1) reveals that assuming the same volatile concentration in H_2O and CO_2 the MO duration on Mars is shorter. Such effect is expected, since the Mars mantle volume is lower than that of Earth, therefore the same concentration corresponds to lower absolute amount of volatiles available for outgassing.

The magma ocean stage on Mars lasts at maximum 10 Myr for 10% water content and 10% CO_2 content. Those abundances are very unlikely. In lower concentrations, the estimated MO on Mars lasts shorter and therefore has geologically insignificant duration. This suggests that Mars could have had multiple magma oceans with enough time to solidify in between incoming impactors, in case those impacts occur with frequency of less than 10 Myr.

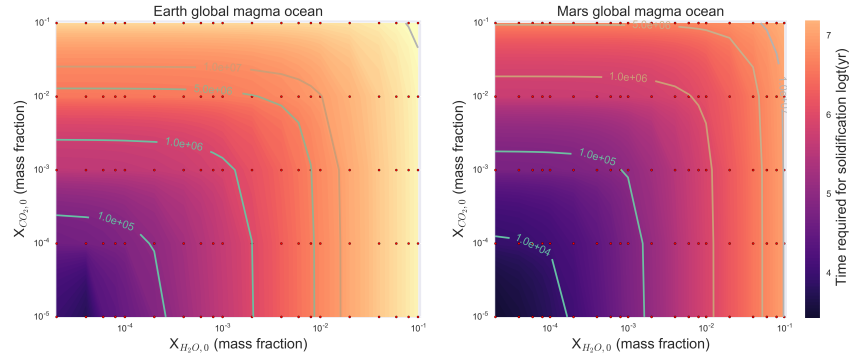


Figure 5.1: Earth (**left**) and Mars (**right**) global magma ocean duration assuming varying H_2O and CO_2 volatile abundances and grey atmosphere.

5.2 EXOPLANETS

Interestingly, the drop of surface temperature during cooling combined with the tendency of stellar environments to gradually strip planets of their atmospheres (Johnstone et al., 2015; Odert et al., 2018; Lammer et al., 2018) (therefore lowering the surface pressure P_{H_2O}) could result in the same outgoing radiation limit during planetary evolution. One sees this in Figure 4.4 taking any constant OLR value that crosses multiple isovolatiles. In that case the stellar evolution plays a primary role in the continuous magma ocean fate. A G-star that increases in luminosity with time (Gough, 1981) favors the maintenance of an existing magma ocean because it contributes warming at the critical distance. In contrast, continuous magma oceans will be more elusive around M-stars whose luminosity decreases with time

(Baraffe et al., 2015). This is because a continuous magma ocean close to its critical distance will progressively receive less stellar radiation eventually creating a window of cooling. A buffer against this effect is the additional vapor outgassing that increases the opacity and lowers the required F_{lim} . However, during progressive cooling the interior will exhaust its water supply into the atmosphere. Under these conditions only water-rich planets can sustain a continuous magma ocean. This shows that there are numerous processes that affect MO feasibility. Consider also the possible Trappist-1 exoplanet migration scenarios (Unterborn et al., 2018), that were suggested in order to justify water-rich composition.

I explore the findings in view of potentially rocky exoplanets that have radius and/or mass within few Earth units (see parameters in Table 5.1).

Results suggest that there are orbital regions where the magma ocean can be transient, permanent and an intermediate region where it is “conditionally” continuous (Fig. 5.2). “Conditionally” here refers to the dependence on water content and rheology front temperature. One observes the overlap in the regions of continuous magma ocean regime for different $T_{RF,0}$. Considering the interior composition adds a measurable level of uncertainty since different planets with different atmospheric water content and solidification temperatures can be characterized by the same outgoing OLR.

Note that unless one is able to constrain the surface pressure of water vapor on an exoplanet, not feasible with the current observational capabilities (Madhusudhan et al., 2014), it will not be possible to constrain the type of evolutionary (continuous, transient) magma ocean. However, hypotheses and proxies concerning planetary water abundance could break this OLR degeneracy that disappears at low vapor pressures close to 4 bar (see Fig. 4.4). A water-poor planet with a thin atmosphere of 4 bar water would be sensitive to the $T_{RF,0}$ value for developing a continuous/transient MO close to their separation limit. Such could be the case for distinguishing the compositions of HD 219134 b and c if one is found in magma ocean state and the other is not (Fig. 5.2). Kepler 36b’ s orbit is further than this distinction possibility and receives enough energy from the star to be in continuous magma ocean as long as it has at least 4 bar water. As soon as its atmosphere is lost it would resemble a BB, in which the effect of any water present on lowering the liquid viscosity would ensure the rapid MO solidification, as it was earlier shown (Table 3.1). Planets Kepler 236c, Ross 128b and LHS 1140c on the contrary are located in the F_{lim} region for relatively high vapor pressure. Assuming ≥ 200 bar, the system converges to the minimum OLR solution of 282 W/m^2 (see Fig. 4.4) which is maintained for up to 1000 bar vapor pressure (Ikoma et al., 2018). Detecting any magma ocean state on those planets would be difficult because of the opaque atmosphere.

Table 5.1: Planet and host star parameters used in Fig. 5.2.

Planet	Orbital distance R (AU)	Host star	T_{eff} (K)	R_{star} (in solar units R_{\odot})	Luminosity L (in solar units L_{\odot})	Ref.
*Kepler 236 c	0.1320	Kepler 236	3750	0.510	-	exoplanet.eu/catalog/
55 Cancri e	0.0156	55 Cancri	-	-	0.59	exoplanet.eu/catalog/ Gough (1981)
Earth	1.0000	Sun (100 Myr old)	5326	1.000	0.72	
*Kepler 36 b	0.1151	Kepler 36	5911	1.619	-	openexoplanetcatalogue.com
*HD 219134 b&c	0.0388 & 0.0653	HD 219134	3131	0.186	-	exoplanet.eu/catalog/ openexoplanetcatalogue.com
*Ross 128 b	0.0496	Ross 128	3192	0.197	-	openexoplanetcatalogue.com
*GJ 1132 b	0.0154	GJ 1132	3270	0.207	-	openexoplanetcatalogue.com
*LHS 1140 b&c	0.087 & 0.02675	LHS 1140	4699	0.778	-	openexoplanetcatalogue.com
*Kepler 78 b	0.01	Kepler 78	5089	0.74	-	exoplanet.eu/catalog/

* In absence of values of luminosity relative to L_{\odot} I calculated the stellar luminosity directly from T_{eff} , R_{star} data.

However, if detected it would mean that the planet formed within a water-rich environment that ensured the minimum atmospheric 200 bar required for the continuous magma ocean. Especially for LHS 1140c, the planet LHS 1140b located in the transient MO region of the same system could provide complementary information for the likelihood of high water content. GJ 1132b is located at the compositional distinction limit. Its potential MO has been studied before by Schaefer et al. (2016). A low atmospheric water content in its MO state would be a proxy of primitive silicate composition. Any of the continuous magma oceans on those planets would eventually solidify if their atmospheric water were lost and were not replenished by the interior.

The possibility of observing a transient magma ocean system is insignificant due to the order of million years duration that I find for them, which is very short compared to observable systems' ages. Detection of continuous magma oceans on candidate planets (at orbits receiving 282 W/m^2 or more (see Fig. 5.2)) is challenging but is aided by the fact that the planet's MO brightness temperature would be much higher than the one corresponding to its equilibrium temperature, yielding OLR of up to $16,000 \text{ W/m}^2$ (see Table 4.1). Such measurements require secondary transit observations as carried out for 55 Cnc e with the Spitzer telescope (Demory et al., 2016) aided by the longer wavelength coverage of JWST. A low brightness temperature, in agreement with a low OLR of 282 W/m^2 , would be an indication towards high steam pressures (see companion paper for possible emission spectra). The surface pressure is not retrievable with the current capabilities but promising methods are developed for low pressure atmospheres (10 bar) that demonstrate pressure broadening of absorbers such as CO_2 and O_2 (Misra et al., 2014). Transmission methods could not probe high surface pressure atmospheres but the OLR would be already near the runaway greenhouse limit in those cases so one should focus in retrieving the latter. A measured OLR = 282 W/m^2 would be indicative of MOs with high steam pressures. I suggest the auxiliary/complementary use of observations obtained from the permanent magma ocean type, such as potentially on 55 Cancri e (Demory et al., 2016; Angelo et al., 2017) and Kepler 78b. From there one could isolate characteristic atmospheric signatures such as: the atmospheric effects of evaporated silicate species that develop over the molten rocky surface (Fegley et al., 2016; Kite et al., 2016; Hammond et al., 2017) and the oxides in the presence of a steam atmosphere (Fegley et al., 2016). Detecting similar silicate cloud signatures on planets close to the continuous MO compositional distinction that is observed at low vapor pressures (4 bar) would serve as a proxy of their composition ($T_{RF,0}$) and of their water content.

Detection of evolutionary magma oceans additionally requires stellar ages in order to focus on systems with ongoing planetary formation, preferably after recently completed accretion. Constraining the

albedo from observations is a possibility given favorable orbital configurations (Madhusudhan et al., 2014; Kite et al., 2016) and would help define the range of orbital distances for a conditionally continuous magma ocean.

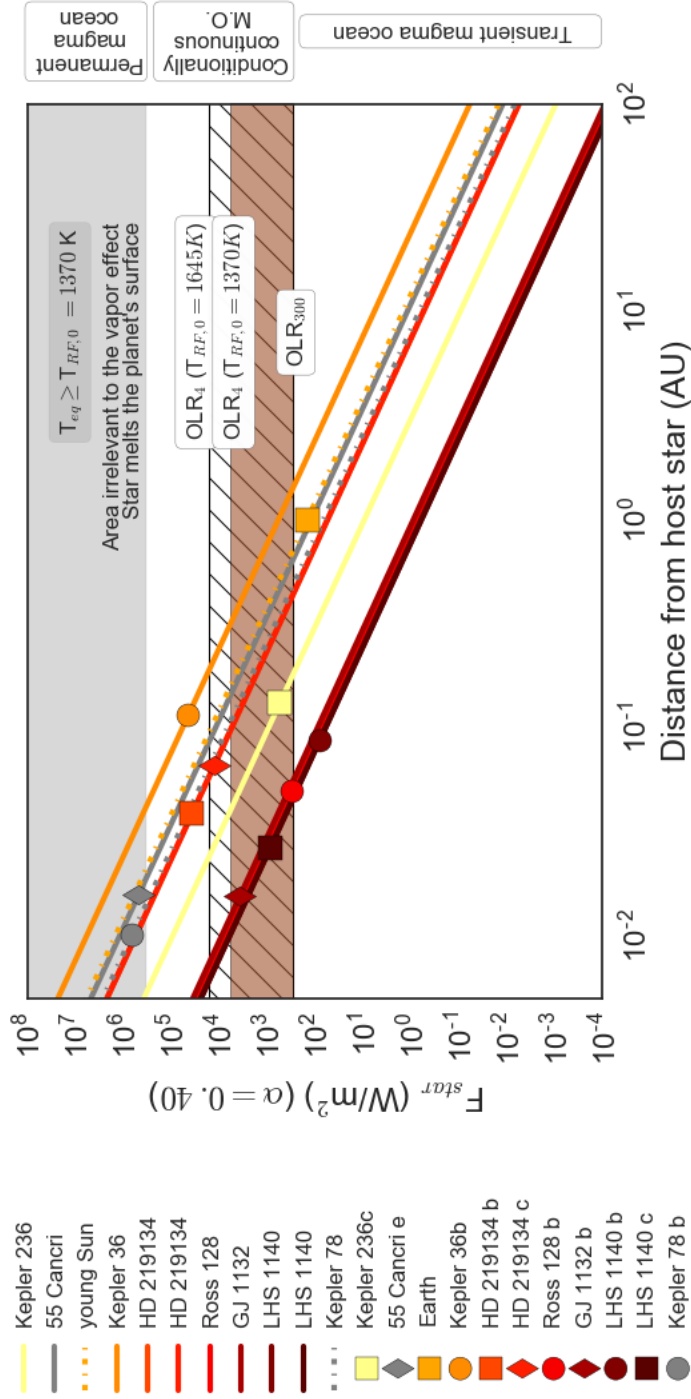


Figure 5.2: Figure from Nikolaou et al. (2019) © AAS. Reproduced with permission. Incoming stellar energy flux at various orbital distances around M and G stars for a planet with albedo $\alpha = 0.4$ (maximum value for cloudless water vapor case). Examples of potentially rocky exoplanets are plotted on the respective host star curve. Grey shaded region corresponds to permanent magma ocean at the lowest mantle melting temperature considered. Regions are drawn for 4–300 bar [OLR](#) for two different rheology front solidification temperatures: $T_{RF,0} = 1370$ (line-hatched) and 1645 K (brown shaded). Star and exoplanet parameters are found in Table 5.1.

DISCUSSION

It was previously showed how the MO duration is tied to the outgassing. The latter is sensitive to factors that modify the amount of enclosed melt or the upper mantle temperature. Two such factors are the assumptions of surface rheology front temperature and critical melt fraction. They vary significantly among studies and they are sources of deviations when comparing with the Ref-A results (e.g. Hamano et al., 2013, assumed $T_{RF,0} = 1370$ K) (Lupu et al., 2014, $T_{RF,0} = 1560$ K) and (Hier-Majumder et al., 2017, $T_{RF,0} = 1758$ K, $\phi_C = 0.30$).

However, keeping both above assumptions constant, the outgassing in this study still represents an upper limit with respect to other studies. The reason is two-fold. Firstly, the use of one-phase adiabat (Section 2.3.3) minimizes the amount of enclosed melt at the end of the MO due to its high slope with respect to the melting curves. From the mass conservation follows that the volatile outgassing into the atmosphere maximizes. Employing a two phase adiabat instead tends to parallelize the slope to the melting curves and results in more enclosed melt and lower outgassing. E.g. the Ref-A case in Lebrun et al. (2013) outgasses 200 bar H_2O compared with 220 bar (this study) via this effect. However, usage of the Solomatov et al. (1993b) two-phase adiabat is subject to strict assumptions (i.e. linear melting curves).

Secondly, I did not account for the Katz et al. (2003) depression of the solidus that accompanies the mantle enrichment in water. Initially, note that the parameterization suggested by Katz et al. (2003) modifies the surface melting temperature $T_{RF,0}$ above the error margin (20 K) for an atmospheric pressure ≥ 30 bar. Furthermore, it is only valid for pressures up to 8 GPa, corresponding to depth of 220–250 km. Indeed, it was motivated by solid state mantle dynamics and explicitly designed to aid modeling of melt generated locally at shallow depth (Noack et al., 2012; Tosi et al., 2017). It cannot be extrapolated to higher pressures in the upper mantle, let alone throughout the range of a global MO (which covers pressures from the surface down to ~ 135 GPa).

Nonetheless, based on the mass balance (Eq. (2.33)), I make a first order estimation of the melting temperature reduction effect upon increasing the water concentration in the melt. Assuming that both the solidus and the liquidus are reduced by the same amount for the same water content (see Katz et al. (2003), Section 2.2 therein), the MO solidification will take place at a lower temperature. In this respect our model provides lower bounds on the solidification time for the same outgassed quantities (Fig. 3.9). However, estimating the

melt fraction using a wet solidus comprises more than a linear shift of melting curves, which would leave the MO final melt fraction unchanged. In fact, the inversion of the saturated solidus that appears near the surface is not necessarily matched by the saturated liquidus non-linear shape (Makhluf et al., 2017). A wet solidus essentially would increase the enclosed melt at the MO end. Based on our current anhydrous parameterization our final outgassing estimations are upper limits because the remnant melt is here minimum (Fig. 3.7). A detailed study is required to quantify the overall effect on the solidification time taking into account the surface solidus depression and the decrease in degassing, which exert opposing tendencies on the MO duration.

All three factors that decrease the $T_{RF,0}$ (see Table 3.1), such as atmospheric steam pressure (1000 bar cause a decrease of 100 K (Katz et al., 2003)), varying silicate content (decrease of $T_{RF,0}$ by up to 400 K comparing peridotite to rhyolite), and redox state of the melt, would further delay the solidification of the MO. Significant work has been done towards resolving melt redox evolution (e.g. Schaefer et al., 2016; Wordsworth et al., 2018) and combining it with silicate content evolution in the melt (Gaillard et al., 2015), which is a future step for a more detailed modeling.

Dynamically, the MO termination is characterized by two main nonlinearities. One is the decelerating advance of the solidification front from the bottom upwards that results in a shallow magma ocean of 50 km or less for $\approx 50\%$ of the magma ocean lifetime. The other is the abrupt end of the magma ocean stage, which is marked by a discontinuous viscosity jump of >8 orders of magnitude across the critical melt fraction.

The catastrophic H_2O outgassing phenomenon is an additional non-linear process. For an Earth-sized planet it ensues when the total melt volume fraction drops below 30% (Fig. 3.6). Adopting the Katz parameterization for the late shallow MO stage does not prevent that degree of solidification. This is because even if the solidus depression were to ensure fully molten water-enriched layers, its maximum range of validity is 8 GPa. This barely covers 10% of the Earth mantle volume. It takes a combination of solidus depression at higher pressures (not yet experimentally confirmed) and a two-phase temperature profile such that global melt remains higher than 30% of mantle volume, in order to hinder the abrupt H_2O outgassing (Fig. 3.6). The present model shows that initial cooling is instead very rapid and causes the solidification of 90% of the mantle within few thousands of years via bottom-up crystallization (Fig. 3.1). The phenomenon could be mitigated if solidification proceeded from the middle outwards, maintaining a large part of the mantle molten in the form of a basal MO (Labrosse et al., 2007). A detailed two-phase flow model such as Hier-Majumder et al.

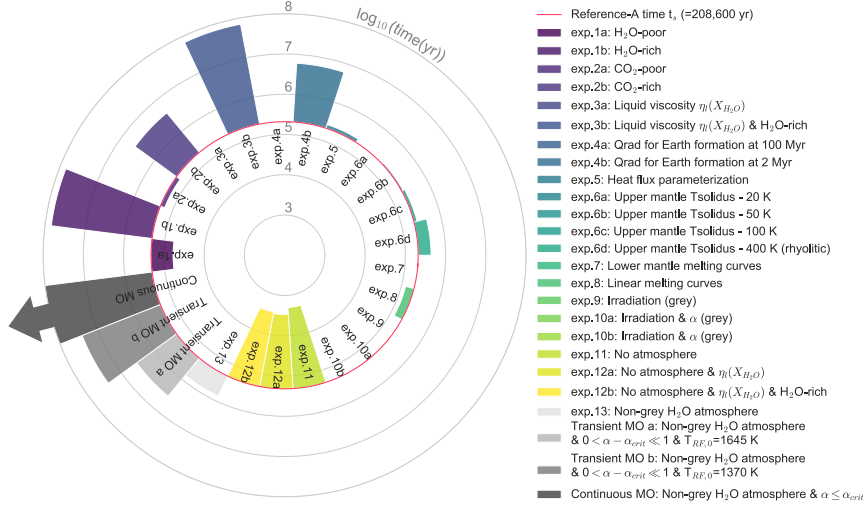


Figure 6.1: Figure from Nikolaou et al. (2019) © AAS. Reproduced with permission. Cumulative plot of the sensitivity experiments for the solidification time t_s (in \log_{10} units) using the 1D COMRAD model, compared to the Ref-A timescale (red line). Labels are as in Table 3.1, which contains the details of each experiment 1–13. Three additional columns are plotted with the outcome of specific settings using the lbl atmosphere (greyscale). Parameters in each experiment as in Ref-A unless otherwise specified. The “transient” MO duration corresponds to the t_s obtained for the highest acceptable albedo above α_{crit} , to the limit of model resolution (lowest cooling flux 1 W m^{-2}), for two different surface rheology front temperatures $T_{RF,0}$. The time arrow of the “continuous” MO is obtained for $\alpha \leq \alpha_{crit}$ and hints to effectively unbounded duration, in the absence of atmospheric loss processes.

(2017), expanded to cover the middle point solidification, is required to quantify this effect in detail.

Moreover, I adopt here the two atmospheric species H_2O and CO_2 but acknowledge the need for including additional trace species that may alter the radiative balance and/or react with surface melt (Gailard et al., 2014; Lupu et al., 2014; H. L. Zhang et al., 2017; Wordsworth et al., 2018). In addition, processes that alter the albedo during the MO evolution (Pluriel et al., 2019) could have an effect on the MO evolution into transient or continuous type.

It is additionally important to consider whether a planetary body has had a long impact history or has chemically evolved increasing its silicate content before impacts remelt it into a magma ocean (Lammer et al., 2018). Such bodies could more easily maintain a secondary continuous magma ocean. Due to their lower $T_{RF,0}$ they would require smaller steam atmospheric mass, instead of the reference 300 bar (one Earth ocean) that is usually assumed in runaway greenhouse studies (e.g. Lebrun et al., 2013; Massol et al., 2016; Marcq et al., 2017). On the contrary, a chemically unevolved silicate primitive composition that melts at high temperatures would require a massive steam atmo-

sphere >100 bar in order to maintain a continuous magma ocean. I conclude that past events of chemical alteration may influence the fate of the magma ocean under the same orbital configuration. Therefore the age of the star and of its planetary system matters. Evolution of the mantle composition during the MO solidification (Elkins-Tanton, 2008; Schaefer et al., 2010) will be an additional factor that prolongs the MO lifetime if it results in decreased $T_{RF,0}$.

The immediate outgassing of CO_2 could have an effect on the hydrodynamic escape process which usually is studied on the assumption that CO_2 is a minor gas in the atmosphere (Hamano et al., 2013; Lupu et al., 2014; Hamano et al., 2015; Airapetian et al., 2017; Wordsworth et al., 2018). In particular, a low mixing ratio of water in the atmosphere together with abundant CO_2 is known to create a cold trap over the convective atmospheric region and to hinder the thermal escape of the heavier and ionized oxygen atoms. Wordsworth et al. (2013b) argue that high CO_2 mixing ratio would not effectively prevent the escape. In order to mitigate water loss to space, Kurokawa et al. (2018) suggested a water ingassing process, posterior to the MO, that could operate through early plate tectonics. It could maintain 2–3 Earth oceans bound in the interior against hydrodynamic escape and could justify D/H ratios.

Combining the response of varying atmospheric composition, a baseline evolution of which is provided here (Figures 3.5, 3.8), with different scenarios of early XUV stellar radiation (Lammer et al., 2008; Johnstone et al., 2015; Airapetian et al., 2017; Odert et al., 2018), could help resolve the issue of atmospheric loss. In particular for the case of Mars, $\text{H}_2\text{O}/\text{CO}_2$ degassed atmospheres were provided as input to study the rate of atmospheric loss under hydrodynamic escape conditions (Odert et al., 2018). Mars-like planetary embryos were chosen as a likely precursor at the orbits of Venus, Earth and Mars and were exposed to the EUV emission of a slowly, moderately and rapidly rotating young Sun-like star at $\tau_{\text{CAI}} + 10$ Myr. Different atmospheres were obtained by varying the initial volatile abundance and magma ocean depth. The magma ocean degassed atmospheres of 100 bar were lost very rapidly, while the maximum possible outgassed atmosphere of 1237 bar was removed within 32–55 Myr at Venus orbit only assuming very high solar EUV and fast stellar rotation (Fig. 6.2). Intermediate mass atmospheres 96–233 bar were lost within 4–17 Myr at Venus and Earth orbits, making for a dry leftover protoplanetary body. On the contrary, they were maintained at Mars orbit assuming a slow stellar rotation. Dissociated CO_2 was lost efficiently while molecular CO_2 was retained. Given that CO_2 outgasses early due to its low solubility, it strengthens the case for preservation of the atmospheric mass at conditions of intermediate solar EUV activity and inefficient photodissociation. The time scales of Mars MO solidification (0.1–2 Myr) are rapid compared to the atmospheric loss process at Mars orbit, which

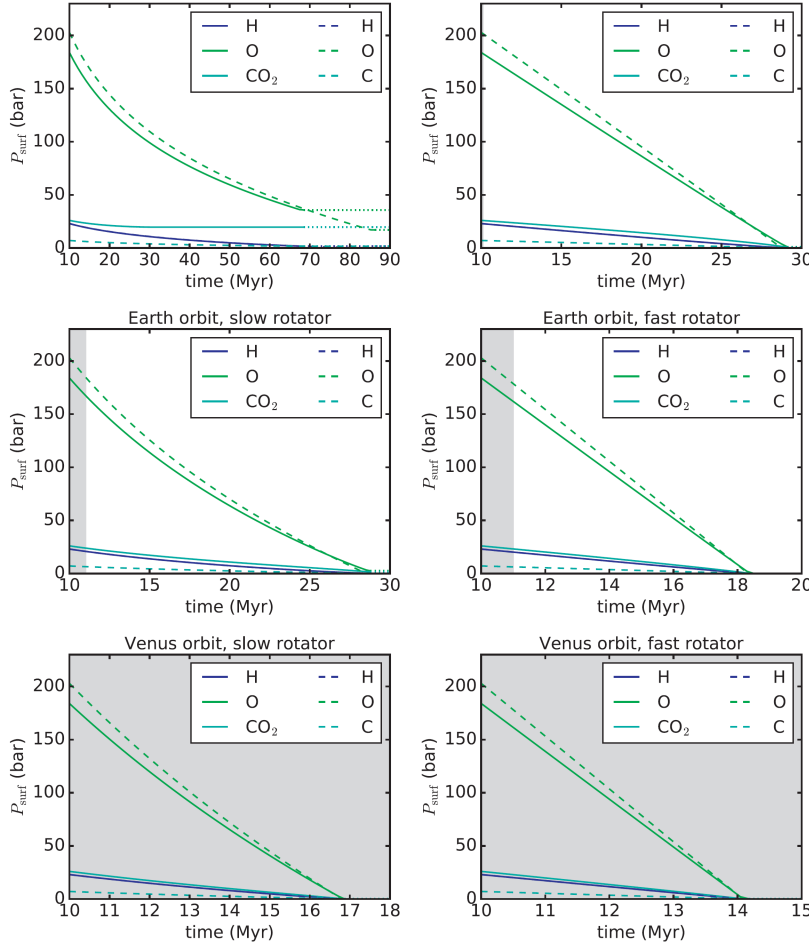


Figure 6.2: Figure by Odert et al. (2018). Reused with permission. Hydrodynamic escape of a Mars-size object atmosphere. Evolution of the partial surface pressures of an escaping steam atmosphere (207 bar H₂O, 26 bar CO₂) around a Mars-like planetary embryo located at the orbits of Mars, Earth and Venus (top to bottom) around a slow (left) and a fast rotator (right). Solid lines indicate the results if CO₂ remains in molecular form and dashed lines assume complete dissociation into O and C. The evolution of H in both cases is almost indistinguishable. Dotted horizontal lines indicate the presence of three major species due to accumulation of a former minor one which cannot be modeled with the present approach. The typical water condensation times at the respective orbits (Lebrun et al., 2013) are shown as shaded areas (the short 0.1 Myr interval for Mars' orbit is almost invisible).

is one order of magnitude slower (17–60 Myr). For the case of Earth orbit they tend to be comparable, of the order of few Myr. Taking into account the larger gravitational pull of an Earth-size planet at Earth orbit the hydrodynamic escape rate will be lower since it is inversely proportional to the object's gravitational potential. By this argument it is suggested that the Earth MO degassed atmosphere will be retained for longer.

Regarding the earliest constrain of the 4.4 Ga Jack Hills zircon (Peck et al., 2001) for the conditions on Earth, the magma ocean duration provides with some perspective. Magma ocean's brief projected duration on Earth (maximum ~ 1 Myr) is instantaneous compared to the geological time scale of ~ 100 Myr that separates the zircon dating $\tau_{CAI} + 160$ Myr and the lunar impact at $\tau_{CAI} + 60$ Myr (Barboni et al., 2017). A magma ocean duration of 100 Myr would need more than 100 Earth ocean masses to be justified, which is an unrealistic parameter assumption. That amount of water could have been indeed delivered in the course of stochastic impacts that accumulate mass onto the protoplanetary embryo that grew to Earth size. Despite not being discarded on the basis of statistical probability, that amount of water is unlikely to have been delivered simultaneously and cannot be considered as an instantaneously available reservoir for Earth. Moreover, water would have been subject to loss processes after each impact. Earth orbit does not qualify for a continuous magma ocean either, discarding the alternative scenario for prolonging its solidification process. By the above argumentation, it is unlikely that a magma ocean caused by the lunar protoplanetary impact was preserved until the zircon's timing.

We obtain the following alternative hypothesis regarding the zircon precipitation: The latest stages of magma ocean produce melt that is progressively enriched in water up to 2 orders of magnitude with respect to the initial abundance (Fig. 3.4.A). When the rheology front reaches the surface and the magma ocean ends, the enclosed melt underneath the surface is rich in water. This could serve as a source of hydrous parent melt to the precipitated zircon mineral. Additional modeling of the solid-liquid matrix thermo-chemical evolution such as Hier-Majumder et al. (2017) could help quantify the time scale of this process against which to evaluate this hypothesis. The alternative zircon explanation assumes a hydrous crust processing and requires its recycling through plate tectonics (Mojzsis et al., 2001). There has been yet little constrain on the onset of mantle convection as well as of the feasibility of plate tectonics onset within 100 Myr, that make this assumption subject to additional unknowns.

Lastly, the grey atmosphere as was implemented in this model is an easily applicable solution for the MO simulation but it can be insensitive to the intensity of insolation. This study also finds that the grey approach is especially sensitive to the different absorption coefficient values used for the CO_2 (See Elkins-Tanton (2008) for a wide range of k_{0,CO_2} explored for fixed $\text{H}_2\text{O}/\text{CO}_2$ atmospheric mixtures). The use of k_{0,CO_2} derived from present ECS studies is unsuitable for the early Earth climate. The *lb* approach remains computationally costly, but the pre-calculated *OLR* values for pure steam are a first step towards a wider use of an atmosphere that better resolves the *IR* absorption.

A concentrated overview of the factors that affect the magma ocean duration, that were examined in this study, is seen in Figure 6.1. The effect of water-rich atmospheres stands out both in grey and in [lbi](#) atmospheric radiative transfer approaches. The [BB](#) simulations show a weak dependence on the water content during a generally rapid solidification process.

LIMITATIONS-CRITICISM

Non-linearities inherent to the circulation dynamics cannot be resolved with a one-dimensional representation of the coupled system. However, I included an overview of the magma ocean's trajectory in the Ra , Pr space (Fig. 3.3). This will help identify the circulation regime at different periods in the [MO](#) thermal evolution. Vigorous convection is likely to generate non-linearities and amplify perturbations in the velocity and pressure fields. Those could possibly affect the equilibration of volatile concentration within the bulk of the [MO](#) fluid and influence the outgassing process. Such phenomena would disturb the lateral homogeneity assumed in the 1D models by construction. Lateral variability that emerges in liquid-like fluids (e.g.: as it is known to occur in the atmosphere) could affect the exchange of energy and hinder mixing in specific spatial and temporal scales because of eddy formation. I do not resolve the effect of those non-linear processes in our 1D model, but I indicate regimes for further scrutiny.

It is worth emphasizing that in the [lbi](#) simulations, the T_{surf} obtained after the end of the magma ocean phase is not informative on the surface conditions, but merely suggestive of a fully solidified mantle. After the end of the magma ocean stage, the model suggests that T_{surf} will be lower than $T_p = T_{RF,0}$, but its exact value cannot be resolved with the coupled [lbi](#)-interior. The reason is that for surface temperatures lower than the water critical point (647 K), the simple subtraction of F_{Sun} from the [OLR](#) used for the atmospheric radiative balance (Eq. 2.41) does not apply. Below the critical point, condensation of water vapor to a surface ocean should be considered. Moreover the replacement of supercritical vapor properties with steam tables of subcritical water is required in the [lbi](#) model to treat the water condensation. Further work is required on this aspect in order to extend the study to the post magma ocean thermal evolution. Nevertheless, the water critical point is well below the surface solidification front temperature, and the model range adequately covers the magma ocean stage, which is the focus of this work.

The results presented in this study only concern a [MO](#) with a molten surface exposed to the lower atmosphere throughout its complete duration. The present study does not discuss the stage of subsurface magma oceans, where a crust is present for part or throughout the to-

tal magma ocean duration and thermally isolates the molten silicates underneath. Such could have been the case for the Moon (Wood et al., 1970). As far as MO viscosity is concerned, while I cannot study the viscosity at high pressure, this is less relevant for the late stages of the magma ocean. At those relatively low pressures, the documented lab knowledge is applicable. At near surface MO conditions ($P = 1\text{--}2$ GPa, $T = 873\text{--}1223$ K) the representation is satisfactory because the viscosity of melts is better constrained there. I notice that the water effect on the viscosity is significant at low quantities where it demonstrates an exponential dependence as follows: where $\exp(\nu_{X_{H_2O}})$ decreases for increasing X_{H_2O} (Kono, 2018). For $X_{H_2O} > 20\%$ the effect is not important because the water dissolves in molecular form and affects neither the mineral structures (Stolper, 1982) nor the degree of polymerization (Burnham, 1975).

Likewise in the melt and in the atmospheric gas mixture chemical reactions are not included. This is evident by the use of constant melting curves and by the solubility curves. The latter are valid for pure H_2O or CO_2 species in balance with silicate melt and ignore gas-gas interactions. As seen in Section 3.2.3, for a constant quantity of mols the volatile partial pressures are modified by the mean molecular weight of the atmosphere. The partial pressure of a gas species is degenerate with respect to the existence of other gas species at various concentration combinations. Therefore the gas species mixing ratio may correspond to multiple solutions, depending on the background composition. The suggestions of volumetric mixing ratio in the atmosphere in this study are thus indicative of the limited gas species assumed. Moreover, the qualitative switch of the atmosphere from CO_2 -dominated to H_2O -dominated will occur at higher H_2O content than the one assumed in Ref-A setting. Evaluation of the Dalton's law on the Ref-A simulation products reveals a <2 factor decrease in the grey emissivity that is not expected to affect the MO solidification times.

CONCLUSIONS

I have conducted a systematic analysis of the numerous factors and physical processes that affect the thermal and outgassing evolution of a global terrestrial magma ocean (Fig. 6.1). The dominant effect is the steam atmosphere blanketing. Silicate-evolved melts have lower melting temperature which causes linear increase in the solidification time. Such chemical evolution is found to decrease the solidus and it is the next most prominent factor for prolonging the transient MO lifetime. Water-dependent viscosity can be ignored for primitive compositions and for planets with greenhouse atmospheres, while it should be considered for atmosphere-free planets and for silicate-evolved melt compositions.

I emphasize that at the magma ocean end, the mantle can store between 45 and 10% of its initial H₂O reservoir and only 6% of the CO₂. The massive outgassing of CO₂ that precedes the catastrophic H₂O outgassing could have an effect in the early atmospheric escape. The qualitative switch of the atmosphere from CO₂-dominated to H₂O-dominated is not likely to occur for the conservative volatile reservoir estimates of Earth but requires multiple Earth ocean water masses as initial planetary content.

The magma ocean duration is closely tied to the degassed amount of volatiles with greenhouse potential. For Earth, its lifetime does not exceed 5 Myr assuming a water reservoir as large as 5 Earth's oceans while CO₂ plays a less important role.

The calculation of the thermal emission for a pure steam atmosphere (Katyal et al., 2019) shows that the MO solidification can be effectively halted at a suitable minimum surface pressure for a given melting temperature at limits that differ from the constant 282 W/m² RC limit. Under no combination of parameters is the early Earth found to exist in a continuous magma ocean state. The enrichment of the melt in water attains its maximum toward the latest stages of the magma ocean and it remains enclosed and located underneath the rheology front upon the magma ocean termination. The hypothesis that this enclosed melt could serve as a suitable hydrous parent melt of the oldest precipitating zircons at the high temperature and low pressure conditions that characterise the findings in the Jack Hills, requires additional modeling to be addressed. Since the final state of the magma ocean provides a range of such conditions, this hypothesis is worth to be further investigated.

The case of Venus could accommodate a continuous magma ocean stage in the early history, provided that at any point in time more

than 200 bar were found in steam form in its atmosphere. Under conditions of enhanced atmospheric escape a water-rich interior could replenish the lost H_2O by interior degassing, and maintain the required outgoing radiation threshold. Both delivery of water through late bombardment and inclusion of multiple water oceans in the Venus protoplanetary embryo are compatible with such hypothesis. A silicate-evolved composition for Venus (close to that of rhyolite) would favor the hypothesis that a conditionally continuous MO took place in the past, since it further lowers the minimum requirement of atmospheric steam mass to 100 bar surface pressure.

A water vapor dominated and magma ocean degassed atmosphere of $\sim 100 - 250$ bar on Mars-sized protoplanetary embryo takes 4–17 Myr to be lost through hydrodynamic escape, subjected to varying pre-Main sequence solar rotation and activity scenarios. Molecular CO_2 is not easily lost compared to the photodissociated species, which could suggest that CO_2 atmosphere is easier to preserve around young stars with moderate rotation and EUV activity.

I find that a molten rocky exoplanet with atmosphere poor in water is a suitable observation target to acquire information on its mantle surface rheology front temperature. The $\sim 10,000 \text{ W/m}^2$ difference in OLR for non-massive (~ 4 bar) steam atmospheres between planets with and without a magma ocean can be used as a proxy of different melting temperatures that disentangles surface compositions. Surface information would however be masked at higher vapor pressures (> 100 bar).

I discussed the set of permanent, conditionally continuous and transient MO types. Those can be viewed as stages, among which a planet can be reassigned during stellar evolution or via potential orbital migrations. Future studies on the thermal and chemical evolution of magma oceans in the solar and extrasolar systems can benefit from our comprehensive model analysis of the numerous factors that influence it. In return, our model will benefit from future observations of albedo on exoplanets close to the compositional distinction at low $P_{\text{H}_2\text{O}}$ OLR limit and spectral properties of permanent magma ocean planets expected from future missions such as *ARIEL* (Turrini et al., 2018) and *PLATO* (Rauer et al., 2014) that will provide stellar age constraints.

BIBLIOGRAPHY

- Abe, Y. (1993). "Physical state of the very early Earth". In: *Lithos* 30.3–4, pp. 223–235. DOI: [10.1016/0024-4937\(93\)90037-D](https://doi.org/10.1016/0024-4937(93)90037-D).
- (1997). "Thermal and chemical evolution of the terrestrial magma ocean." In: *PEPI* 100.1–4, pp. 27–39. DOI: [10.1016/S0031-9201\(96\)03229-3](https://doi.org/10.1016/S0031-9201(96)03229-3).
- Abe, Y. and T. Matsui (1985). "The formation of an impact generated H₂O atmosphere and its implications for the early thermal history of the earth." In: *JGRS* 90.S02, pp. C545–559. DOI: [10.1029/JB090iS02p0C545](https://doi.org/10.1029/JB090iS02p0C545).
- (1988). "Evolution of an impact- generated H₂O - CO₂ atmosphere and formation of a hot proto- ocean on earth". In: *J Atmos Sci* 45.21, pp. 3081–3101. DOI: [10.1175/1520-0469\(1988\)045.eprint:10.1175/1520-0469\(1988\)045<3081:E0AIGH>2.0.CO;2](https://doi.org/10.1175/1520-0469(1988)045.eprint:10.1175/1520-0469(1988)045<3081:E0AIGH>2.0.CO;2).
- Airapetian, V. S., A. Gloer, G. V. Khazanov, R. O. P. Loyd, K. France, J. Sojka, W. C. Danchi, and M. W. Liemohn (2017). "How Hospitable Are Space Weather Affected Habitable Zones? The Role of Ion Escape". In: *ApJL* 836.1, p. L3. DOI: [10.3847/2041-8213/836/1/L3](https://doi.org/10.3847/2041-8213/836/1/L3).
- Allègre, C. J., G. Manhès, and C. Göpel (Apr. 1995). "The age of the Earth". In: *Geochimica et Cosmochimica Acta* 59.8, pp. 1445–1456. DOI: [10.1016/0016-7037\(95\)00054-4](https://doi.org/10.1016/0016-7037(95)00054-4).
- Altwegg, K., H. Balsiger, A. Bar-Nun, J.-J. Berthelier, A. Bieler, P. Bochslers, C. Briois, U. Calmonte, M. Combi, J. De Keyser, et al. (2015). "67P/Churyumov-Gerasimenko, a Jupiter family comet with a high D/H ratio". In: *Science* 347.6220, p. 1261952. DOI: [10.1126/science.1261952](https://doi.org/10.1126/science.1261952).
- Andraut, D., N. Bolfan-Casanova, G. L. Nigro, M. A. Bouhifd, G. Garbarino, and M. Mezouar (2011). "Solidus and liquidus profiles of chondritic mantle: Implication for melting of the Earth across its history". In: *E&PSL* 304, pp. 251–259. DOI: [10.1016/j.epsl.2011.02.006](https://doi.org/10.1016/j.epsl.2011.02.006).
- Angelats i C, M., F. Forget, M. A. López-Valverde, and F. González-Galindo (2005). "The first Mars thermospheric general circulation model: The Martian atmosphere from the ground to 240 km". In: *Geophysical research letters* 32.4. DOI: [10.1029/2004gl021368](https://doi.org/10.1029/2004gl021368).
- Angelo, I. and R. Hu (2017). "A Case for an Atmosphere on Super-Earth 55 Cancri e". In: *AJ* 154.6, p. 232. DOI: [10.3847/1538-3881/aa9278](https://doi.org/10.3847/1538-3881/aa9278).
- Ballmer, M. D., D. L. Lourenço, K. Hirose, R. Caracas, and R. Nomura (2017). "Reconciling magma-ocean crystallization models with the present-day structure of the Earth's mantle". In: *GGG* 18.7, pp. 2785–2806. DOI: [10.1002/2017GC006917](https://doi.org/10.1002/2017GC006917).

- Baraffe, I., D. Homeier, F. Allard, and G. Chabrier (2015). "New evolutionary models for pre-main sequence and main sequence low-mass stars down to the hydrogen-burning limit". In: *A&A* 577, A42. DOI: [10.1051/0004-6361/201425481](https://doi.org/10.1051/0004-6361/201425481).
- Barboni, M., P. Boehnke, B. Keller, I. E. Kohl, B. Schoene, E. D. Young, and K. D. McKeegan (2017). "Early formation of the Moon 4.51 billion years ago". In: *SciA* 3.1, e1602365. DOI: [10.1126/sciadv.1602365](https://doi.org/10.1126/sciadv.1602365).
- Barrat, J. A., B. Zanda, F. Moynier, C. Bollinger, C. Liorzou, and G. Bayon (2012). "Geochemistry of CI chondrites: Major and trace elements, and Cu and Zn Isotopes". In: *GeCoA* 83, pp. 79–92. ISSN: 0016-7037. DOI: [10.1016/j.gca.2011.12.011](https://doi.org/10.1016/j.gca.2011.12.011).
- Bell, E. A., T. M. Harrison, I. E. Kohl, and E. D. Young (2014). "Eoarchean crustal evolution of the Jack Hills zircon source and loss of Hadean crust". In: *Geoch. Cosm. Acta* 146.1, pp. 27–42. DOI: [10.1016/j.gca.2014.09.028](https://doi.org/10.1016/j.gca.2014.09.028).
- Berg, G. and B. Bollmark (1985). "Retention of U and Pb in zircons from shocked granite in the Siljan impact structure, Sweden". In: *Earth and Planetary Science Letters* 74.4, pp. 347–349. DOI: [10.1016/S0012-821X\(85\)80006-6](https://doi.org/10.1016/S0012-821X(85)80006-6).
- Birkhoff, G., R. Bellman, and C. C. Lin, eds. (1960). *Proceedings of the 13th symposium in applied mathematics of the American Mathematical Society*. Vol. 13.
- Blass, A., X. Zhu, R. Verzicco, D. Lohse, and R. J. Stevens (2019). "Flow organization and heat transfer in turbulent wall sheared thermal convection". In: *arXiv preprint arXiv:1904.11400*.
- Boer, J. de, G. Salter, M. Benisty, A. Vigan, A. Boccaletti, P. Pinilla, C. Ginski, A. Juhasz, A.-L. Maire, S. Messina, et al. (2016). "Multiple rings in the transition disk and companion candidates around RX J1615. 3-3255-High contrast imaging with VLT/SPHERE". In: *Astronomy & Astrophysics* 595, A114. DOI: [10.1051/0004-6361/201629267](https://doi.org/10.1051/0004-6361/201629267).
- Boukaré, C.-E., B. Y. Ricard, and G. Fiquet (2015). "Thermodynamics of the MgO-FeO-SiO₂ system up to 140 GPa: Application to the crystallization of Earth's magma ocean". In: *JGRB* 120.9, pp. 6085–6101. DOI: [10.1002/2015JB011929](https://doi.org/10.1002/2015JB011929).
- Boukaré, C.-E. and Y. Ricard (Sept. 2017). "Modeling phase separation and phase change for magma ocean solidification dynamics". In: *Geochemistry, Geophysics, Geosystems* 18.9, pp. 3385–3404. DOI: [10.1002/2017gc006902](https://doi.org/10.1002/2017gc006902).
- Bouvier, A. and M. Wadhwa (2010). "The age of the Solar System redefined by the oldest Pb–Pb age of a meteoritic inclusion". In: *Nature Geoscience* 3.9, pp. 637–641. DOI: [10.1038/ngeo941](https://doi.org/10.1038/ngeo941).
- Bower, D. J., P. Sanan, and A. S. Wolf (2018). "Numerical solution of a non-linear conservation law applicable to the interior dy-

- namics of partially molten planets". In: *PEPI* 274, pp. 49–62. DOI: [10.1016/j.pepi.2017.11.004](https://doi.org/10.1016/j.pepi.2017.11.004).
- Braukmüller, N., F. Wombacher, C. Funk, and C. Münker (June 2019). "Earth's volatile element depletion pattern inherited from a carbonaceous chondrite-like source". In: *Nature Geoscience*. DOI: [10.1038/s41561-019-0375-x](https://doi.org/10.1038/s41561-019-0375-x).
- Burnham, C. W. (1975). "Water and magmas; a mixing model". In: *GeCoA* 39.8, pp. 1077–1084. DOI: [10.1016/0016-7037\(75\)90050-2](https://doi.org/10.1016/0016-7037(75)90050-2).
- Canup, R. M. (2004). "Dynamics of Lunar formation". In: *ARA&A* 42. doi: 10.1146/annurev.astro.41.082201.113457, pp. 441–475. DOI: [10.1146/annurev.astro.41.082201.113457](https://doi.org/10.1146/annurev.astro.41.082201.113457).
- Caroll, M. and J. R. Holloway (1994). *Volatiles in Magmas*. Ed. by Va. Mineralogical Society of America Fredericksburg. Vol. 30. Mineralogical Society of America, Fredericksburg, Va. DOI: [10.1515/9781501509674](https://doi.org/10.1515/9781501509674).
- Chen, B., X. Lai, J. Li, J. Liu, J. Zhao, W. Bi, E. E. Alp, M. Y. Hu, and Y. Xiao (2018). "Experimental constraints on the sound velocities of cementite Fe₃C to core pressures". In: *E&PSL* 494, pp. 164–171. ISSN: 0012-821X. DOI: [10.1016/j.epsl.2018.05.002](https://doi.org/10.1016/j.epsl.2018.05.002).
- Coradini, A., C. Federico, and P. Lanciano (1983). "Earth and Mars: early thermal profiles". In: *PEPI* 31.2, pp. 145–160. DOI: [10.1016/0031-9201\(83\)90106-1](https://doi.org/10.1016/0031-9201(83)90106-1).
- Costa, A., L. Caricchi, and N. Bagsdassarov (2009). "A model for the rheology of a particle-bearing suspensions and partially molten rocks". In: *GGG* 10, Q.03010. DOI: [doi:10.1029/2008GC002138](https://doi.org/10.1029/2008GC002138).
- D'Alessio, P., N. Calvet, L. Hartmann, J. Muzerolle, and M. Sitko (2004). "Models of accretion disks around young stars". In: *Symposium-International Astronomical Union*. Vol. 221. Cambridge University Press, pp. 403–410. DOI: [10.1017/S0074180900241831](https://doi.org/10.1017/S0074180900241831).
- Dasgupta, R and M. Hirschmann (2010). "The deep carbon cycle and melting in Earth's interior". In: *E&PSL* 298.1, pp. 1–13. DOI: [10.1016/j.epsl.2010.06.039](https://doi.org/10.1016/j.epsl.2010.06.039).
- Dauphas, N. (2017). "The isotopic nature of the Earth's accreting material through time". In: *Nature* 541.7638, p. 521. DOI: [10.1038/nature20830](https://doi.org/10.1038/nature20830).
- Davaille, A., A. Limare, F. Touitou, I. Kumagai, and J. Vatteville (2011). "Anatomy of a laminar starting thermal plume at high Prandtl number". In: *ExFl* 50.2, pp. 285–300. DOI: [10.1007/s00348-010-0924-y](https://doi.org/10.1007/s00348-010-0924-y).
- Davaille, A. and J. Vatteville (2005). "On the transient nature of mantle plumes". In: *Geophysical Research Letters* 32.14. DOI: [10.1029/2005GL023029](https://doi.org/10.1029/2005GL023029).
- Deguen, R., M. Landeau, and P. Olson (2014). "Turbulent metal-silicate mixing, fragmentation, and equilibration in magma oceans". In:

- Earth and Planetary Science Letters* 391, pp. 274–287. DOI: [10.1016/j.epsl.2014.02.007](#).
- Demory, B.-O., M. Gillon, J. de Wit, N. Madhusudhan, E. Bolmont, K. Heng, T. Kataria, N. Lewis, R. Hu, J. Krick, et al. (2016). “A map of the large day–night temperature gradient of a super-Earth exoplanet”. In: *Nature* 532.7598, p. 207. DOI: [10.1038/nature17169](#).
- Dingwell, D. (1996). “Volcanic dilemma: flow or blow?” In: *Sci* 273.5278, pp. 1054–1055. DOI: [10.1126/science.273.5278.1054](#).
- Dorn, C., N. R. Hinkel, and J. Venturini (2017). “Bayesian analysis of interiors of HD 219134b, Kepler-10b, Kepler-93b, CoRoT-7b, 55 Cnc e, and HD 97658b using stellar abundance proxies”. In: *A&A* 597, A38. DOI: [10.1051/0004-6361/201628749](#).
- Drążkowska, J. and Y. Alibert (2017). “Planetesimal formation starts at the snow line”. In: *Astronomy & Astrophysics* 608, A92. DOI: [10.1051/0004-6361/201731491](#).
- Einstein, A. (1906). “Eine neue bestimmung der moleküldimensionen”. In: *Annalen der Physik* 324.2, pp. 289–306. DOI: [10.1002/andp.200590008](#).
- Elkins-Tanton, L. T. (2008). “Linked magma ocean solidification and atmospheric growth for Earth and Mars”. In: *E&PSL* 271.1-4, pp. 181–191. DOI: [10.1016/j.epsl.2008.03.062](#).
- (May 2012). “Magma oceans in the inner solar system”. In: *AREPS* 40, pp. 113–139. DOI: [10.1146/annurev-earth-042711-105503](#).
- Endo, Y., Y. Ueno, S. Aoyama, and S. O. Danielache (2016). “Sulfur isotope fractionation by broadband UV radiation to optically thin SO₂ under reducing atmosphere”. In: *E&PSL* 453, pp. 9–22. DOI: [10.1016/j.epsl.2016.07.057](#).
- Fegley, B., N. S. Jacobson, J. P. Williams, J. M. C. Plane, L. Schaefer, and K. Lodders (2016). “Solubility of Rock in Steam Atmospheres of Planets”. In: *ApJ* 824.2, p. 103. DOI: [10.3847/0004-637x/824/2/103](#).
- Fegley, B. and L. Schaefer (2014). “Treatise on Geochemistry”. In: ed. by H. Holland and K. Turekian. Elsevier. Chap. 13.3 Chemistry of Earth’s earliest atmosphere, pp. 71–90. URL: [arXiv:1210.0270v1](#).
- Feulner, G. (May 2012). “The faint young Sun problem”. In: *Reviews of Geophysics* 50.2. DOI: [10.1029/2011rg000375](#).
- Fiquet, G., A. L. Auzende, J. Siebert, A. Corgne, H. Bureau, H. Ozawa, and G. Garbarino (2010). “Melting of Peridotite to 140 Gigapascals”. In: *Sci* 329, pp. 1516–1518. DOI: [10.1126/science.1192448](#).
- Fischer-Gödde, M. and T. Kleine (2017). “Ruthenium isotopic evidence for an inner Solar System origin of the late veneer”. In: *Nature* 541, pp. 525–527. DOI: [10.1038/nature21045](#).
- Flato, G. et al. (2013). *Evaluation of Climate Models*. In: *Climate Change 2013: The Physical Science Basis. Contribution of Working Group I to the Fifth Assessment Report of the Intergovernmental Panel on Climate*

- Change. 9.7 Climate Sensitivity and Climate Feedbacks*, page 817. Ed. by T. F. Stocker, D. Qin, G.-K. Plattner, M. Tignor, S.K. Allen, J. Boschung, A. Nauels, Y. Xia, V. Bex, and P. M. Midgley. Cambridge University Press, Cambridge, United Kingdom and New York, NY, USA. URL: https://www.ipcc.ch/site/assets/uploads/2018/02/WGIAR5_Chapter09_FINAL.pdf.
- Foley, S. F. and Z. Pintér (2018). "Chapter 1 - Primary Melt Compositions in the Earth's Mantle". In: *Magmas Under Pressure*. Ed. by Yoshio Kono and Chrystèle Sanloup. Elsevier, pp. 3–42. ISBN: 978-0-12-811301-1. DOI: [10.1016/B978-0-12-811301-1.00001-0](https://doi.org/10.1016/B978-0-12-811301-1.00001-0).
- Gaillard, F. and B. Scaillet (2014). "A theoretical framework for volcanic degassing chemistry in a comparative planetology perspective and implications for planetary atmospheres". In: *E&PSL* 403, Supplement C, pp. 307–316. ISSN: 0012-821X. DOI: [10.1016/j.epsl.2014.07.009](https://doi.org/10.1016/j.epsl.2014.07.009).
- Gaillard, F., B. Scaillet, M. Pichavant, and G. Iacono-Marziano (2015). "The redox geodynamics linking basalts and their mantle sources through space and time". In: *ChGeo* 418, pp. 217–233. DOI: [10.1016/j.chemgeo.2015.07.030](https://doi.org/10.1016/j.chemgeo.2015.07.030).
- Garufi, A., M. Benisty, T. Stolker, H. Avenhaus, J. De Boer, A. Pohl, S. P. Quanz, C. Dominik, C. Ginski, C. Thalmann, et al. (2017). "Three years of SPHERE: the latest view of the morphology and evolution of protoplanetary discs". In: *The Messenger* 169, 32. DOI: [10.18727/0722-6691/5036](https://doi.org/10.18727/0722-6691/5036). URL: [arXiv:1710.02795](https://arxiv.org/abs/1710.02795).
- Giordano, D. and D. Dingwell (2003). "Non-Arrhenian multicomponent melt viscosity: a model". In: *E&PSL* 208, pp. 337–349. DOI: [10.1016/S0012-821X\(03\)00042-6](https://doi.org/10.1016/S0012-821X(03)00042-6).
- Giordano, D., J. Russell, and D. Dingwell (2008). "Viscosity of magmatic liquids: A model". In: *E&PSL* 271, pp. 123–134. DOI: [10.1016/j.epsl.2008.03.038](https://doi.org/10.1016/j.epsl.2008.03.038).
- Glatzmaier, G. A. (2013). *Introduction to Modeling Convection in Planets and Stars: Magnetic Field, Density Stratification, Rotation*. Vol. 24. Princeton University Press. DOI: [10.23943/princeton/9780691141725.001.0001](https://doi.org/10.23943/princeton/9780691141725.001.0001).
- Goldblatt, C. (2015). "Habitability of Waterworlds: Runaway Greenhouses, Atmospheric Expansion, and Multiple Climate States of Pure Water Atmospheres". In: *AsBio* 15, 5, pp. 362–370. DOI: [10.1089/ast.2014.1268](https://doi.org/10.1089/ast.2014.1268).
- Goldblatt, C., T. D. Robinson, K. J. Zahnle, and D. Crisp (2013). "Low simulated radiation limit for runaway greenhouse climates". In: *NatGe* 6, 8, p. 661. DOI: [10.1038/ngeo1892](https://doi.org/10.1038/ngeo1892).
- Gómez-Leal, I., L. Kaltenegger, V. Lucarini, and F. Lunkeit (2018). "Climate sensitivity to carbon dioxide and the moist greenhouse threshold of earth-like planets under an increasing solar forcing". In: *The Astrophysical Journal* 869, 2, p. 129. DOI: [10.3847/1538-4357/aaba5f](https://doi.org/10.3847/1538-4357/aaba5f).

- Gough, D. (Sept. 1981). "Solar interior structure and luminosity variations". In: *ESA and European Physical Society, Proceedings of ES-LAB Symposium on Physics of Solar Variations, 14th, Scheveningen, Netherlands, Sept. 16-19, 1980. Solar Physics*. Vol. 74, pp. 21–34. DOI: [10.1007/978-94-010-9633-1_4](https://doi.org/10.1007/978-94-010-9633-1_4).
- Green, D. H., W. O. Hibberson, I. Kovács, and A. Rosenthal (2010). "Water and its influence on the lithosphere–asthenosphere boundary". In: *Nature*, pp. 448–451. DOI: [10.1038/nature09369](https://doi.org/10.1038/nature09369).
- Grossmann, S. and D. Lohse (2000). "Scaling in thermal convection: a unifying theory". In: *Journal of Fluid Mechanics* 407, pp. 27–56. DOI: [10.1017/s0022112099007545](https://doi.org/10.1017/s0022112099007545).
- (2003). "On geometry effects in Rayleigh-Benard convection". In: *JFM* 486, pp. 105–114. DOI: [10.1017/S0022112003004270](https://doi.org/10.1017/S0022112003004270).
- (2011). "Multiple scaling in the ultimate regime of thermal convection". In: *PhFl* 23.4, p. 045108. DOI: [10.1063/1.3582362](https://doi.org/10.1063/1.3582362).
- Güdel, M. (1997). "Are Coronae of Magnetically Active Stars Heated by Flares?" In: *ApJL* 480.2, p. L121. DOI: [10.1086/344614](https://doi.org/10.1086/344614).
- Haghighipour, N. and O. C. Winter (2016). "Formation of terrestrial planets in disks with different surface density profiles". In: *Celestial Mechanics and Dynamical Astronomy* 124.3, pp. 235–268. DOI: [10.1007/s10569-015-9663-y](https://doi.org/10.1007/s10569-015-9663-y).
- Hallis, L. J., G. R. Huss, K. Nagashima, G. J. Taylor, S. A. Halldórs-son, D. R. Hilton, M. J. Mottl, and K. J. Meech (2015). "Evidence for primordial water in Earth's deep mantle". In: *Sci* 350.6262, pp. 795–797. DOI: [10.1126/science.aac4834](https://doi.org/10.1126/science.aac4834).
- Hamano, K., Y. Abe, and H. Genda (2013). "Emergence of two types of terrestrial planet on solidification of magma ocean". In: *Nature* 497, pp. 607–610. DOI: [10.1038/nature12163](https://doi.org/10.1038/nature12163).
- Hamano, K., H. Kawahara, Y. Abe, M. Onishi, and G. L. Hashimoto (2015). "Lifetime and Spectral Evolution of a Magma Ocean with a Steam Atmosphere: Its Detectability by Future Direct Imaging". In: *ApJ* 806.2, p. 216. DOI: [10.1088/0004-637x/806/2/216](https://doi.org/10.1088/0004-637x/806/2/216).
- Hammond, M. and R. T. Pierrehumbert (2017). "Linking the Climate and Thermal Phase Curve of 55 Cancri e". In: *ApJ* 849.2, p. 152. DOI: [10.3847/1538-4357/aa9328](https://doi.org/10.3847/1538-4357/aa9328).
- Hansen, B. MS (2009). "Formation of the terrestrial planets from a narrow annulus". In: *The Astrophysical Journal* 703.1, p. 1131. DOI: [10.1088/0004-637x/703/1/1131](https://doi.org/10.1088/0004-637x/703/1/1131).
- Held, I. M. and B. J. Soden (2006). "Robust Responses of the Hydrological Cycle to Global Warming". In: *JCli* 19.21, pp. 5686–5699. DOI: [10.1175/JCLI3990.1](https://doi.org/10.1175/JCLI3990.1).
- Herzberg, C., P. Raterron, and J. Zhang (2000). "New experimental observations on the anhydrous solidus for peridotite KLB-1". In: *GGG* 1.11, p. 1051. DOI: [10.1029/2000GC000089](https://doi.org/10.1029/2000GC000089).

- Hier-Majumder, S. and Marc M Hirschmann (2017). “The origin of volatiles in the earth’s mantle”. In: *GGG* 18.8, pp. 3078–3092. DOI: [10.1002/2017GC006937](https://doi.org/10.1002/2017GC006937).
- Hirose, K., G. Morard, R. Sinmyo, K. Umemoto, J. Hernlund, G. Helffrich, and S. Labrosse (2017). “Crystallization of silicon dioxide and compositional evolution of the Earth’s core”. In: *Nature* 543.7643, p. 99. DOI: [10.1038/nature21367](https://doi.org/10.1038/nature21367).
- Hirschmann, M. (2000). “Mantle solidus: Experimental constraints and the effects of peridotite composition.” In: *GGG* 1.10. DOI: [10.1029/2000GC000070](https://doi.org/10.1029/2000GC000070).
- (2006). “Water, melting, and the deep Earth H₂O cycle”. In: *AREPS* 34, pp. 629–653. DOI: [10.1146/annurev.earth.34.031405.125211](https://doi.org/10.1146/annurev.earth.34.031405.125211).
- (2012). “Magma ocean influence on early atmosphere mass and composition”. In: *E&PSL* 341. Supplement C, pp. 48–57. DOI: [10.1016/j.epsl.2012.06.015](https://doi.org/10.1016/j.epsl.2012.06.015).
- Hirschmann, M. and R. Dasgupta (2009). “The H/C ratios of Earth’s near-surface and deep reservoirs, and consequences for deep Earth volatile cycles”. In: *ChGeo* 262.1–2, pp. 4–16. DOI: [10.1016/j.chemgeo.2009.02.008](https://doi.org/10.1016/j.chemgeo.2009.02.008).
- Hirschmann, M. and D. Kohlstedt (2012). “Water in Earth’s mantle”. In: *PhT* 65.3, pp. 40–45. DOI: [10.1063/PT.3.1476](https://doi.org/10.1063/PT.3.1476).
- Hoskin, P. W. O. (2005). “Trace-element composition of hydrothermal zircon and the alteration of Hadean zircon from the Jack Hills, Australia”. In: *Geoch. Cosm. Acta* 69.3, pp. 637–648. DOI: [10.1016/j.gca.2004.07.006](https://doi.org/10.1016/j.gca.2004.07.006).
- Humphries, R. J. and S. Nayakshin (2018). “Changes in the metallicity of gas giant planets due to pebble accretion”. In: *Monthly Notices of the Royal Astronomical Society* 477.1, pp. 593–615. DOI: [10.1093/mnras/sty569](https://doi.org/10.1093/mnras/sty569).
- Ikoma, M., L. Elkins-Tanton, K. Hamano, and J. Suckale (May 2018). “Water Partitioning in Planetary Embryos and Protoplanets with Magma Oceans”. In: *SSRv* 214.4, p. 76. ISSN: 1572-9672. DOI: [10.1007/s11214-018-0508-3](https://doi.org/10.1007/s11214-018-0508-3).
- Ingersoll, A. P. (2013). *Princeton Primers in Climate: Planetary Climates*. Ed. by A P Ingersoll. Princeton University Press. DOI: [10.23943/princeton/9780691145044.001.0001](https://doi.org/10.23943/princeton/9780691145044.001.0001).
- Izidoro, A. and S. N. Morbidelli A. and Raymond (2014). In: *The Astrophysical Journal* 794.1, p. 11. DOI: [10.1088/0004-637x/794/1/11](https://doi.org/10.1088/0004-637x/794/1/11).
- Jaupart, C. and J.-C. Mareschal (2011). *Heat generation and transport in the earth*. Cambridge University Press. DOI: [10.1017/cbo9780511781773.006](https://doi.org/10.1017/cbo9780511781773.006).
- Javoy, M. et al. (2010). “The chemical composition of the Earth: Enstatite chondrite models”. In: *E&PSL* 293.3, pp. 259–268. DOI: [10.1016/j.epsl.2010.02.033](https://doi.org/10.1016/j.epsl.2010.02.033).
- Johnstone, C. P., M. Güdel, H. Lammer, and K. G. Kislyakova (2018). “The Upper Atmospheres of Terrestrial Planets: Carbon Dioxide

- Cooling and the Earth's Thermospheric Evolution". In: *A&A*. DOI: [10.1051/0004-6361/201832776](https://doi.org/10.1051/0004-6361/201832776).
- Johnstone, C. P., M. Güdel, A. Stökl, H. Lammer, L. Tu, K. G. Kislyakova, T. Lüftinger, P. Odert, N. V. Erkaev, and E. A. Dorfi (2015). "The Evolution of Stellar Rotation and the Hydrogen Atmospheres of Habitable-zone Terrestrial Planets". In: *ApJL* 815.1, p. L12. DOI: [10.1016/j.icarus.2014.12.01](https://doi.org/10.1016/j.icarus.2014.12.01).
- Karato, A. I. and P. Wu (1993). "Rheology of the upper mantle: a synthesis". In: *Sci* 260, pp. 771–778. DOI: [10.1126/science.260.5109.771](https://doi.org/10.1126/science.260.5109.771).
- Karki, B. and L. Stixrude (2010). "Viscosity of MgSiO₃ Liquid at Earth's mantle conditions: Implications for an Early magma ocean". In: *Sci* 328.5979, pp. 740–742. DOI: [10.1126/science.118832](https://doi.org/10.1126/science.118832).
- Kasting, J. (1988). "Runaway and Moist Greenhouse Atmospheres and the Evolution of Earth and Venus." In: *Icar* 74, pp. 472–494. DOI: [10.1016/0019-1035\(88\)90116-9](https://doi.org/10.1016/0019-1035(88)90116-9).
- Katyal, N., A. Nikolaou, M. Godolt, J. L. Grenfell, N. Tosi, F. Schreier, and H. Rauer (2019). "Evolution and Spectral Response of a Steam Atmosphere for Early Earth with a coupled climate-interior model". In: *The Astrophysical Journal* 875.31. DOI: [10.3847/1538-4357/ab0d85](https://doi.org/10.3847/1538-4357/ab0d85).
- Katz, R. F., M. Spiegelman, and C. H. Langmuir (2003). "A new parameterization of hydrous mantle melting". In: *GGG* 4.9, p. 1073. DOI: [10.1029/2002GC000433](https://doi.org/10.1029/2002GC000433).
- Kessel, R., M. W. Schmidt, P. Ulmer, and T. Pettke (2005). "Trace element signature of subduction-zone fluids, melts and supercritical liquids at 120–180 km depth". In: *Nature* 437.7059, p. 724. DOI: [10.1038/nature03971](https://doi.org/10.1038/nature03971).
- King, E., J. W. Valley, D. W. Davis, and G. Edwards (1998). "Oxygen isotope ratios of Archean plutonic zircons from granite–greenstone belts of the Superior Province: indicator of magmatic source". In: *Precambrian Res.* 92, pp. 365–387. DOI: [10.1016/S0301-9268\(98\)00082-5](https://doi.org/10.1016/S0301-9268(98)00082-5).
- Kite, E. S., B. Fegley Jr, L. Schaefer, and E. Gaidos (2016). "Atmosphere-interior Exchange on Hot, Rocky Exoplanets". In: *ApJ* 828.2, p. 80. DOI: [10.1016/0022-4073\(67\)90070-2](https://doi.org/10.1016/0022-4073(67)90070-2).
- Klahr, H. and W. Brandner (2006). *Planet formation: theory, observations, and experiments*. Vol. 1. Cambridge University Press. DOI: [10.1017/cbo9780511536571](https://doi.org/10.1017/cbo9780511536571).
- Kobayashi, H., H. Takahashi, and Y. Hiki (2000). "Viscosity of glasses near and below the glass transition temperature." In: *JAP* 88.6, pp. 3776–3778. DOI: [10.1063/1.1286107](https://doi.org/10.1063/1.1286107).
- Kondratyev, K. Y. (1969a). "Radiation in the Atmosphere". In: ed. by J. V. Miegham. Vol. 12. International Geophysics series. Academic Press, Inc. Chap. Chapter 1 - Radiant energy. The main concepts and definitions. Pp. 1–48. URL: <https://www.elsevier.com>.

- [com/books/radiation-in-the-atmosphere/kondratyev/978-0-12-419050-4](https://www.elsevier.com/books/radiation-in-the-atmosphere/kondratyev/978-0-12-419050-4).
- (1969b). “Radiation in the Atmosphere”. In: ed. by J. V. Miegham. Vol. 12. International Geophysics series. Academic Press, Inc. Chap. Chapter 3 - Radiation absorption in the atmosphere. Pp. 85–159. URL: <https://www.elsevier.com/books/radiation-in-the-atmosphere/kondratyev/978-0-12-419050-4>.
- Kono, Y. (2018). “Chapter 10 - Viscosity Measurement”. In: *Magma Under Pressure*. Ed. by Yoshio Kono and Chrystèle Sanloup. Elsevier, pp. 261–280. ISBN: 978-0-12-811301-1. DOI: [10.1016/B978-0-12-811301-1.00010-1](https://doi.org/10.1016/B978-0-12-811301-1.00010-1).
- Kono, Y., C. Kenney-Benson, Y. Shibazaki, C. Park, G. Shen, and Y. Wang (2015). “High-pressure viscosity of liquid Fe and FeS revisited by falling sphere viscometry using ultrafast X-ray imaging”. In: *Physics of the Earth and Planetary Interiors* 241, pp. 57–64. DOI: [10.1016/j.pepi.2015.02.006](https://doi.org/10.1016/j.pepi.2015.02.006).
- Kono, Y., C. Park, C. Kenney-Benson, G. Shen, and Y. Wang (2014). “Toward comprehensive studies of liquids at high pressures and high temperatures: Combined structure, elastic wave velocity, and viscosity measurements in the Paris–Edinburgh cell”. In: *Physics of the Earth and Planetary Interiors* 228, pp. 269–280. DOI: [10.1016/j.pepi.2013.09.006](https://doi.org/10.1016/j.pepi.2013.09.006).
- Kraichnan, R. H. (1962). “Turbulent thermal convection at arbitrary Prandtl number”. In: *The Physics of Fluids* 5.11, pp. 1374–1389. DOI: [10.1063/1.1706533](https://doi.org/10.1063/1.1706533).
- Kretzschmar, H.-J., I. Jähne, S. Herrmann, and M. Kunick (2019). *Steam Properties Calculator*. 2011–2019. Zittau/Görlitz University of Applied Sciences. URL: <http://www.steam-properties-calculator.com>.
- Kröner, A. (1985). “Evolution of the Archean continental crust”. In: *Annual Review of Earth and Planetary Sciences* 13.1, pp. 49–74. DOI: [10.1146/annurev.ea.13.050185.000405](https://doi.org/10.1146/annurev.ea.13.050185.000405).
- Kurokawa, H., J. Foriel, M. Laneuville, C. Houser, and T. Usui (2018). “Subduction and atmospheric escape of Earth’s seawater constrained by hydrogen isotopes”. In: *E&PSL* 497, pp. 149–160. DOI: [10.1016/j.epsl.2018.06.016](https://doi.org/10.1016/j.epsl.2018.06.016).
- Labrosse, S., J. W. Hernlund, and N. Coltice (2007). “A crystallizing dense magma ocean at the base of the Earth’s mantle”. In: *Nature* 450, pp. 866–869. DOI: [10.1038/nature06355](https://doi.org/10.1038/nature06355).
- Lammer, H., J. F. Kasting, E. Chassefière, R. E. Johnson, Y. N. Kulikov, and F. Tian (2008). “Atmospheric escape and evolution of terrestrial planets and satellites”. In: *SSRv* 139.1-4, pp. 399–436. DOI: [10.1007/s11214-008-9413-5](https://doi.org/10.1007/s11214-008-9413-5).
- Lammer, H. et al. (2013). “Outgassing history and escape of the martian atmosphere and water inventory”. In: *SSRv* 174.1-4, pp. 113–154. DOI: [10.1007/s11214-012-9943-8](https://doi.org/10.1007/s11214-012-9943-8).

- Lammer, H. et al. (May 2018). "Origin and evolution of the atmospheres of early Venus, Earth and Mars". In: *A&ARv* 26.1, p. 2. ISSN: 1432-0754. DOI: [10.1007/s00159-018-0108-y](https://doi.org/10.1007/s00159-018-0108-y).
- Laneuville, M., J. Hernlund, S. Labrosse, and N. Guttenberg (2018). "Crystallization of a compositionally stratified basal magma ocean". In: *Physics of the Earth and Planetary Interiors* 276, pp. 86–92. DOI: [10.1016/j.pepi.2017.07.007](https://doi.org/10.1016/j.pepi.2017.07.007).
- Le Bas, M. J., R. W. Le Maitre, A. Streckeisen, and B. Zanettin (1986). "A chemical classification of volcanic rocks based on the total alkali silica diagram". In: *JPet* 27.3, pp. 745–750. DOI: [10.1093/petrology/27.3.745](https://doi.org/10.1093/petrology/27.3.745).
- Lebrun, T., H. Massol, E. Chassefière, A. Davaille, E. Marcq, P. Sarda, F. Leblanc, and G. Brandeis (2013). "Thermal evolution of an early magma ocean in interaction with the atmosphere". In: *JGRE* 118.6, pp. 1155–1176. DOI: [10.1002/jgre.20068](https://doi.org/10.1002/jgre.20068).
- Leconte, J., F. Forget, B. Charnay, R. Wordsworth, and A. Pottier (2013). "Increased insolation threshold for runaway greenhouse processes on Earth-like planets". In: *Nature* 504.7479, p. 268. DOI: [10.1038/nature12827](https://doi.org/10.1038/nature12827).
- Lohse, D. and F. Toschi (2003). "Ultimate state of thermal convection". In: *PhRvL* 90.3, p. 034502. DOI: [10.1103/PhysRevLett.90.034502](https://doi.org/10.1103/PhysRevLett.90.034502).
- Lupu, R. E., K. Zahnle, M. S. Marley, L. Schaefer, B. Fegley, C. Morley, K. Cahoy, R. Freedman, and J. J. Fortney (2014). "The Atmospheres of Earthlike Planets after Giant Impact Events". In: *ApJ* 784.1, p. 27. DOI: [10.1006/icar.1999.6201](https://doi.org/10.1006/icar.1999.6201).
- Maas, C. and U. Hansen (2015). "Effects of Earth's rotation on the early differentiation of a terrestrial magma ocean". In: *JGR* 120.11, pp. 7508–7525. DOI: [10.1002/2015JB012053](https://doi.org/10.1002/2015JB012053).
- (2019). "Dynamics of a terrestrial magma ocean under planetary rotation: A study in spherical geometry". In: *Earth and Planetary Science Letters* 513, pp. 81–94. DOI: [10.1016/j.epsl.2019.02.016](https://doi.org/10.1016/j.epsl.2019.02.016).
- Madhusudhan, N., H. Knutson, J. Fortney, and T. Barman (2014). "Protostars and Planets VI". In: ed. by H. Beuther, R. Klessen, C. Dullemond, and T. Henning. University of Arizona Press. Chap. Exoplanetary atmospheres. DOI: [10.2458/azu_uapress_9780816531240-ch032](https://doi.org/10.2458/azu_uapress_9780816531240-ch032).
- Makhluf, A. R., R. C. Newton, and C. E. Manning (2017). "Experimental determination of liquidus H₂O contents of haplogranite at deep-crustal conditions". In: *CoMP* 172.9, p. 77. DOI: [10.1007/s00410-017-1392-7](https://doi.org/10.1007/s00410-017-1392-7).
- Mamajek, Eric E. (2009). "Initial Conditions of Planet Formation: Lifetimes of Primordial Disks". In: 1158.1, pp. 3–10. DOI: [10.1063/1.3215910](https://doi.org/10.1063/1.3215910).
- Manning, C. E. (2018). "Chapter 3 - The Influence of Pressure on the Properties and Origins of Hydrous Silicate Liquids in Earth's Interior". In: *Magma Under Pressure*. Ed. by Y. Kono and Chrys-

- téle Sanloup. Elsevier, pp. 83–113. ISBN: 978-0-12-811301-1. DOI: [10.1016/B978-0-12-811301-1.00003-4](https://doi.org/10.1016/B978-0-12-811301-1.00003-4).
- Marchi, S., B. A. Black, L. T. Elkins-Tanton, and W. F. Bottke (2016). “Massive impact-induced release of carbon and sulfur gases in the early Earth’s atmosphere”. In: *E&PSL* 449, pp. 96–104. DOI: [10.1016/j.epsl.2016.05.032](https://doi.org/10.1016/j.epsl.2016.05.032).
- Marcq, E. (2012). “A simple 1-D radiative-convective atmospheric model designed for integration into coupled models of magma ocean planets”. In: *JGRE* 117.E1, E01001. DOI: [10.1029/2011JE003912](https://doi.org/10.1029/2011JE003912).
- Marcq, E., A. Salvador, H. Massol, and A. Davaille (2017). “Thermal radiation of magma ocean planets using a 1-D radiative-convective model of H₂O-CO₂ atmospheres”. In: *JGRE* 122.7, pp. 1539–1553. DOI: [10.1002/2016JE005224](https://doi.org/10.1002/2016JE005224).
- Marsh, B. D. (1981). “On the Crystallinity, Probability of Occurrence, and Rheology of Lava and Magma”. In: *CoMP* 78, pp. 85–98. DOI: [10.1007/BF00371146](https://doi.org/10.1007/BF00371146).
- Massol, H. et al. (2016). “Formation and Evolution of Protoatmospheres”. In: *SSRv* 205.1–4, pp. 153–211. DOI: [10.1007/s11214-016-0280-1](https://doi.org/10.1007/s11214-016-0280-1).
- Maurice, M., N. Tosi, H. Samuel, A.-C. Plesa, C. Hüttig, and D. Breuer (2017). “Onset of solid-state mantle convection and mixing during magma ocean solidification”. In: *JGRE* 122.3, pp. 577–598. DOI: [10.1002/2016JE005250](https://doi.org/10.1002/2016JE005250).
- Melosh, H. J. (1990). “Giant impacts and the thermal state of the early Earth”. In: *Origin of the Earth* 1, pp. 69–83.
- Mibe, K., T. Kawamoto, K. N. Matsukage, Y. Fei, and S. Ono (2011). “Slab melting versus slab dehydration in subduction-zone magmatism”. In: *PNAS* 108.20, pp. 8177–8182. DOI: [10.1073/pnas.1010968108](https://doi.org/10.1073/pnas.1010968108).
- Misra, A., V. Meadows, M. Claire, and D. Crisp (2014). “Using dimers to measure biosignatures and atmospheric pressure for terrestrial exoplanets”. In: *AsBio* 14.2, pp. 67–86. DOI: [10.1089/ast.2013.0990](https://doi.org/10.1089/ast.2013.0990).
- Miyazaki, Y. and J. Korenaga (Apr. 2019a). “On the Timescale of Magma Ocean Solidification and Its Chemical Consequences: 1. Thermodynamic Database for Liquid at High Pressures”. In: *Journal of Geophysical Research: Solid Earth*. DOI: [10.1029/2018jb016932](https://doi.org/10.1029/2018jb016932).
- (Apr. 2019b). “On the Timescale of Magma Ocean Solidification and Its Chemical Consequences: 2. Compositional Differentiation Under Crystal Accumulation and Matrix Compaction”. In: *Journal of Geophysical Research: Solid Earth*. DOI: [10.1029/2018jb016928](https://doi.org/10.1029/2018jb016928).
- Mojzsis, S. J., M. Harrison, and R. T. Pidgeon (2001). “Oxygen-isotope evidence from ancient zircons for liquid water at the Earth’s surface 4,300 Myr ago”. In: *Nature* 409. DOI: [10.1038/35051557](https://doi.org/10.1038/35051557).

- Monteux, J., D. Andraut, and H. Samuel (2016). "On the cooling of a deep terrestrial magma ocean". In: *E&PSL* 448.Supplement C, pp. 140–149. DOI: [10.1016/j.epsl.2016.05.010](https://doi.org/10.1016/j.epsl.2016.05.010).
- Morbidelli, A., H. F. Levison, K. Tsiganis, and R. Gomes (2005). "Chaotic capture of Jupiter's Trojan asteroids in the early Solar System." In: *Natur* 435, pp. 462–465. DOI: [10.1038/nature03540](https://doi.org/10.1038/nature03540).
- Nakajima, S., Y.-Y. Hayashi, and Y. Abe (1992). "A study on the "run-away greenhouse effect" with a one dimensional radiative-convective equilibrium model." In: *J. Atmos. Sci.* 49.23, pp. 2256–2266. DOI: [10.1175/1520-0469\(1992\)049<2256:ASOTGE>2.0.CO;2](https://doi.org/10.1175/1520-0469(1992)049<2256:ASOTGE>2.0.CO;2).
- Nayakshin, Sergei (2011). "Formation of terrestrial planet cores inside giant planet embryos". In: *Monthly Notices of the Royal Astronomical Society* 413.2, pp. 1462–1478. DOI: [10.1111/j.1365-2966.2011.18230.x](https://doi.org/10.1111/j.1365-2966.2011.18230.x).
- Niemela, J. J., L. Skrbek, K. R. Sreenivasan, and R. J. Donnelly (2000a). "Erratum: Turbulent convection at very high Rayleigh numbers". In: *Nature* 406.6794, p. 439. DOI: [10.1038/35019124](https://doi.org/10.1038/35019124).
- (2000b). "Turbulent convection at very high Rayleigh numbers". In: *Nature* 404.6780, p. 837. DOI: [10.1038/35009036](https://doi.org/10.1038/35009036).
- Nikolaou, A., N. Katyal, N. Tosi, M. Godolt, J. L. Grenfell, and H. Rauer (2019). "What Factors Affect the Duration and Outgassing of the Terrestrial Magma Ocean?" In: *ApJ* 875.1, p. 11. DOI: [10.3847/1538-4357/ab08ed](https://doi.org/10.3847/1538-4357/ab08ed).
- Noack, L., D. Breuer, and T. Spohn (2012). "Coupling the atmosphere with interior dynamics: Implications for the resurfacing of Venus". In: *Icar* 217, pp. 484–498. DOI: [10.1016/j.icarus.2011.08.026](https://doi.org/10.1016/j.icarus.2011.08.026).
- Odert, P., H. Lammer, N. V. Erkaev, A. Nikolaou, H. I. M. Lichtenegger, C. P. Johnstone, K. G. Kislyakova, M. Leitzinger, and N. Tosi (2018). "Escape and fractionation of volatiles and noble gases from Mars-sized planetary embryos and growing protoplanets". In: *Icarus* 307, pp. 327–346. DOI: [10.1016/j.icarus.2017.10.031](https://doi.org/10.1016/j.icarus.2017.10.031).
- Olson, P. and Z. D. Sharp (2018). "Hydrogen and helium ingassing during terrestrial planet accretion". In: *Earth and Planetary Science Letters* 498, pp. 418–426. DOI: [10.1016/j.epsl.2018.07.006](https://doi.org/10.1016/j.epsl.2018.07.006).
- Pan, V., J. R. Holloway, and Hervig R L (1991). "The pressure and temperature dependence of carbon dioxide solubility in tholeiitic basalt melts". In: *GeCoA* 55, pp. 1587–1595. DOI: [10.1016/0016-7037\(91\)90130-W](https://doi.org/10.1016/0016-7037(91)90130-W).
- Parfitt, A. and L. Wilson (2008). *Fundamentals of physical volcanology*. Ed. by A. Parfitt and L. Wilson. Blackwell. DOI: [10.1111/j.1475-4959.2008.292_7.x](https://doi.org/10.1111/j.1475-4959.2008.292_7.x).
- Peck, W. H., J. W. Valley, S. A. Wilde, and C. M. Graham (2001). "Oxygen isotope ratios and rare earth elements in 3.3 to 4.4 Ga zircons: Ion microprobe evidence for high $\delta^{18}\text{O}$ continental crust and oceans in the Early Archean". In: *Geoch. Cosm. Acta* 65.22, pp. 4215–4229. DOI: [10.1016/s0016-7037\(01\)00711-6](https://doi.org/10.1016/s0016-7037(01)00711-6).

- Perchuk, L. L. and I. Kushiro (1991). "Thermodynamics of the Liquidus in the System Diopside—Water: A Review". In: *Physical Chemistry of Magmas*. Ed. by Leonid L. Perchuk and Ikuo Kushiro. New York, NY: Springer New York, pp. 249–267. ISBN: 978-1-4612-3128-8. DOI: [10.1007/978-1-4612-3128-8_9](https://doi.org/10.1007/978-1-4612-3128-8_9).
- Persikov, E. S., V. A. Zharikov, and P. G. Bukhtiyarov (1990). "The effect of volatiles on the properties of magmatic melts". In: *European Journal of Mineralogy*, pp. 621–642. DOI: [10.1127/ejm/2/5/0621](https://doi.org/10.1127/ejm/2/5/0621).
- Pierrehumbert, R. T. (2010). *Principles of Planetary climate*. Ed. by R T Pierrehumbert. Cambridge University Press. DOI: [10.1017/cbo9780511780783](https://doi.org/10.1017/cbo9780511780783).
- Plass, G. N. (1956). "The influence of the 15μ carbon-dioxide band on the atmospheric infra-red cooling rate". In: *Quarterly Journal of the Royal Meteorological Society* 82.353, pp. 310–324. DOI: [10.1002/qj.49708235307](https://doi.org/10.1002/qj.49708235307).
- Pluriel, W., E. Marcq, and M. Turbet (2019). "Modeling the albedo of Earth-like magma ocean planets with H₂O-CO₂ atmospheres". In: *Icarus* 317, pp. 583–590. DOI: [10.1016/j.icarus.2018.08.023](https://doi.org/10.1016/j.icarus.2018.08.023).
- Pujol and North (2003). "Analytical investigation of the atmospheric radiation limits in semigray atmospheres in radiative equilibrium". In: *Tell* 55.A, pp. 328–337. DOI: [10.3402/tellusa.v55i4.12101](https://doi.org/10.3402/tellusa.v55i4.12101).
- Rauer, H. et al. (Nov. 2014). "The PLATO 2.0 mission". In: *ExA* 38.1, pp. 249–330. ISSN: 1572-9508. DOI: [10.1007/s10686-014-9383-4](https://doi.org/10.1007/s10686-014-9383-4).
- Rayleigh, Lord (1900). *Scientific Papers, Vol. II, p. 200*. Cambridge University Press.
- Raymond, S. N. and A. Izidoro (2017). "Origin of water in the inner Solar System: Planetesimals scattered inward during Jupiter and Saturn's rapid gas accretion". In: *Icar* 297, pp. 134–148. DOI: [10.1016/j.icarus.2017.06.030](https://doi.org/10.1016/j.icarus.2017.06.030).
- Raymond, S. N., T. Quinn, and J. I. Lunine (2006). "High-resolution simulations of the final assembly of Earth-like planets I. Terrestrial accretion and dynamics". In: *Icar* 183.2, pp. 265–282. DOI: [10.1016/j.icarus.2006.03.011](https://doi.org/10.1016/j.icarus.2006.03.011).
- Read, P. (2009). "Fluid dynamics: Rotating convection on the edge". In: *Natur* 457, pp. 270–271. DOI: [10.1038/457270a](https://doi.org/10.1038/457270a).
- Rems project, team and Studio Strings Software (2013). *REMS Mars Weather application*. Centro de Astrobiología, CSIC-INTA REMS/MSL 2013 (CAB).
- Roscoe, R. (1952). "The viscosity of suspensions of rigid spheres". In: *BJAP* 3.8, pp. 267–269. DOI: [10.1088/0508-3443/3/8/306](https://doi.org/10.1088/0508-3443/3/8/306).
- Rosby, H. T. (1965). "On thermal convection driven by non-uniform heating from below: an experimental study". In: *Deep Sea Research and Oceanographic Abstracts* 12.1, pp. 9–16. DOI: [10.1016/0011-7471\(65\)91336-7](https://doi.org/10.1016/0011-7471(65)91336-7).

- Rossum, G. van and F. L. Drake (2001). *Python Reference Manual*. Python-Labs. Virginia, USA Available at <http://www.python.org>. URL: <http://www.python.org>.
- Rothman, L. S. et al. (2013). "The HITRAN2012 molecular spectroscopic database". In: *JQSRT* 130, pp. 4–50. DOI: [10.1016/j.jqsrt.2013.07.002](https://doi.org/10.1016/j.jqsrt.2013.07.002).
- Rubie, D. C. (2015). "'9.03 - Formation of the Earth's Core'". In: *Treatise on Geophysics (Second Edition)*. Ed. by Gerald Schubert. Second Edition. Elsevier, pp. 43–79. DOI: [10.1016/B978-0-444-53802-4.00154-8](https://doi.org/10.1016/B978-0-444-53802-4.00154-8).
- Ruedas, T. (2017). "Radioactive heat production of six geologically important nuclides". In: *GGG* 18.9, pp. 3530–3541. DOI: [10.1002/2017GC006997](https://doi.org/10.1002/2017GC006997).
- Safronov, V. S. (1972). *Evolution of the protoplanetary cloud and formation of the earth and the planets*. Academy of Sciences of the USSR. DOI: [10.1007/978-94-011-1154-6_2](https://doi.org/10.1007/978-94-011-1154-6_2).
- Sakamaki, T., A. Suzuki, E. Ohtani, H. Terasaki, S. Urakawa, Y. Katayama, K. Funakoshi, Y. Wang, J. W. Hernlund, and M. D. Ballmer (2013). "Ponded melt at the boundary between the lithosphere and asthenosphere". In: *Nature Geoscience* 6.12, p. 1041. DOI: [10.1038/ngeo1982](https://doi.org/10.1038/ngeo1982).
- Sakuraba, H., H. Kurokawa, and H. Genda (2019). "Impact degassing and atmospheric erosion on Venus, Earth, and Mars during the late accretion". In: *Icarus* 317, pp. 48–58. DOI: [10.1016/j.icarus.2018.05.035](https://doi.org/10.1016/j.icarus.2018.05.035).
- Salvador, A., H. Massol, A. Davaille, E. Marcq, P. Sarda, and E. Chassefière (2017). "The relative influence of H₂O and CO₂ on the primitive surface conditions and evolution of rocky planets". In: *JGRE* 122.7, pp. 1458–1486. DOI: [10.1002/2017JE005286](https://doi.org/10.1002/2017JE005286).
- Schaefer, L. and B. Fegley (2010). "Chemistry of atmospheres formed during accretion of the Earth and other terrestrial planets". In: *Icarus* 208.1, pp. 438–448. ISSN: 0019-1035.
- (2017). "Redox States of Initial Atmospheres Outgassed on Rocky Planets and Planetesimals". In: *ApJ* 843.2, p. 120. DOI: [10.3847/1538-4357/aa784f](https://doi.org/10.3847/1538-4357/aa784f).
- Schaefer, L., R. Wordsworth, Z. Berta-Thompson, and D. Sasselov (2016). "Predictions of the Atmospheric Composition of GJ 1132b". In: *ApJ* 829.2, p. 63. DOI: [10.3847/0004-637x/829/2/63](https://doi.org/10.3847/0004-637x/829/2/63).
- Schreier, F., S. G. Garcia, P. Hedelt, M. Hess, J. Mendrok, M. Vasquez, and J. Xu (2014). "GARLIC— A general purpose atmospheric radiative transfer line-by-line infrared-microwave code: Implementation and evaluation". In: *J. Quant. Spectrosc. Radiat. Transfer* 137, pp. 29–50. DOI: [10.1016/j.jqsrt.2013.11.018](https://doi.org/10.1016/j.jqsrt.2013.11.018).
- Schubert, G., D. L. Turcotte, and P. Olson (2001). *Mantle Convection in the Earth and Planets*. Cambridge University Press. DOI: [10.1017/CB09780511612879](https://doi.org/10.1017/CB09780511612879).

- Shishkina, O. (2016). "Momentum and heat transport scalings in laminar vertical convection". In: *PhRvE* 93.5, p. 051102. DOI: [10.1103/physreve.93.051102](#).
- Shishkina, O., S. Grossmann, and D. Lohse (2016). "Heat and momentum transport scalings in horizontal convection". In: *Geophysical Research Letters* 43.3, pp. 1219–1225. DOI: [10.1002/2015GL067003](#).
- Shraiman, B. I. and E. D. Siggia (1990). "Heat transport in high-Rayleigh-number convection". In: *Physical Review A* 42.6, p. 3650. DOI: [10.1103/PhysRevA.42.3650](#).
- Siggia, E. D. (1994). "High Rayleigh number convection". In: *Annual review of fluid mechanics* 26.1, pp. 137–168. DOI: [10.1146/annurev.fluid.26.1.137](#).
- Sleep, N. H., K. J. Zahnle, and R. E. Lupu (2014). "Terrestrial aftermath of the Moon-forming impact". In: *RSPTA* 372.2024. ISSN: 1364-503X. DOI: [10.1098/rsta.2013.0172](#).
- Solomatov, V. (2007). "Treatise on Geophysics". In: ed. by G.. Schubert. Elsevier. Chap. Magma ocean and primordial mantle differentiation, pp. 91–119. DOI: [10.1016/b978-044452748-6.00141-3](#).
- Solomatov, V. and D. Stevenson (1993a). "Kinetics of crystal growth in a terrestrial magma ocean". In: *JGR* 98.E3, pp. 5407–5418. DOI: [10.1029/92je02839](#).
- (1993b). "Suspension in convective layers and style of differentiation of a terrestrial magma ocean". In: *JGR* 98.E3, pp. 5375–5390. DOI: [10.1029/92je02948](#).
- Speedy, R. J. (2003). "Kauzmann's paradox and the glass transition". In: *Biophys. Chem.* 105.2-3, pp. 411–420. DOI: [10.1016/s0301-4622\(03\)00105-4](#).
- Stixrude, L., N. de Koker, N. Sun, M. Mookherjee, and B. B. Karki (2009). "Thermodynamics of silicate liquids in the deep Earth". In: *E&PSL* 278.3-4, pp. 226–232. DOI: [10.1016/j.epsl.2008.12.006](#).
- Stolper, E. (1982). "The speciation of water in silicate melts". In: *GeCoA* 46.12, pp. 2609–2620. DOI: [10.1016/0016-7037\(82\)90381-7](#).
- Tasker, E., J. Tan, K. Heng, S. Kane, D. Spiegel, and the ELSI Origins Network Planetary Diversity Workshop (2017). "The language of exoplanet ranking metrics needs to change". In: *NatAs* 1.2, p. 42. DOI: [10.1038/s41550-017-0042](#).
- Tonks, W. B. and H. J. Melosh (1993). "Magma ocean formation due to giant impacts". In: *Journal of Geophysical Research: Planets* 98.E3, pp. 5319–5333. DOI: [10.1029/92JE02726](#).
- Tosi, N., M. Godolt, B. Stracke, T. Ruedas, J. L. Grenfell, D. Höning, A. Nikolaou, A.-C. Plesa, D. Breuer, and T. Spohn (2017). "The habitability of a stagnant-lid Earth". In: *A&A* 605.A71. DOI: [10.1051/0004-6361/201730728](#).
- Tschauner, O. et al. (Mar. 2018). "Ice-VII inclusions in diamonds: Evidence for aqueous fluid in Earth's deep mantle". In: *Science* 359.6380, pp. 1136–1139. DOI: [10.1126/science.aao3030](#).

- Tsiganis, K., R. Gomes, A. Morbidelli, and H. F. Levison (2005). "Origin of the orbital architecture of the giant planets of the Solar System". In: *Natur* 435, p. 459. DOI: [10.1038/nature03539](https://doi.org/10.1038/nature03539).
- Tu, L., C. P. Johnstone, M. Güdel, and H. Lammer (2015). "The extreme ultraviolet and X-ray Sun in Time: High-energy evolutionary tracks of a solar-like star". In: *A&A* 577, p. L3. DOI: [10.1051/0004-6361/201526146](https://doi.org/10.1051/0004-6361/201526146).
- Turcotte, D. L. and G. Schubert (2002). *Geodynamics*. Cambridge University Press. DOI: [10.1017/cbo9780511807442](https://doi.org/10.1017/cbo9780511807442).
- Turrini, D. et al. (Jan. 2018). "The contribution of the ARIEL space mission to the study of planetary formation". In: *ExA* 46.1, pp. 45–65. ISSN: 1572-9508. DOI: [10.1007/s10686-017-9570-1](https://doi.org/10.1007/s10686-017-9570-1).
- Ueno, Y., M. S. Johnson, S. O. Danielache, C. Eskebjerg, A. Pandey, and N. Yoshida (2009). "Geological sulfur isotopes indicate elevated OCS in the Archean atmosphere, solving faint young sun paradox". In: *PNAS* 106.35, pp. 14784–14789. DOI: [10.1073/pnas.0903518106](https://doi.org/10.1073/pnas.0903518106).
- Unterborn, C. T., S. J. Desch, N. R. Hinkel, and A. Lorenzo (2018). "Inward migration of the TRAPPIST-1 planets as inferred from their water-rich compositions". In: *NatAs* 2.4, pp. 297–302. DOI: [10.1038/s41550-018-0411-6](https://doi.org/10.1038/s41550-018-0411-6).
- Urbain, G., Y. Bottinga, and P. Richet (1982). "Viscosity of liquid silica, silicates and alumino-silicates". In: *GeCoA* 46, pp. 1061–1072. DOI: [10.1016/0016-7037\(82\)90059-x](https://doi.org/10.1016/0016-7037(82)90059-x).
- Valley, J. W., W. H. Peck, E. M. King, and S. A. Wilde (2002). "A cool Early Earth?" In: *Geo* 30, pp. 351–354. DOI: [10.1038/scientificamerican1005-58](https://doi.org/10.1038/scientificamerican1005-58).
- Wang, H. S., C. H. Lineweaver, and T. R. Ireland (2019). "The volatility trend of protosolar and terrestrial elemental abundances". In: *Icarus* 328, pp. 287–305. DOI: [10.1016/j.icarus.2019.03.018](https://doi.org/10.1016/j.icarus.2019.03.018).
- Watson, E. B. and T. M. Harrison (2005). "Zircon Thermometer Reveals Minimum Melting Conditions on Earliest Earth". In: *Science* 308.5723, pp. 841–844. DOI: [10.1126/science.1110873](https://doi.org/10.1126/science.1110873).
- Wetherill, G. W. (1990). "Formation of the Earth". In: *Annual Review of Earth and Planetary Sciences* 18.1, pp. 205–256. DOI: [0.1146/annurev.earth.18.1.205](https://doi.org/10.1146/annurev.earth.18.1.205).
- Wood, J. A., J. S. Jr Dickey, U. B. Marvin, and B. N. Powell (1970). "Lunar anorthosites and a geophysical model of the Moon". In: *Proceedings of the Apollo 11 Lunar Science Conference*. Ed. by A.A. Levinson. Vol. 1. New York: Pergammon Press, pp. 965–988.
- Woolley, H. W. (1980). "Thermodynamic properties for H₂O in the ideal gas state". In: *Water and Steam: Their Properties and Current Industrial Applications, Proceedings of the 9th International Conference on the Properties of Water and Steam*. Pergamon Press, New York, pp. 166–175.

- Wordsworth, R. and R. T. Pierrehumbert (2013a). "Hydrogen-Nitrogen Greenhouse Warming in Earth's Early Atmosphere". In: *Sci* 339.6115, pp. 64–67. ISSN: 0036-8075. DOI: [10.1126/science.1225759](https://doi.org/10.1126/science.1225759). eprint: <http://science.sciencemag.org/content/339/6115/64.full.pdf>.
- (2013b). "Water loss from terrestrial planets with CO₂-rich atmospheres". In: *ApJ* 778.2, p. 154. DOI: [10.1088/0004-637x/778/2/154](https://doi.org/10.1088/0004-637x/778/2/154).
- Wordsworth, R., L. Schaefer, and R. A. Fischer (2018). "Redox evolution via gravitational differentiation on low-mass planets: implications for abiotic oxygen, water loss and habitability". In: *AJ* 155.5, p. 195. DOI: [10.3847/1538-3881/aab608](https://doi.org/10.3847/1538-3881/aab608).
- Yamamoto, G. and G. Onishi (1952). "Absorption of solar radiation by water vapor in the atmosphere". In: *J Meteor* 9.6, pp. 415–421. DOI: [10.1175/1520-0469\(1952\)009<0415:aosrbw>2.0.co;2](https://doi.org/10.1175/1520-0469(1952)009<0415:aosrbw>2.0.co;2).
- Yang, J., J. Leconte, E. T. Wolf, C. Goldblatt, N. Feldl, T. Merlis, Y. Wang, D. D. B. Koll, F. Ding, F. Forget, et al. (2016). "Differences in water vapor radiative transfer among 1D models can significantly affect the inner edge of the habitable zone". In: *The Astrophysical Journal* 826.2, p. 222. DOI: [10.3847/0004-637X/826/2/222](https://doi.org/10.3847/0004-637X/826/2/222).
- Zahnle, K. J., J. F. Kasting, and J. B. Pollack (1988). "Evolution of a steam atmosphere during earth's accretion". In: *Icar* 74.1, pp. 62–97. ISSN: 0019-1035. DOI: [10.1016/0019-1035\(88\)90031-0](https://doi.org/10.1016/0019-1035(88)90031-0).
- Zhang, H. L., M. M. Hirschmann, E. Cottrell, and A. C. Withers (2017). "Effect of pressure on Fe³⁺/ΣFe ratio in a mafic magma and consequences for magma ocean redox gradients". In: *GeCoA* 204, pp. 83–103. DOI: [10.1016/j.gca.2017.01.023](https://doi.org/10.1016/j.gca.2017.01.023).
- Zhang, J. and C. Herzberg (1994). "Melting experiments on anhydrous peridotite KLB-1 from 5.0 to 22.5 GPa". In: *JGR* 99.B9, pp. 17729–17742. DOI: [10.1029/94JB01406](https://doi.org/10.1029/94JB01406).

EIDESSTATTLICHE VERSICHERUNG
DECLARATION BY THE AUTHOR

Hiermit erkläre ich an Eides statt, dass ich die vorliegende Dissertationsschrift selbst verfasst und keine anderen als die angegebenen Quellen und Hilfsmittel benutzt habe.

I hereby declare, on oath, that I have written the present dissertation by myself and have not used other than the acknowledged resources and aids.

Berlin, May 5, 2020

Athanasia Nikolaou